In-situ Examination of Diffusion and Precipitation Processes during the Evolution of Chemical Garden Systems

Dissertation

zur Erlangung des Grades
Doktor der Naturwissenschaften (Dr. rer. nat.)
der Naturwissenschaftlichen Fakultät IV
Chemie und Pharmazie
Universität Regensburg

vorgelegt von

Fabian Glaab

Regensburg 2011

Promotionsgesuch eingereicht am: 15.12.2011

Promotionskolloquium am: 03.02.2012

Die Arbeit wurde angeleitet von: Prof. Dr. Werner Kunz

Prüfungsausschuss:

Vorsitzender: Prof. Dr. Dominik Horinek

1. Gutachter: Prof. Dr. Werner Kunz

2. Gutachter: Prof. Dr. Arno Pfitzner

3. Gutachter: Prof. Dr. Henri Brunner

That’s only one small step for mankind…

…but one giant leap for me.

Abstract

"Chemical" or "silicate gardens" are a well known example for the spontaneous formation of a complex and structured system from ordinary educts. Simply by addition of soluble metal salt crystals to alkaline silica sols, dissolution of the metal salt and subsequent solidification initiate a self-organization process, which not only produces two separated compartments with drastically different chemical conditions by precipitation of a closed and tubular membrane but also produces a variety of stunning structures reminiscent of living forms such as trees or aquatic plants.

Although a considerable number of scientific studies was dedicated to chemical gardens and related phenomena during the last more than 300 years, current literature is still lacking in central aspects of chemical garden growth. Especially due to the fact that most of the studies concentrated on *ex-situ* characterizations of these stunning architectures, only rare information is available to date on the evolution of dynamic processes occurring *during* their growth.

The present thesis therefore mainly focuses on the time-resolved evaluation of crucial parameters in the course of chemical garden growth to contribute to the amplification of the knowledge on these long since discovered phenomena.

Several strategies are developed in this work, aiming on the establishment of suitable *in-situ* examination techniques allowing for the direct observation of critical parameters in both generated compartments during chemical garden evolution.

Implementation of a novel preparation procedure – involving the slow addition of sodium silicate solution to tablets of pressed metal salts (instead of small seed crystals) – yields in the formation of uniform and macroscopic tubular membranes with one end open to the atmosphere. This modification of the classical preparation procedure paves the way for directly accessing the heretofore caged interior compartment and therefore allows a continuous analysis by different techniques.

X-ray absorption spectroscopy (XAS) and atomic emission spectroscopy (AES) techniques are applied to analyze the temporal evolution of ion species concentrations and their distribution in the outer and interior compartments of the generated silicate

garden tubes. Together with continuous measurements of the pH in the interior and exterior compartments, these techniques are used for the detection of occurring diffusion processes across the precipitated tubular membrane and their temporal evolution. Presented results from these measurements show that chemical gardens are a complex system operating far from equilibrium due to a spontaneous separation of two solutions with drastic concentration differences by a porous membrane during the early stages of formation. It is demonstrated that the evolution of the system and its return to thermodynamic equilibrium are not at all completed once macroscopic growth of the well-known tubular structures is terminated. Instead, a series of diffusion and (coupled) precipitation processes occur over timeframes of up to days after preparation, gradually relieving the initially generated concentration gradients. The results of this work further illustrate that the walls of silica gardens allow bidirectional and non-specific ion transport, and thus fundamentally challenge the currently accepted model of a semi-permeable membrane.

Observed concentration and pH gradients across the tube wall implicate the existence of appreciable potential differences between the two compartments, which were directly measured in this work. From results of long-term electrochemical potential measurements, it is deduced that the overall detected cell potential can be explained by a superposition of diffusion, membrane and pH induced potentials prevailing across the silicate garden walls.

Different *in-situ* and *ex-situ* XRD techniques are used to identify the existence of crystalline material in the precipitated tube walls. Recorded data from independently obtained XRD analyses, together with results from AES and XAS measurements, are used to establish a model that describes the kinetics of precipitation and crystallization processes during chemical garden growth as those of an irreversible consecutive reaction. The kinetic model of silicate garden growth is found to be universally applicable and might therefore probably be transferable to other systems, in which a combination of dissolution, precipitation and crystallization processes play an important role, e.g. in the progress of Portland cement hydration.

Ex-situ analyses of isolated membrane tubes on their structural and chemical composition, using scanning electron microscopy (SEM) in combination with energy dispersive X-ray spectroscopy (EDX), reveal a partial layering of the precipitated membrane tubes, exhibiting a silica-rich exterior and an interior surface mainly consisting of pure metal hydroxide. Furthermore, different kinds of stunning sub-structurings of the exterior and interior surfaces of the tubular precipitates are observed, ranging from periodical waviness on the exterior silica skin via interwoven fiber-networks up to clusters of metal oxide hydroxide rosettes or isolated crystallites. Therefore, this structural diversity directly mirrors the influence of the preparation technique as well as of precipitation and crystallization processes, occuring during the growth of chemical gardens, on their resulting structures.

Zusammenfassung

„Chemische Gärten“, auch verbreitet unter dem Begriff „Silikatgärten“, sind ein wohlbekanntes Beispiel für die spontane Entstehung komplexer und strukturierter Systeme aus einfachen, abiotischen und anorganischen Ausgangsstoffen. Dabei wird durch simple Zugabe von Kristallen wasserlöslicher, mehrwertiger Metallsalze zu alkalischen Silikatlösungen ein Selbstorganisationsprozess in Gang gesetzt, der nach rasch beginnender Auflösung des Metallsalzes zur unmittelbaren Ausbildung einer geschlossenen, gelartigen Membran aus Metallsilikat führt. Durch diese Prozesse entstehen zwei getrennte Kompartimente, deren jeweilige Lösungen sich in ihrer chemischen Zusammensetzung drastisch unterscheiden. Im weiteren Verlauf dieser spontanen Reaktion kommt es durch wiederholtes Platzen der Membran zur Ausbildung ungewöhnlicher Strukturen, die aufgrund ihres äußeren Erscheinungsbildes lebenden Organismen, wie beispielsweise Bäume oder Wasserpflanzen, stark ähneln. Historisch bedingt, leitet sich die Bezeichnung „chemische Gärten“ aus dieser strukturellen Übereinstimmung ab.

Trotz zahlreicher wissenschaftlichen Studien innerhalb der letzten mehr als 300 Jahre, die sich der Untersuchung chemischen Gärten und ähnlicher Phänomene widmeten, blieben bisher noch zentrale Aspekte zum Wachstum dieser Strukturen ungeklärt. Da die meisten bisherigen Studien sich mit der nachträglichen Untersuchung isolierter Strukturen *nach* dem Wachstumsprozess beschäftigten, sind bis heute nur wenige Informationen über die zeitliche Entwicklung ablaufender dynamischer Prozesse, *während* des Wachstums vorhanden.

Aus diesem Grund steht in der vorliegenden Arbeit die Entwicklung und Anwendung geeigneter Methoden zur zeitlich aufgelösten Untersuchung wichtiger Parameter während des Wachstumsprozesses chemischer Gärten im Mittelpunkt.

Eine notwendige Voraussetzung zur erfolgreichen Durchführung kontinuierlicher Analysemessungen in beiden Kompartimenten liegt insbesondere in der Entwicklung einer neuartigen Präparationsmethode, die eine einfache und direkte Analyse der bisher schwer zugänglichen inneren Lösung im Inneren der sich bildenden Membranröhren erlaubt. Eine geeignete Lösung dieses Problems liegt sowohl in der Verwendung

gepresster Metallsalztabletten anstatt agglomerierter Kristalle als auch in einer langsamen Zudosierung der verdünnten Natriumsilikatlösung. Eine derartige Modifizierung des klassischen Präparationsschemas ermöglicht die Synthese gleichförmiger, makroskopischer und nach oben hin offener Membranröhren, die einen direkten Zugang zur Lösung im Inneren der Röhre gewährleisten.

Im Rahmen dieser Arbeit wurden verschiedene *in-situ* Techniken zur zeitaufgelösten Untersuchung des Wachstums chemischer Gärten angewendet.

Mithilfe der Röntgenabsorptionsspektroskopie (XAS) sowie der Atomemissionsspektroskopie (AES) wurde der zeitliche Verlauf der Konzentrationen aller Ionenspezies und deren Verteilung in den äußeren und inneren Lösungen der präparierten Membranröhren analysiert. Zusammen mit Langzeitmessungen von pH-Werten in beiden Kompartimenten wurden diese Methoden dazu verwendet, Diffusionsprozesse durch die generierte Membran und deren zeitliche Entwicklung aufzuklären. Die Ergebnisse aus diesen Messungen zeigen, dass chemische Gärten komplexe Systeme darstellen, die sich aufgrund der Ausbildung separater Kompartimente mit drastisch differenten chemischen Eigenschaften zu Beginn des Wachstums weit entfernt vom thermodynamischen Gleichgewicht befinden. Die Resultate aus allen Messungen offenbaren ferner, dass die Entwicklung chemischer Gärten und deren Rückkehr ins thermodynamische Gleichgewicht bei weitem nicht mit der Beendigung des makroskopischen Wachstums abgeschlossen ist. Vielmehr trägt eine Reihe an Diffusions- und gekoppelten Fällungsprozessen über einen Zeitraum von bis zu mehreren Tagen zur schrittweisen Beseitigung der anfänglich generierten Konzentrationsgradienten bei.

Die in dieser Arbeit präsentierten Analysen lassen erschließen, dass die Wände der Silikatgärten einen bidirektionalen und unspezifischen Transport von Ionen erlauben, was somit grundsätzlich das bisher in der Literatur verbreitete Modell einer semipermeablen Membran in Frage stellt.

Die beobachteten Konzentrations- und pH-Gradienten über die Membranröhren legen die Existenz beachtlicher Potentialdifferenzen zwischen beiden Kompartimenten nahe, die im Rahmen dieser Arbeit auch direkt vermessen werden konnten. Aus den Ergebnissen von Langzeitmessungen elektrochemischer Potentiale lässt sich ableiten, dass sich das vorliegende und gemessene Gesamtpotential über die Wandung der chemischen Gärten durch eine Überlagerung aus Diffusions-, Membran- und pH-induzierten Potentialen ergibt.

Verschiedene *in-situ* und *ex-situ* Methoden aus dem Bereich der Röntgendiffraktometrie kamen zur Identifikation vorhandener kristalliner Anteile in den erhaltenen Präzipitaten zur Anwendung. Daten aus unabhängig voneinander durchgeführten XRD-Analysen wurden zusammen mit Ergebnissen aus AES- und XAS-Messungen zur Beschreibung der Kinetik der während der Entwicklung chemischer Gärten ablaufenden Fällungs- und Kristallisationsprozesse verwendet. Die Verläufe der Metallionenkonzentrationen im Inneren der chemischen Gärten sowie die Zunahme der gefunden kristallinen Anteile während der Entwicklung chemischer Gärten konnten der Kinetik einer irreversiblen Konsekutivreaktion zugeschrieben werden. Das etablierte kinetische Modell ist unabhängig vom verwendeten Metallsalz universell anwendbar und kann daher möglicherweise auch auf andere Systeme übertragen werden, bei denen eine Kombination von Auflösungs-, Fällungs- und Kristallisationsprozessen eine wichtige Rolle spielt, beispielsweise bei der Ausbildung dreidimensionaler Calcium-Silikat-Hydrat-Netzwerke während der Aushärtung von Portlandzement.

Ex-situ Analysen zur strukturellen und chemischen Charakterisierung isolierter Membranröhren wurden mithilfe der Rasterelektronenmikroskopie (SEM) und in Kombination mit energiedispersiver Röntgenspektroskopie (EDX) durchgeführt. Untersuchungen am Material isolierter Membrane zeigen zum Teil die Ausbildung von Schichten unterschiedlicher chemischer Zusammensetzung innerhalb der Membranwände; so weist die äußere Seite der Membran tendenziell einen hohen Silikatanteil auf, während die Innenseite vorwiegend aus Metallhydroxiden besteht. Darüber hinaus finden sich unterschiedliche Arten bemerkenswerter Unterstrukturierungen auf den äußeren und inneren Oberflächen der Membranröhren. Diese reichen vom periodischen Auftreten wellenartiger Strukturen auf der äußeren, silikatreichen Seite, über ausgedehnte Netzwerke ineinander verwobener Fasern, bis hin zur Existenz isolierter Kristallite oder Rosetten aus Metallhydroxiden. Diese strukturelle Diversität spiegelt somit direkt den Einfluss der Präparationsmethode sowie der beteiligten Präzipitations- und Kristallisationsprozesse während des Wachstums auf die resultierenden Strukturen chemischer Gärten wider.

Preface

This thesis originates from studies performed at the Institute of Physical and Theoretical Chemistry of the University of Regensburg in the period from November 2005 to October 2011. Besides a two-months stay at the Laboratorio de Estudios Cristalográficos (LEC) (Granada, Spain), parts of the presented results were also obtained during several beamtimes at the synchrotron radiation facilities ELETTRA (Trieste, Italy), MAX-lab (Lund, Sweden) and HASYLAB/DESY (Hamburg, Germany).

Realization of the present work would not have been possible without the precious help and support of numerous people who I want to express my gratitude in the following.

First of all, I would like to thank my supervisor Prof. Dr. Werner Kunz for offering me the opportunity to work at his institute and for providing a relaxed and unforced environment, enabling the conductance of independent and unprejudiced research. His patience and open mind for many scientific fields allowed me the performance of systematic studies on this interesting topic of fundamental research at a time, where acquisition of information for commercial research becomes more and more relevant. I furthermore appreciate his objectivity towards the results of this thesis, which, in my opinion, might partially become overrated and exploited by other persons involved in this field.

In this context, I would also express my deep gratitude to Prof. Dr. Juan Manuel García-Ruiz (LEC Granada), who initiated the focusing of this thesis on the topic of chemical gardens and thereby opened the chance for a lively collaboration and interaction of both institutes also in this field of science. I appreciate his invitation for a stay in Granada and his persistent enthusiasm and help in the ongoing evaluation and interpretation of the data collected in the frame of this work.

Further acknowledgement is also addressed to Prof. Dr. Emilia Morallon Nunez for her clarifying contribution in the field of electrochemistry, helping with the interpretation of experimental results obtained from electrochemical potential measurements.

At this point, thanks also go to my employer ETC Products GmbH for offering me in the last five years the opportunity to gain valuable insight in the highly interesting field of surface functionalization by sol-gel coatings and their industrial application. In particular, I want to express my gratitude to Dr. Monika Mitterhuber, Walter Hilgart and Simone Vogl for the uncomplicated and harmonic atmosphere during the overall period of collaboration.

Dr. Emilio Melero-Garcìa and Dr. Duane Choquesillo-Lazarte are acknowledged for their experimental support during several beamtimes at the ELETTRA and HASYLAB/DESY synchrotron radiation facilities. Further thanks go to Dr. André Rothkirch, Dr. Edmund Welter, Dr. Thomas Wroblewski (all HASYLAB), Alberto Cassetta, Luisa Barba (both ELETTRA) and Dr. Stefan Carlson (MAX-lab) for their excellent technical support at the beamlines.

Thanks go to Björn Bartel for performing parts of the SEM and EDX analyses, and I would also like to acknowledge the staff of the mechanical and electronic workshops for their competent help in technical matters whenever required. Further thanks are addressed to Robert Weikl, Carolin Fürst, Bastian Hiltl and Martin Fleischmann for carrying out some of the AES, pH and potential measurements.

Roger-Jan Kutta (University of Regensburg) is acknowledged for providing proprietary programmed routines very useful for facilitated data processing and graphical illustration.

To all current and former colleagues at the Institute of Physical and Theoretical Chemistry, cordial gratitude is owed for the enjoyable working atmosphere and uncomplicated collaboration they offered to me.

Thereby, particular thanks are addressed to my veteran lab fellow Matthias Kellermeier for intensive and inspiring discussions and his support during the last seven years not only in the context of this thesis but also in private matters. I am furthermore pleased to thank Regina Klein and Alexander Schätz for their friendship and loyality during the many years of study and graduation. I would also like to express my gratitude to Alexander Stoppa, Josef Eiblmeier and Teresa Maltry for spending a good and enjoyable time together during the last years.

Finally, my gratitude is directed to Prof. Dr. Arno Pfitzner and Prof. Dr. Henri Brunner for their willingness to be examiners of this thesis.

Special thanks go to my family and all of my friends who faithfully accompanied me through foul and fair, offering me support and good and joyful times and thereby significantly contributing to the realization of this work.

My deepest gratitude, however, is reserved to my parents, and in particular to my mother, for being always on my side and never loosing trust in me, giving me the power and motivation to finally achieve my desired objectives. Without their mental support and enduring optimism, I would probably never have succeeded to come so far, and therefore this thesis is especially dedicated to them.

Fabian Glaab, Regensburg, Dezember 2011.

Table of Contents

I. Introduction and Purpose

1. The Formation of Chemical Gardens

Simply by addition of soluble metal salt crystals to alkaline silica sols, dissolution of the metal salt and subsequent solidification give birth to a self-organization process, which not only produces two separated compartments with drastically different chemical conditions but also produces a variety of stunning structures reminiscent of living forms such as trees or aquatic plants. Chemical gardens, grown from different metal salts in diluted water glass, are presented in Fig. 1 and exhibit plant-like structures.

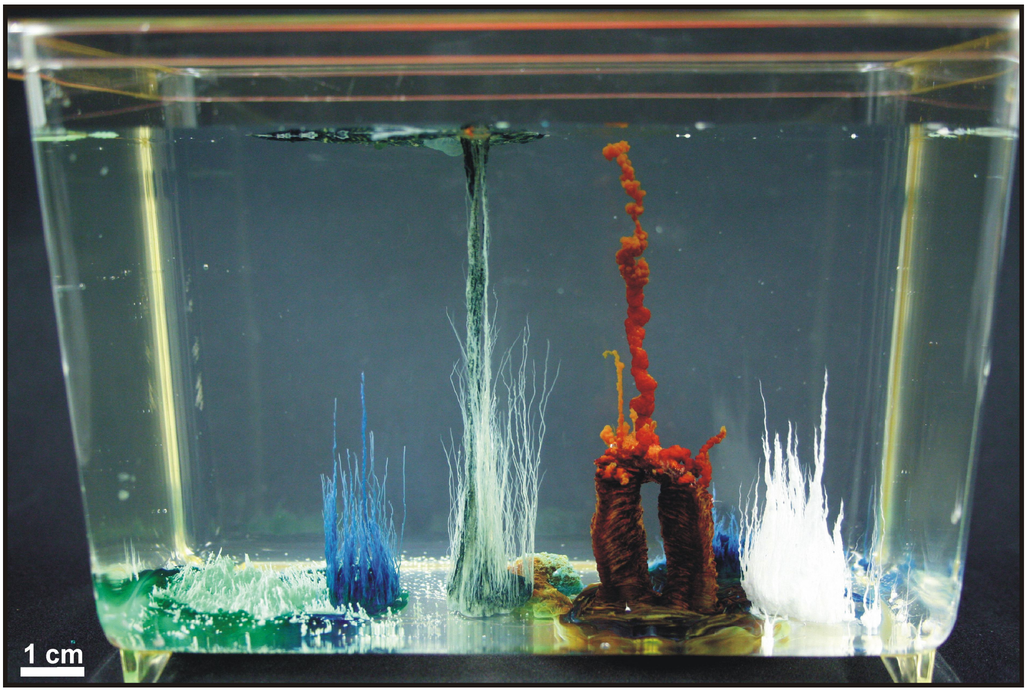

Fig. 1: Image showing chemical gardens grown from crystal clusters immersed into diluted sodium silicate solution after four hours; used metal salts were (from left to right): $NiSO_4 \cdot 6\ H_2O$ (cyan), $CoCl_2 \cdot 6\ H_2O$ (blue), $FeCl_2 \cdot 6\ H_2O$ (green), $Cu(NO_3)_2 \cdot 3\ H_2O$ (blue), $FeCl_3 \cdot 6\ H_2O$ (orange), $Co(NO_3)_2 \cdot 6\ H_2O$ (blue), $CaCl_2 \cdot 2\ H_2O$ (white).

Due to these features, resembling biogenic species though consisting entirely of inorganic matter, these “chemical” or “silica gardens” have aroused a flurry of interest around a century ago in the context of a search for the origin of life.[1]

2. History of Chemical Garden Phenomena

First mentioned in literature by Glauber more than 300 years ago,[2] the formation of "chemical gardens" became a well known example for the spontaneous self-organization of simple materials to highly complex structures.

Initially, the growth of chemical garden-like structures was thought to rely essentially on the chemistry of silica. Later studies yet revealed that solutions of other oxo-anions such as oxalates, acetates, hydroxides, carbonates, sulfates, phosphates or chromates are under certain conditions also capable media for the production of similar architectures.[3-4] In contrast to the more or less limited number of suitable anions, cations of most metals can be used for the preparation of silica gardens, except for alkali metals due to the high solubility of their silicates.[5]

For a long time, barely coarse information was available on the details of this self-organized mineralization process. About thirty years ago, it returned into focus again as more profound investigations were started by several groups which still continue to date. While research in the distant past was mainly concentrated on extending the concept of chemical gardens to a wider range of metal salts and anions, the scopes of recent work diverge and primarily concentrate on the analysis of the basic formation mechanism of chemical gardens, as well as on their structural and chemical characterization. Different techniques were also employed to control and design the growth of chemical gardens. Another group of studies elucidates the involvement of similar processes in different practical problems and other related phenomena.

3. Fragmentary Knowledge in Current Literature

Despite of the numerous studies performed on chemical gardens and related phenomena up to date (which will be presented in more detail in chapter II of this thesis), central aspects of chemical garden growth have remained insufficiently understood and require further clarification.

A. Properties of the Tubular Precipitates

For example, the detailed nature and properties of the walls separating the inner acidic metal salt solution from the outer alkaline silica sol, and in particular their compositional evolution with time, have not been elucidated yet. These layers are traditionally thought to behave like semi-permeable membranes through which only water molecules can penetrate,[6-22] though some authors speculated that also hydroxide ions may diffuse to some extent from the outside to the inside.[7, 15, 23-24]

B. Lacking Information on the Evolution of Dynamic Processes during Growth

A major reason for the given fragmentary knowledge on such dynamic phenomena in chemical gardens is that many investigations were of more or less unsystematic nature and mainly focused on characterizing the precipitates after growth had been terminated and samples were harvested. Consequently, only few data exist that reflect processes which occur *during* formation and important information about spatiotemporal changes of many crucial parameters is still missing. For example, only rare information is available on the progression of diffusion processes, while quantitative statements on the kinetics of involved precipitation and crystallization processes are even completely lacking. Current literature also provides only qualitative data on the evolution of pH and ion concentrations during the growth of silicate gardens.

C. Poor Reproducibility of Conventional Chemical Garden Experiments

Another general problem one has to cope with when studying chemical gardens is the rather poor reproducibility of conventional experiments. Although the observed architectures rely on the same structural principles and growth mechanisms, their particular morphologies, dimensions and chemical specification are quite unique and accidental, thus rendering consistent analyses difficult.

4. Strategies Contributing to Further Clarification

To contribute to the closing of the gap in the knowledge of chemical garden growth, several strategies are developed, focusing on the establishment of standardized *in-situ* examination techniques for the direct observation of critical parameters during chemical garden evolution.

A. Implementation of a Standardized Preparation Procedure

The first step towards the realization of these purposes founds in the selection of suitable materials and the establishment of a proper preparation routine which allows for the controlled growth of silicate gardens, exhibiting a macroscopic, tubular shape. By this novel setup, reproducible examinations are enabled to gain important information about the evolution of dynamic processes (diffusion, precipitation, crystallization) and chemical gradients (pH, ion concentrations, electrochemical potentials) in silicate garden systems.

B. Selection of Suitable Methods for Time-resolved Examinations

In this thesis, different techniques are tested and employed for *ex-situ* and *in-situ* characterizations of these modified chemical garden systems.

Scanning electron microscopy (SEM) in combination with energy dispersive X-ray spectroscopy (EDX) is used for *ex-situ* analyses of isolated membrane tubes on their structural and chemical composition to contribute to the clarification of the membrane structuring and its resulting properties.

Different *in-situ* X-ray diffraction (XRD) techniques are used to identify the existence of crystalline material in the precipitated tube walls. Furthermore, these methods are used to evaluate important data on the evolution of crystallization processes occurring during silicate garden growth.

X-ray absorption spectroscopy (XAS) and atomic emission spectroscopy (AES) techniques are applied to obtain relevant information about the temporal evolution of ion species concentrations and their distribution in the outer and interior compartments of the generated silicate garden tubes. Together with continuous measurements of the pH in the interior and exterior compartments, these techniques aim on the identification of existing diffusion processes across the precipitated tubular membrane and their temporal evolution.

Installation of a suitable setup, allowing a time-resolved detection of possibly existing potential differences across the membranes is aspired to identify electrochemical processes occurring during the growth of silica gardens.

Experiments should also provide sufficient data to allow a quantitative estimation of the total period of chemical garden evolution, i.e. the time the system requires to finally end up in thermodynamic equilibrium.

All examination methods installed in the framework of this thesis finally aim on the establishment of a detailed model which quantitatively describes the evolution of all relevant processes during the overall period of growth.

II. Fundamental Information

As already indicated in the introductory part of this work, research on chemical gardens for more than 300 years has already brought forth a considerable quantity of literature. Therefore, this chapter is dedicated to introduce the reader to the current status of knowledge on this field of science. Focus is thereby laid on the presentation of more recent research activities, which, despite of their divergence, can roughly be assigned to four major topics:

The first is dealing with the elucidation of the basic formation mechanism, while a second research field involves the characterization of chemical gardens on their structural and chemical composition after growth. A third field of research interest focuses on the control and design of the growth of chemical gardens by different methods. Finally, the involvement of similar processes in different practical problems and other related phenomena is pointed out by another group of studies.

Most relevant and interesting results of each research field are presented in the following four sections, starting with the explanation of the fundamental mechanism governing the formation of these extraordinary structures.

1. Qualitative Mechanism of Formation

1.1. Underlying Physical Processes

The first and most fundamental field of scientific interest on the chemical garden phenomenon concerns the search for a basic model explaining their formation on a mechanistic level.[6, 25]

By the use of interferometric methods during the preparation of silicate gardens from $CoCl_2$ crystals in diluted water glass, it was found that growth is fuelled by a combination of forced convection from osmosis and free convection from buoyancy, together with chemical reaction.[7] As depicted in Fig. 2, several steps lead to the formation of the resulting vertically grown tubular precipitates: Addition of a metal salt crystal to silica sols (a) triggers the immediate formation of a layer of colloidal gel consisting of hydrous metal silicate around the crystal (b). Osmotically driven inflow of liquid from the silicate solution outside the membrane subsequently increases the interior volume (c), thus leading to further dissolution of the solid metal salt and an expansion of the flexible membrane until it bursts (d). As the membrane ruptures, pressure is relieved and a jet of concentrated metal salt solution is ejected from the inside into the surrounding medium, ascending vertically due to the lower density of the interior metal salt solution (e). Instant precipitation of metal silicate and hydroxide at the boundary layer between the inner and outer solution seals the ruptured membrane such that, in the following, the internal pressure re-increases.

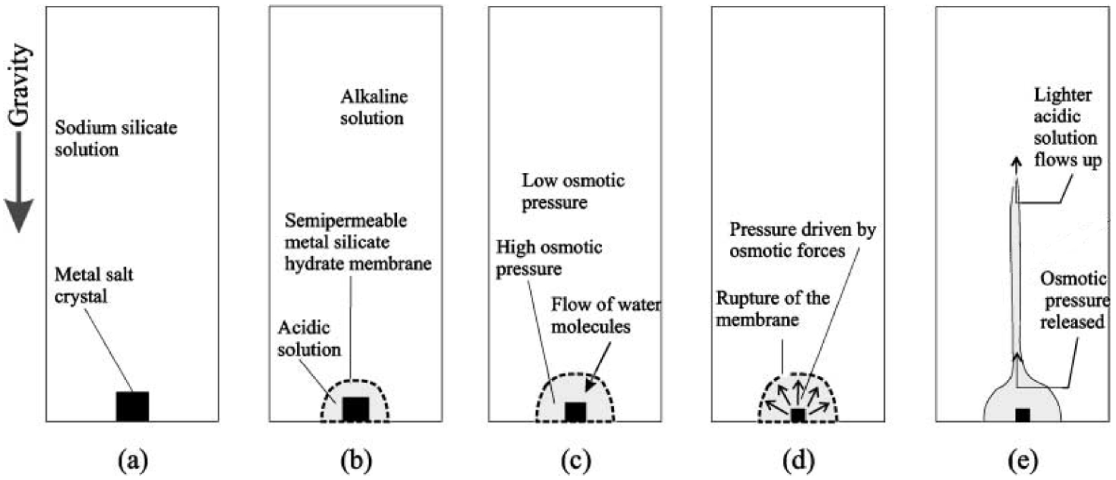

Fig. 2: Reaction steps leading to the formation of tubular silica gardens: (a) setup at start of the reaction, (b) membrane formation between acidic and basic solutions, (c) higher osmotic pressure in the interior causes expansion of the membrane by inflow of water, (d) rupture of the membrane at excess pressure, (e) formation of vertical tubes by buoyancy.[7]

The existence of osmotic processes during the formation of chemical gardens was first demonstrated by the establishment of a simplified model, consisting of an inorganic porous membrane pot which separates an interior concentrated cobalt chloride brine from a surrounding sodium silicate solution (Fig. 3b).

From this experiment it was deduced that osmotic driven inflow of water through the porous membrane leads to a dilution of the concentrated $CoCl_2$ solution and thus to an expansion of the interior volume (Fig. 3a).

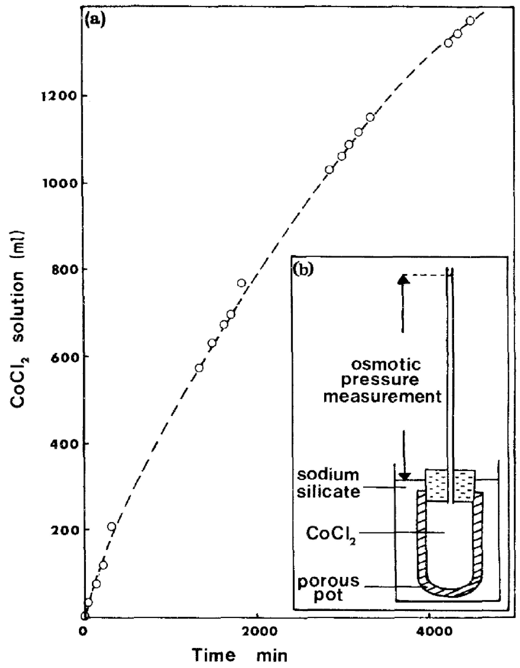

Fig. 3: Experiment to illustrate the semi-permeable nature of the colloidal gel membrane. (a) Graph showing the pressure increase as a function of time. (b) Schematic drawing of the apparatus used as a model for silicate gardens.[6]

Besides the observed in-diffusion of water through the membrane, some authors further postulate from elemental compositions of the interior surface of isolated tubules that the initially formed membrane is also permeable for hydroxide[7] and sodium ions,[26-27] respectively.

1.2. Pressure Oscillations

Pressure oscillations, caused by repeated membrane rupture and subsequent sealing processes during the growth of chemical gardens were identified by using a setup deviating from the classical experiment. Instead of starting with a solid metal salt crystal, a concentrated $CaCl_2$ solution was pumped into a sodium silicate solution from the bottom of a reaction vessel (Fig. 4a), while the pressure of the interior $CaCl_2$ solution was monitored during the growth of the resulting chemical garden (Fig. 4b).[28]

Two different types of pressure oscillations could be identified: slow oscillations correspond to simultaneous ruptures at different locations of the membrane, so that the membrane surface is increased by a significant amount (Fig. 4b left). In contrast, fast pressure oscillation is observed during the growth of tubular filaments. In this case, the membrane surface is only little enlarged, thus rapidly causing repeated membrane rupture at the end of the tube (Fig. 4b right). As a result of repeated membrane rupturing and sealing, oscillatory growth of the tubular precipitates is observed.

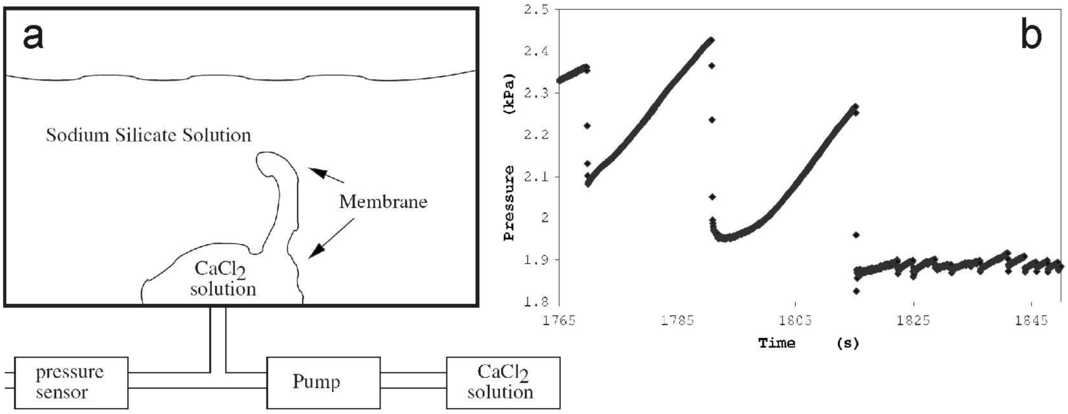

Fig. 4: (a) Schematical drawing of the setup used to measure the pressure oscillations inside the precipitated membrane and (b) resulting temporal evolution of the interior pressure, showing two different modes of pressure oscillations.[28]

1.3. Membrane Structuring by Concurrent Solidification Processes

1.3.1. Precipitation and Gelification Reactions

In general, growth of silicate gardens involves the concurrent solidification of three different material classes by a combination of sol-gel processes with precipitation reactions, altogether forming a complex structured composite membrane material.[16, 29]

In the beginning stages of crystal dissolution, the metal ions rapidly react with the aqueous sodium silicate, leading to the formation of a colloidal gelly membrane composed of ill-defined hydrous metal silicate (Eq.(1)). However, as the multivalent metal ions also act as Lewis acids, the pH at the front where silicate and metal ions clash is significantly lowered. As a consequence, the solubility of silicate is drastically reduced, resulting in the protonation of the anionic silicate ions and subsequently in the condensation of the monomeric silicic acid units to an insoluble silica gel layer (Eq.(2)). Both of these reaction steps correlate to the sol-gel process (cf. section II.1.3.2). On the other hand, the in-flow of water molecules and hydroxide ions through the generated siliceous membrane increases the pH on the interior surface of the membrane. The increase in alkalinity thus leads to the formation of metal hydroxide and its subsequent polymerization (Eq.(3)).

- Formation of ill-defined hydrous metal silicate ($m < 1$; $x > 1$; $y = 4 - 2\,(x - m)$):

$$[\mathrm{SiO(OH)_3}]^- + (2\,m-1)\,\mathrm{OH}^- + m\,\mathrm{M}^{2+} \longrightarrow \mathrm{M}_m\left[\mathrm{SiO}_x(\mathrm{OH})_y\right] + (x-1)\,\mathrm{H_2O} \quad (1)$$

- Precipitation of silica:

$$[\mathrm{SiO(OH)_3}]^- + \mathrm{H}^+ \longrightarrow \mathrm{Si(OH)_4} \to \to \text{"}\mathrm{SiO_2}\text{"} + 2\,\mathrm{H_2O} \quad (2)$$

- Formation of metal hydroxide and its polymerization:

$$n\,\mathrm{M}^{2+} + 2\,n\,\mathrm{OH}^- \longrightarrow n\,\mathrm{M(OH)_2} \longrightarrow (-\mathrm{M}-\mathrm{O}-)_n + n\,\mathrm{H_2O} \quad (3)$$

To get an idea about the silicate species existing in the surrounding water glass at different pH, distribution profiles for monomeric silicate species in solution were calculated as a function of pH on the basis of the corresponding acid/base equilibria:

$$\mathrm{Si(OH)_4} \underset{}{\overset{\mathrm{K_1}}{\rightleftarrows}} \mathrm{Si(OH)_3O^-} + \mathrm{H}^+ \underset{}{\overset{\mathrm{K_2}}{\rightleftarrows}} \mathrm{Si(OH)_2O_2^{2-}} + 2\,\mathrm{H}^+ \quad (4)$$

where K_1 and K_2 are the first and second dissociation constant of silicic acid. Considering the principle of mass preservation and assuming in a rough approximation ideality for the solutions, the following equations for the pH-dependent species concentrations can be derived:

$$[\mathrm{Si(OH)_4}] = \frac{[\mathrm{SiO_2}]_0 \cdot [\mathrm{H}^+]^2}{\mathrm{K_1} \cdot \mathrm{K_2} + \mathrm{K_1} \cdot [\mathrm{H}^+] + [\mathrm{H}^+]^2} \quad (5)$$

$$[\mathrm{Si(OH)_3O}]^- = \frac{\mathrm{K_1} \cdot [\mathrm{H}^+] \cdot [\mathrm{SiO_2}]_0}{\mathrm{K_1} \cdot \mathrm{K_2} + \mathrm{K_1} \cdot [\mathrm{H}^+] + [\mathrm{H}^+]^2} \quad (6)$$

$$[\mathrm{Si(OH)_2O_2}]^{2-} = \frac{\mathrm{K_1} \cdot \mathrm{K_2} \cdot [\mathrm{SiO_2}]_0}{\mathrm{K_1} \cdot \mathrm{K_2} + \mathrm{K_1} \cdot [\mathrm{H}^+] + [\mathrm{H}^+]^2} \quad (7)$$

Thereby, $[\mathrm{SiO_2}]_0$ represents the overall analytical silica concentration. The values used for the dissociation constants of silicic acid during calculation were $K_1 = 1.44 \cdot 10^{-10}$ mol L^{-1} and $K_2 = 3.72 \cdot 10^{-14}$ mol L^{-1}.[30]

The resulting distribution profiles of the silicate species prevailing at a pH range from 5 to 14 are given in Fig. 5. At the high pH given in the outer water glass reservoir, all silica is expected to exist in a charged deprotonated form and thus remains dissolved due to electrostatic repulsion. Upon lowering the pH, the degree of protonation is increased and condensation processes take place, eventually leading to the formation of insoluble polymeric silicate species. Consequently, under the near-neutral to slightly acidic conditions prevailing in the interior solution (pH 5-7), quantitative precipitation of amorphous silica occurs such that penetration of dissolved silicate ions through the membrane walls is prevented and only water and hydroxide ions are able to pass through.

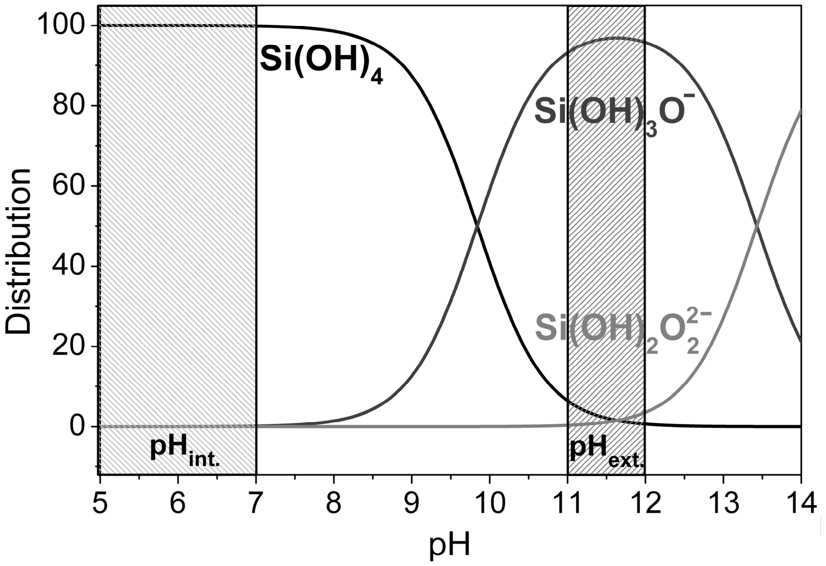

Fig. 5: Distribution profiles for monomeric silicate species occurring in solution as a function of pH. Shaded areas mark the pH ranges found in the inner metal salt solutions (pH < 7) and the exterior silica sol (pH ~ 11-12).

As a consequence of the interplay of above described solidification processes, the membrane wall is supposed to consist of three layers of different composition.[19] Starting from the interior of the tubular precipitates, a primary layer, composed of metal hydroxide or metal oxide, is adjoined to a secondary transition layer consisting of a metal silicate compound. The exterior surface, which is in contact with the diluted water glass, finally consists of an outer silica shell (Fig. 6).

Fig. 6: Schematical cross-section of the membrane wall, showing the proposed formation of three layers of different composition according to the proposed precipitation and gelation reactions.[29]

However, by today, no detailed description is given in literature about the thickness of each layer or the zones of transition. Overall, the structures formed in chemical gardens consist of a complex, mostly amorphous material.

Independent of the use of solid or liquid metal salt precursors, vertical hollow tubes are generated as a result of precipitation and gelation processes, with typical dimensions of a few millimeters in width and up to several centimeters in length.[31]

At the end of macroscopic growth, the formed metal silicate/hydroxide wall separates an enclosed volume of concentrated acidic metal salt solution from a surrounding, highly alkaline sodium silicate solution.

1.3.2. Introduction to the Sol-Gel Process

Basically, two different methods of sol-gel processing exist; the first method is based on the use of aqueous solutions of inorganic precursors, i.e. dissolved alkali metal silicate species, the second pathway starts from metal organic precursors, i.e. alkoxy silanes or transition metal alkoxides.

1.3.2.1.Gelification of Aqueous Solutions of Sodium Silicate

Method 1, the gelification of silica-rich gels from inorganic precursors, is based on the following three steps, presented in Fig. 7: Starting from aqueous solutions of alkali metal silicates (typically water glass, pH>12), the pH of the solution is lowered to the acidic range (pH~2) by addition of strong inorganic acids (e.g. HCl, HNO_3 or H_2SO_4), causing protonation of the monomeric silicate ions to silicic acid $Si(OH)_4$. Due to its instability at concentrations greater than $\sim 2\cdot 10^{-3}$ M, the monomeric silicic acid tends to polymerize to polysilicic acid (sol formation).[32] During further condensation, the size of these primary particles increases until aggregation of the primary particles leads to the formation of a network (gel).[33]

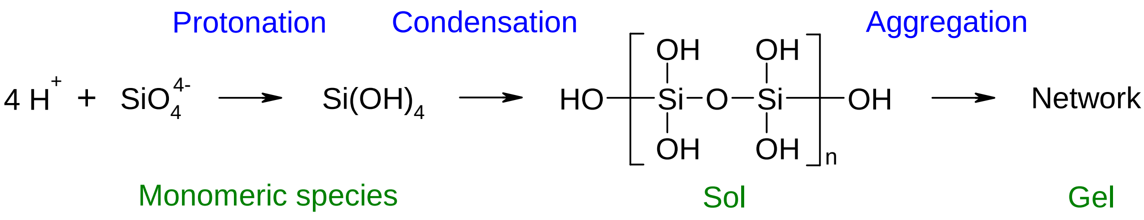

Fig. 7: Reaction steps leading to the formation of a silica hydrogel.[33]

The conditions leading to the formation and growth of the particles are different from those leading to aggregation or gelation. The gelling process is influenced by numerous factors, e.g. the presence of a catalyst, electrolytes and coagulants, as well as the particle size and concentration affect the gelation process.

However, the pH of the solution plays the most important role for the rate of silica sol gelation.[34] While in certain pH regions, the sol provides a fair stability, gelation of pure silica sols proceeds with a maximum rate at pH~5.

Furthermore, the addition of soluble metal salts often enhances the gelling and coagulation by reducing the overall net repulsion effect. Due to their tendency to form condensed small polymeric cations in aqueous solution, highly multivalent metal ions ($M^{3+/4+}$) may behave differently. For example, a cyclic tetramer of zirconium ($(Zr_4(OH)_8(H_20)_8)^{8+}$) initially forms in a concentrated sol and further condenses to form larger polynuclear ions.[35] Under adequate experimental conditions, these types of polynuclear species might react with the silica sol to form complex metal silicate species. Thus, the critical step in this sol-gel synthesis pathway is the preparation of a stable, homogeneous multi-component sol, which subsequently evolves to a solid, homogeneous gel.

Following this sol-gel route, homogeneous gels and glasses were successfully obtained not only in purely silicate based systems [36-38] but also in alkali borosilicate, calcium silicate [39], aluminum silicate [40] as well as in rare earth silicate systems.[41-42]

1.3.2.2.Polymerization of Alkoxy Silanes in Solvent-based Systems

Method 2 of sol-gel processing starts from reacting alkoxy metal precursors in solvent based systems and is much more common in literature. On a molecular scale, the sol-gel process for silicic alkoxides can be described by hydrolysis and condensation reaction steps (cf. Fig. 8), which occur simultaneously and in concurrence.

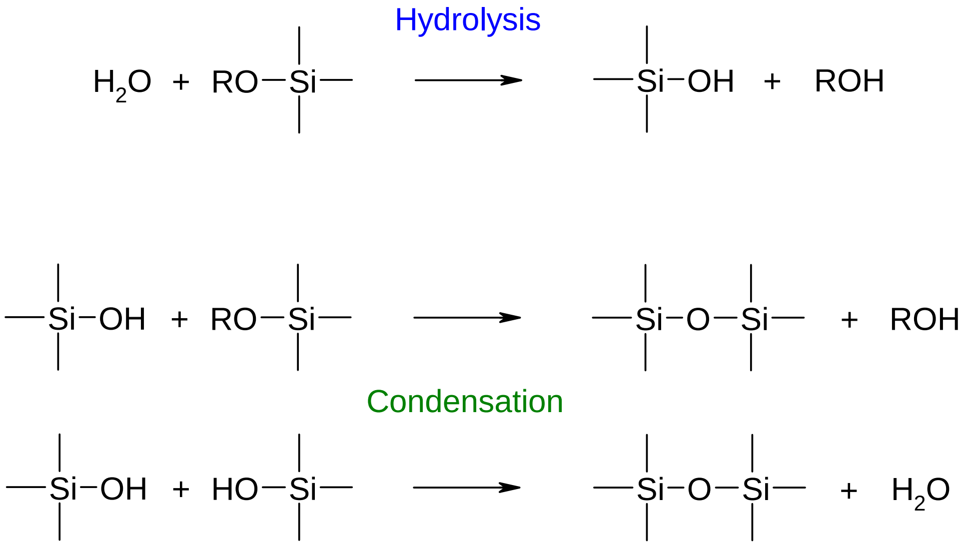

Fig. 8: Hydrolysis and condensation reactions leading to polymerization of alkoxy silanes.

During the hydrolysis step, the Si-OR bond of the alkoxysilane becomes subject to hydrolytic cleavage, giving reactive silanol groups. Subsequent condensation of the Si-OH groups leads to the formation of siloxane bonds. Both, hydrolysis and condensation can be described as a bimolecular nucleophilic substitution reaction, whereas the mechanism depends on the type of catalyst used (acidic or basic).

The back reaction of the hydrolysis, the esterification of the silanol groups, considerably controls the concentration of oligomeric intermediate species in the sol. This process step also follows a S_N2 reaction mechanism and occurs in a higher intensity in acidic media than in a basic milieu.[43] In acidic solvent systems containing alcohols differing from the ones being released during the hydrolysis step, a special esterification reaction, the trans-esterification of alkoxy groups, can be observed.

As for the hydrolysis, back reactions are observed for the condensation process, and siloxane bonds are cleaved depending on the pH of the system. Fission of siloxane bonds preferably proceeds under alkaline conditions, while in acidic media, siloxane bonds are formed more or less irreversibly, as neither disproportionations nor rearrangements occur.[44]

Continued condensation leads to the formation of a three-dimensional, solid gel network of silicon dioxide, consisting of a porous, polymeric network, with solvent molecules (e.g. water or alcohols) incorporated in the cavities of the gel.[45] An illustration of such a gel structure is schematically given in Fig. 9:

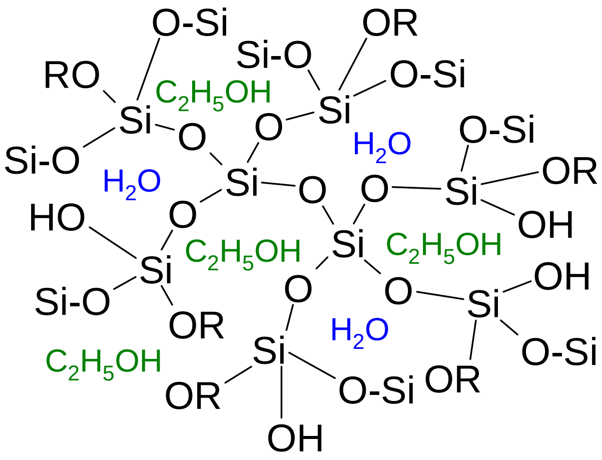

Fig. 9: Schematical illustration of the gel structure

Assuming complete condensation in the resulting gel, the overall reaction is then given as:

$$Si(OR)_4 + 2\ H_2O \longrightarrow SiO_2 + 4\ ROH \qquad (8)$$

The constitution of the resulting polymer is controlled by the relative reaction rates of the hydrolysis and condensation steps, preferentially giving linear chain polymers in acidic media, while basic catalysis favors polycondensation and leads to highly branched polymeric species.[45-49]

The influence of the pH on the reaction rate of both subprocesses (hydrolysis and condensation) is given in Fig. 10.

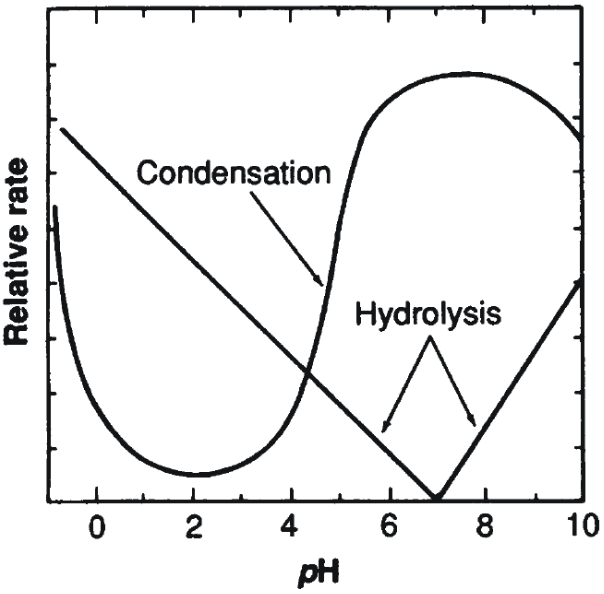

Fig. 10: Relative reaction rates for hydrolysis and condensation in correlation to pH.[50]

At pH values between 2 and 5, condensation is the rate determining step.[50] Monomers and small oligomers with reactive silanol groups coexist in parallel. Further condensation leads to a weakly branched network with small cage-like units. In contrast, hydrolysis determines the reaction rate in basic environments. Growth of the clusters is mainly directed by condensation with monomeric units, resulting in three-dimensional networks with large particles and pores.[51]

Commonly, nitric or hydrochloric acid are used for acidic catalysis, but acetic acid is also often used. For basic catalyzed sol-gel processes, sodium hydroxide or ammonia are commonly used. Both, strong acids and bases generally have a more pronounced influence on the increase of the rate of hydrolysis than weaker acids and bases, while a reversed effect is observed for the condensation reactions.

In general, the sol-gel process does not necessarily require the use of a solvent. However, as alkoxy silanes are hardly miscible with water, preparation requires vigorous agitation by ultrasonification to obtain homogeneous mixtures.[52-54] Control of the subprocesses is more complicated and often yields in shorter gel times of such systems. For this reason, alcohols are commonly used as solvents to easily provide homogeneous solutions and to allow the regulation of the drying process.

2. Structural and Chemical Composition of Silica Gardens

Several studies dealt with structural and chemical *ex-situ* characterization of different hollow silicate garden fibers. In general, these publications focus on the elucidation of three different properties of the precipitated material, in particular the dimensions of the formed tubular structures, the structure of the membrane as well as its elemental composition, and the identification of crystalline material.

2.1. Dimensions of the Tubular Precipitates

Dimensions of traditionally prepared silicate garden tubes exhibit significant variations, especially in their length, which ranges from several millimeters to some decimeters. In contrast, the distribution of their diameters is narrowed and typically situated in the region of several hundred micrometers up to a few millimeters, quite independent of the type of metal salt used (cf. Fig. 11).[6, 18, 24]

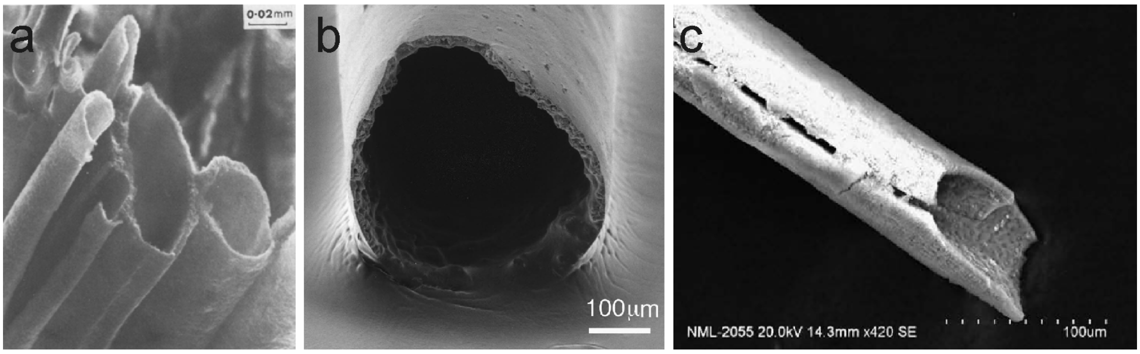

Fig. 11: Silicate garden tubes with diameters ranging from 20-400 µm, prepared from water glass solutions and crystals of (a) ferrous sulfate, (b) copper nitrate and (c) cobalt chloride, respectively. [6, 18, 24]

2.2. Structural and Elemental Composition of the Membrane

By means of scanning electron microscopy, several differently prepared tubular precipitates were analyzed on their structural performance and overall appearance.[17-18, 24] In most cases, the exterior and interior surface of the isolated chemical garden tubes exhibit quite similar basic structures, with a relatively smooth and compact external surface (Fig. 12 a-c), while the inside of the membrane provides rough and textured surfaces (Fig. 12 d-f).

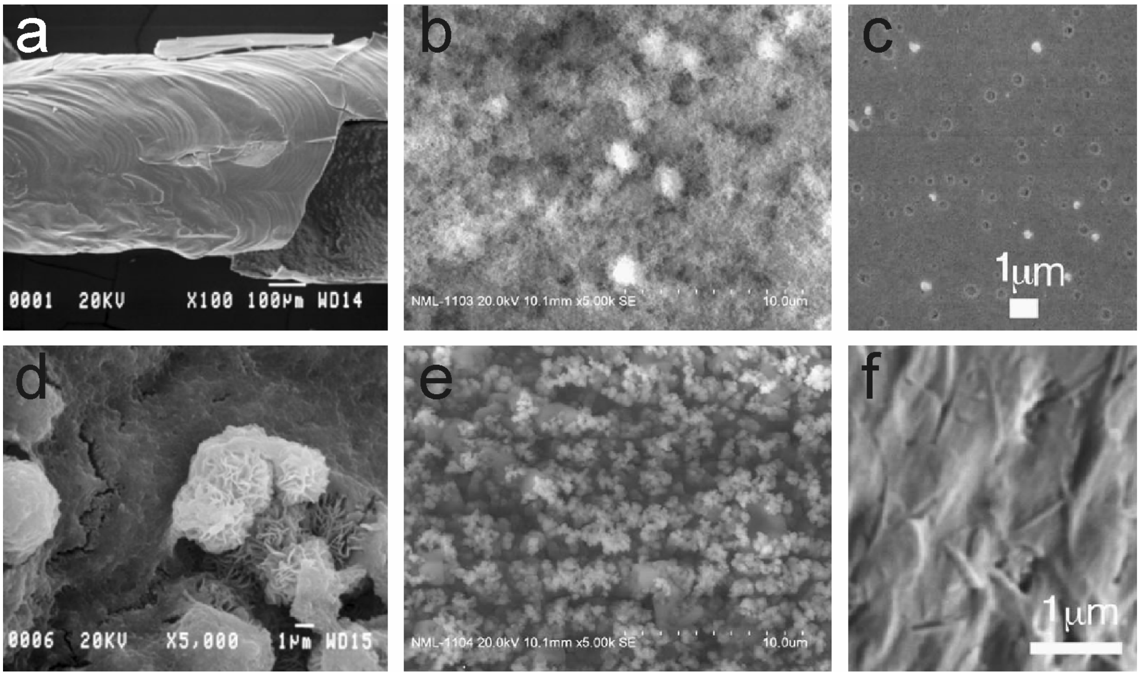

Fig. 12: (a-c) smooth exterior and (d-f) structured interior surfaces of silicate garden tubes prepared from diluted water glass and (a, d) copper sulfate solution, (b, e), cobalt chloride crystals and (c, f) copper nitrate crystals, respectively.[17-18, 24]

SEM pictures taken from the cross sections of two different isolated membrane materials further revealed a rough separation into three different layers (Fig. 13), by this confirming the proposed layered structuring as discussed at the end of section II.1.3. In both cases, the layer previously facing towards the outer silica sol (right side of Fig. 13 a and b) exhibits a condensed and homogeneous appearance, while the former interior surfaces of the membranes provide a porous and rugged layer (Fig. 13, left side). Both layers are separated by an intermediate region, which provides the highest thickness of all three layer types. However, the nature of this interlayer significantly differs for both examined materials.

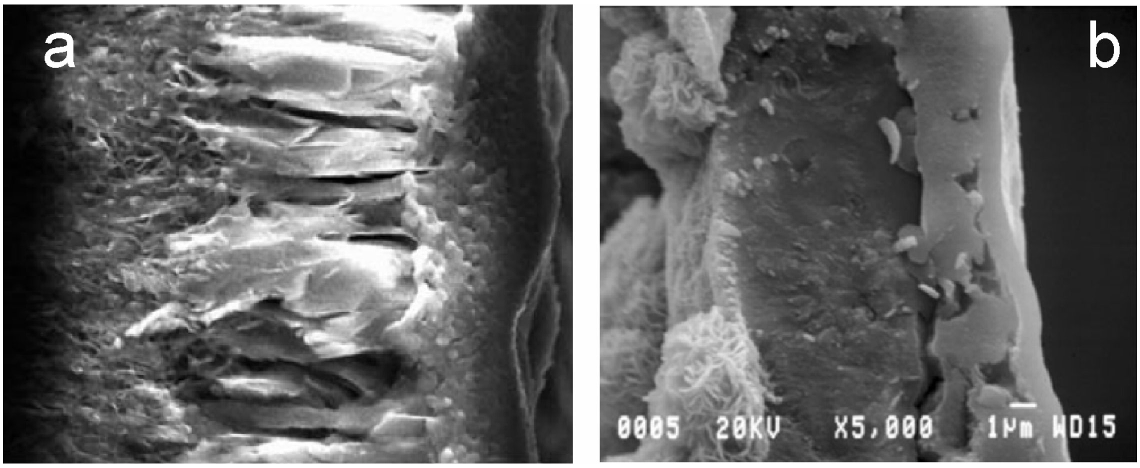

Fig. 13: Cross sections of tube membranes, prepared from diluted water glass and aqueous solutions of (a) zinc sulfate and (b) copper sulfate. Three more or less distinct layers with different structures can be recognized: a smooth and dense exterior (right), a intermediate layer (middle) and a structured and rough interior surface.[17, 29]

Besides the commonly found structuring of the tube interior, two studies also revealed the presence of silicatic microspheres spread on the inner surface of silicate gardens grown from $SrCl_2$, $BaCl_2$ and $NiSO_4$, respectively (cf. Fig. 14).[26-27]

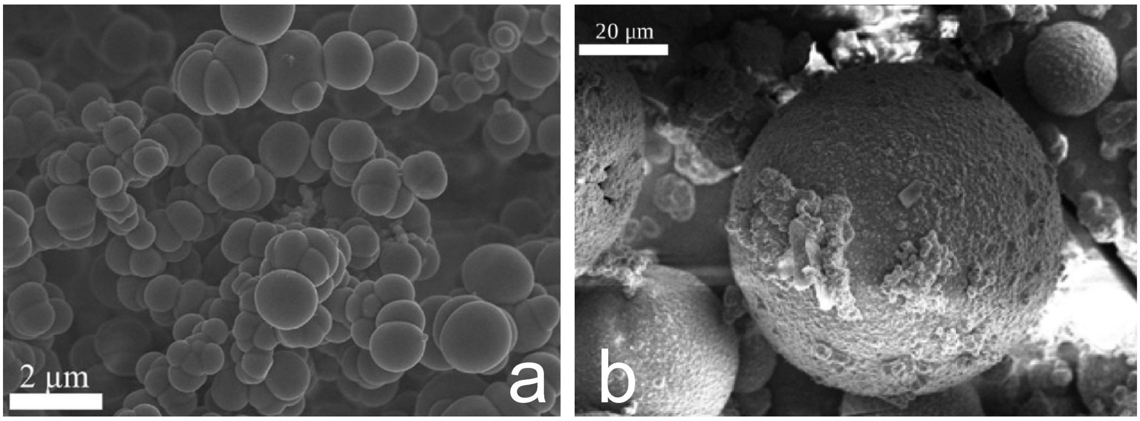

Fig. 14: SEM pictures of silicatic microspheres found on the interior surface of silicate gardens grown from (a) $BaCl_2$ and (b) $NiSO_4$, respectively. [26-27]

By using energy dispersive X-ray spectroscopy (EDX), silicate garden tubes prepared from aqueous solutions of zinc sulfate (Fig. 13a) and copper sulfate (Fig. 13b) were examined on their elemental constitution. [17, 29] Resulting EDX spectra of the interior (Fig. 15 a, c) and exterior (Fig. 15 b, d) surface of both membrane materials feature significant differences in their elemental composition. For both cases, it was found that the exterior surface layers are enriched in silica, while the interior coat mainly consists of metal hydroxide. Similar results were also reported for tubular structures prepared from cobalt chloride crystals,[18] thus indicating that the found tendencies are independent of the applied preparation procedure as well as of the type of used metal salt. In addition to the observed layered structuring of the membrane material, reported EDX data further corroborate the proposed formation mechanism presented in section II.1.3.

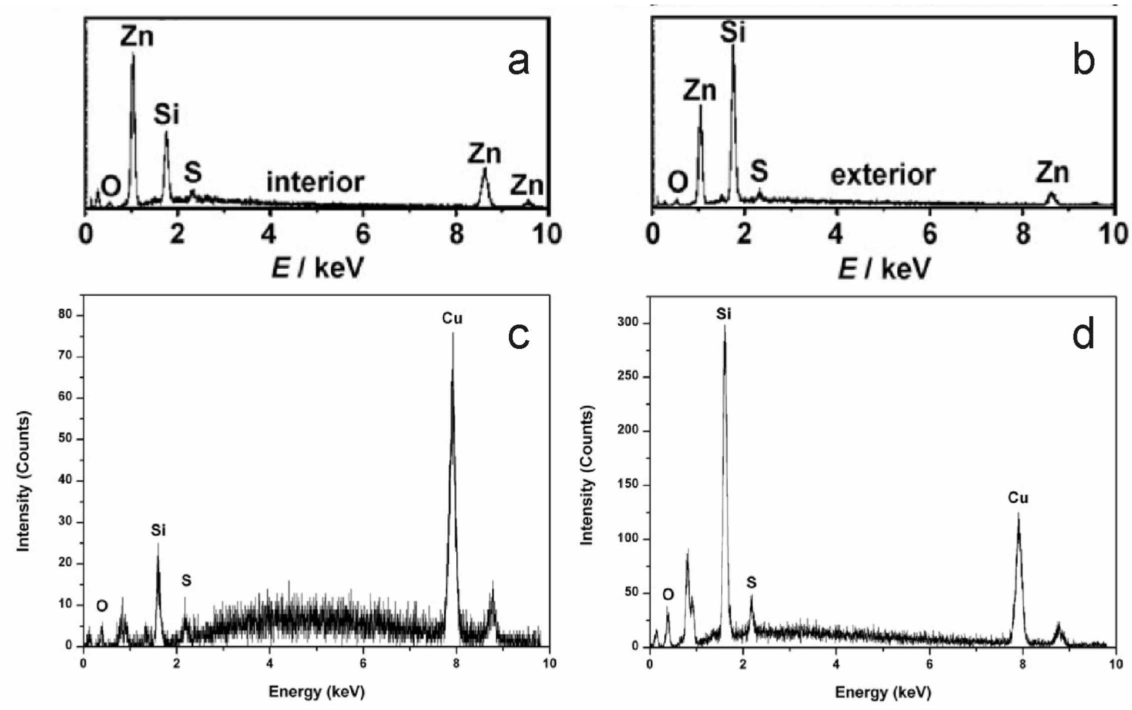

Fig. 15: EDX spectra of (a, c) interior and (b, d) exterior surfaces of silicate garden membranes prepared with aqueous solutions of (a, b) zinc sulfate and (c, d) copper sulfate.[17, 29]

2.3. Investigations on the Crystallinity of the Precipitated Material

Apart from the pure analysis of the elemental composition by EDX spectroscopy, several publications dealt with the examination of isolated and particularly thermally post-treated silicate garden tubes on their crystalline nature by means of X-ray diffraction (XRD) or electron diffraction techniques. Within these studies, it was found that at least some of the examined chemical garden tubes provide fractions of crystalline material. For example, it was found that membrane material precipitated from copper nitrate crystals contains small amounts of copper hydroxide nitrate [$Cu_2(OH)_3NO_3$]

crystals (Fig. 16 a).[24] However, this crystalline material emerged to be not stable against irradiation by electron beam and is rapidly transformed to crystalline copper oxide. Membrane walls which were prepared by the use of a copper sulfate solution also exhibit polycrystalline areas after being thermally treated at 140°C (Fig. 16 b). However, in this case, assignment of the diffraction patterns to a specific crystalline compound remained unsuccessful.[17] A second examination of tubular fibers prepared from $CuSO_4·5H_2O$ crystals and dried at 25°C identified present crystalline fractions as a mixture of $CuSO_4·H_2O$, $CuSO_4·3H_2O$ $CuSiO_3·H_2O$ and possibly $Na_2Cu(SO_4)_2$.[16] In the same study, crystalline matter ($CaO·SiO_2·H_2O$, $CaCO_3$, $Na_2O·8CaO·5SiO_2·7H_2O$) was also observed in precipitates prepared from $CaCl_2$, while tubes formed from $FeSO_4·7H_2O$, $CoCl_2·6H_2O$ and $NiCl_2·6H_2O$ crystals exclusively consisted of amorphous material. Membrane material precipitated by reacting sodium silicate with solutions of zinc sulfate was found to contain fractions of nano meter scaled ZnO crystals when heated to 250°C prior to analysis.[22] The formation of crystalline β-Co_2SiO_4 in silicate garden precipitates prepared with $CoCl_2$ crystals was reported to occur at ambient temperature, being transformed to α-Co_2SiO_4 after heating to 900°C.[18] Crystalline matter was also observed in precipitates prepared from $CaCl_2$ and in diluted water glass. In contrast to the previously presented studies, where crystalline matter was already detectable when precipitates were treated at relatively low temperatures, membrane tubes prepared from ferric nitrate [$Fe(NO_3)_3·9\,H_2O$] remained amorphous until temperatures of $T>650$°C. After thermal treatment at 850°C, crystalline fractions of crystobalite and hematite were finally detectable.[55] Recently, another two studies were published on the crystallization behavior of silicate gardens grown from pressed wafers of metal chlorides or sulfates, containing cations from group 2 (Ca, Sr, Ba)[26] and period 4 (Ca, Mn, Co, Ni)[27] of the periodic table. In the first study, X-Ray analysis revealed the existence of crystalline $SrCO_3$ and $BaCO_3$ in the precipitates, while, in contrast, no crystalline $CaCO_3$ was detected. The presence of crystalline $MnO·H_2O$, $Co(OH)_2$, $Ni_3Si_2O_5(OH)_4$ and hydrated nickel hydroxide was reported in the second study. Crystals of sodium chloride and sulfate were found on the interior surface of the precipitated tubes. As samples were not rinsed with water prior to drying and analysis, found NaCl and Na_2SO_4 crystals were formed during the drying process.

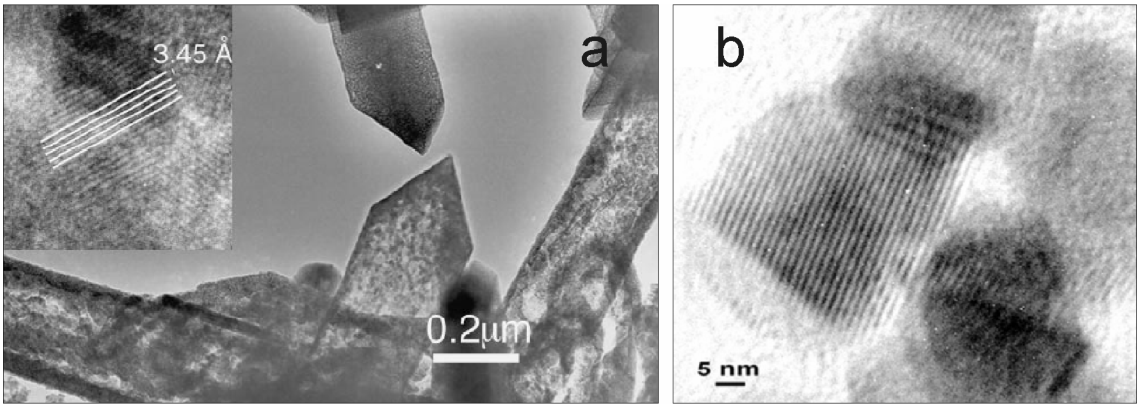

Fig. 16: Pictures of crystalline material obtained by transmission electron microscopy (TEM) on silicate gardens prepared with (a) copper nitrate crystals and (b) aqueous copper sulfate solution, respectively. Crystalline areas in (a) were identified as $Cu_2(OH)_3NO_3$, while assignment of (b) was not possible.[17, 24]

Apart from the cited publications revealing the presence of crystalline fractions incorporated in the precipitated tubes, another study, facing with the examination of tubular membranes precipitated from $Al(NO_3)_3$ crystals in the silicate system, proved the existence of highly ordered silica nanorods with diameters of ~45nm and close-packed hexagonal arrangement (Fig. 17).[19]

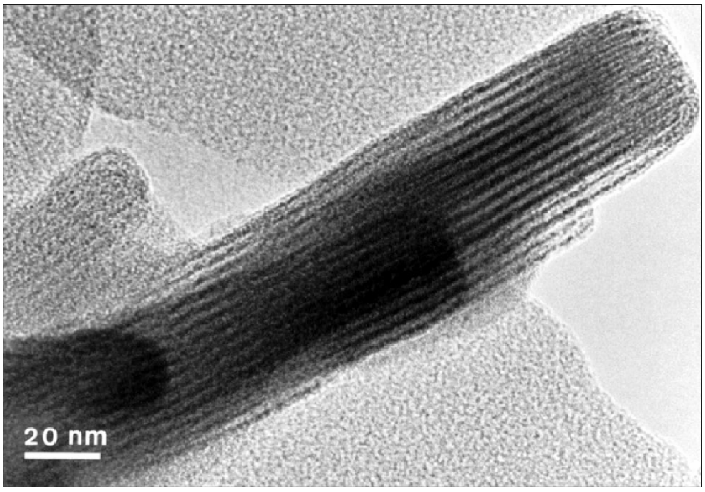

Fig. 17: TEM picture of structured silica nanorods with close-packed hexagonal arrangement in tubular precipitates prepared from $Al(NO_3)_3$ crystals and dried at 45°C.[19]

Comparison of these published data has shown that the formation of crystalline material not only strongly depends on the sort of metal cation, but also on the type of counter ion as well as on the conditions of preparation or post-treatment, thus rendering a general statement of crystallization processes in silicate gardens impossible.

3. Control and Design of Chemical Garden Growth

A third area of research is devoted on controlling and designing the shape of chemical gardens. Early attempts towards structural changes were made by simple modifications of the experimental procedure.

3.1. Influence of Silicate Concentration

First of all, Coatman et al. have shown that the silicate concentration is an important factor for silicate garden growth and strongly affects the shape and growth behavior of resulting precipitates.[6] In a series of experiments, the silicate concentration was altered by dilution with varying fractions of water and subsequently, crystals of cobalt nitrate were added to the different mixtures. It was found that, for a given salt type, there is an optimum range of silicate concentration that produces the capillary growth most effectively (cf. Fig. 18).

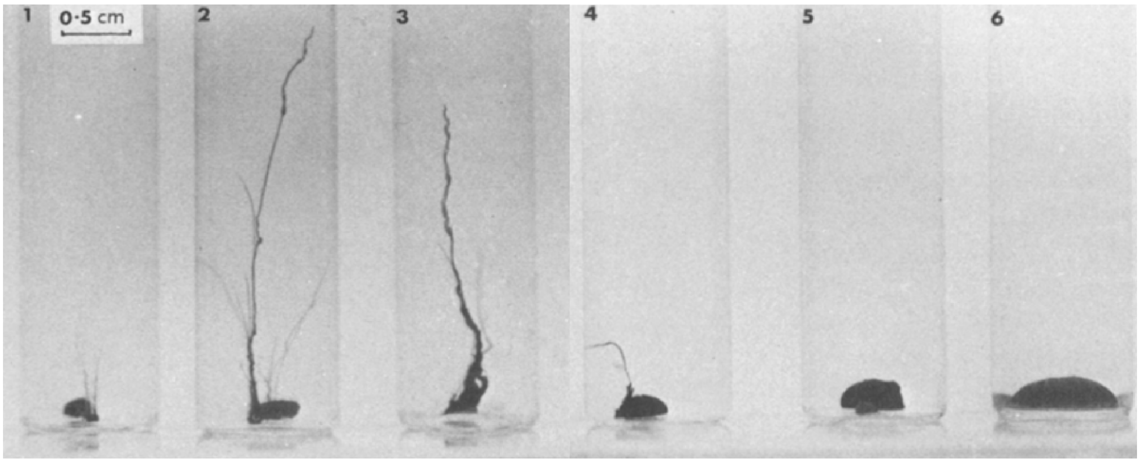

Fig. 18: Silicate garden growth from cobalt nitrate crystals in sodium silicate at different silica concentrations. Water glass (7 M with respect to silica) was diluted by the following amounts: (1) 1:2, (2) 1:4, (3) 1:8, (4) 1:16, (5) 1:32, (6) 1:64.[6]

In concentrated solutions of silicate, a dense, tight-fitting shell is formed around the seed crystal and this seems to rupture only with difficulty to produce tubular growth. At the other extreme, as the silicate solution is diluted by higher ratios, the gel membrane becomes less rigid and more and more increases in its elastic nature. Due to the decreasing density of the silicate solution, buoyancy of the enclosed metal salt solution is diminished. As a consequence, fibrillar and vertical growth commences and formation of globular excrescences caused by repeated rupture and re-healing of the elastic gel membrane is favoured. Finally, with increasing dilution, the precipitated material fails to cohere properly and instead forms a flocculent spongy mass around the dissolving seed crystal.

3.2. Use of Aqueous Metal Salt Solutions

A second modification of the classical setup was realized by several groups, replacing the solid metal salt crystals by concentrated salt solutions. In a first attempt, concentrated metal salt solutions were layered over diluted water glass. As result, pseudopodia-like, capillary-shaped or tube-like architectures were generated.[56] It took nearly 100 years, until this basic concept was re-used and successfully implemented for the preparation of comparably thin hollow tubes with well defined diameters. This was achieved by injecting concentrated metal salt solutions directly into diluted water glass under carefully controlled conditions.[8-10]

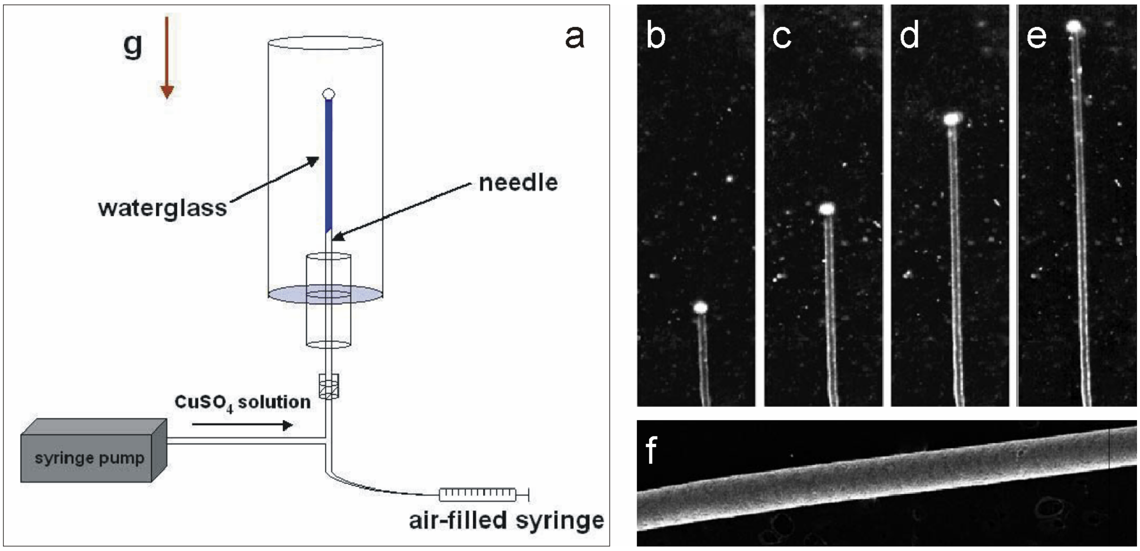

Fig. 19: (a) Schematical drawing of the experimental setup used for bubble-guided growth of uniform tubular precipitates (b-f) by injection of copper sulfate solution into diluted water glass.[22, 29]

A further enhancement of the tube uniformity was achieved using an advanced procedure which involves the injection of a tiny gas bubble into the diluted water glass prior to inducing the concentrated metal salt solution (Fig. 19a). Due to buoyancy effects, the gas bubble attached at the tip of the precipitating tube directs the tube growth in a precisely vertical direction so that straight tubules with uniform dimensions are obtained (Fig. 19b-f).[22] Similar structures were also obtained in the reverse case, when sodium silicate solution was injected into a cupric sulfate solution.[11]

3.3. Influence of Polymeric Additives

The morphology of chemical garden precipitates can also be tuned by polymeric additives.[57] In a silicate-free system, addition of $FeCl_3$ seed crystals to aqueous solutions of potassium hexacyanoferrate(II) trihydrate containing various amounts of cellulose hydroxyethyl ether results in a series of different growth scenarios, which crucially depend on the molecular weight of the polymeric cellulose hydroxyethyl ether. While only slight changes of the classical growth behavior were observed for hexacyanoferrate solutions containing polymers with low molecular weight, rather surprising results were obtained in solutions based on high molecular weight polymers.

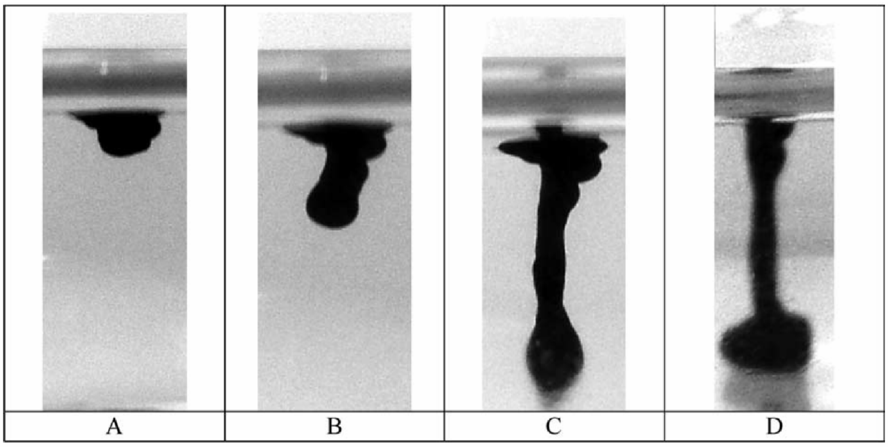

Fig. 20: Inverse and down-directed growth of filaments composed of Berlin blue ($Fe[FeFe(CN)_6]_3$) in aqueous solutions of $K_4[Fe(CN)_6]$ containing polymeric cellulose hydroxyethyl ether (M_w = 140.000-160.000, c = 1 wt%).[57]

In these cases, due to the high viscosity of the solution, the seed crystal did not sink to the bottom of the vessel but kept floating on the liquid-gas interface and an inverse, down-directed outgrowth of Berlin blue ($Fe[FeFe(CN)_6]_3$) filaments occurs (Fig. 20).

3.4. Exposure to Magnetic and Electric Fields

3.4.1. Helical Growth by Strong Magnetic Fields

The influence of strong magnetic fields on the growth behavior of precipitating membranes prepared from Mg(II), Zn(II), Mn(II) Cu(II), Co(II), Ni(II), Fe(II) or Fe(III) salts in the silicate system was examined by several groups.[12-14, 58] In most of these studies, the experimental setup correlates to Fig. 21.

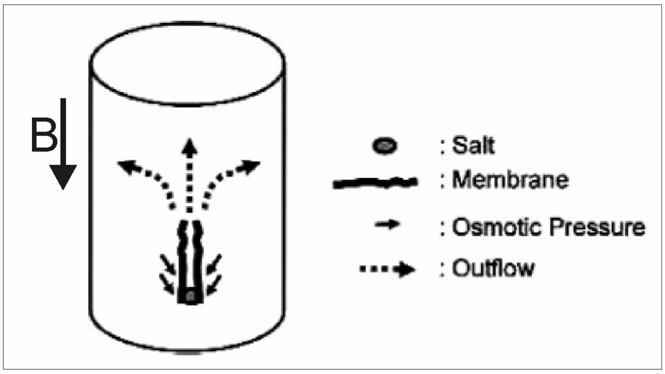

Fig. 21: Mechanism of membrane tube formation showing the outflow of anions from the tube interior. Left arrow indicates down-directed magnetic field.[13]

A metal salt crystal was placed in a glass vessel which was subsequently filled with diluted water glass. Formation of tubular membranes was either performed in absence of a magnetic field or under a vertically and down-directed field of 15 T by mounting the glass vessel in the center of a superconducting magnet.

Five different experiments were performed for each type of metal salt, always producing identical results regardless of the magnetism of the metal salts:

1. Growth of vertical membrane tubes without any signs of chirality was observed in the absence of a magnetic field (Fig. 22a).
2. Helical growth of membrane tubes with right-handed chirality was obtained when the metal salt crystal was placed near the vessel wall (Fig. 22b).
3. Left-handed helices of precipitated tubules result from experiments in which the metal salt crystal is placed near the outer surface of a thin graphite rod centered in the vessel (Fig. 22c).

4. Tubular precipitates also grow with left-handed chirality when metal salt crystals are placed in the center of the vessel in the absence of a graphite rod and thus far away from any boundary surface (Fig. 22d).
5. Reversed helix chiralities were observed when the direction of the magnetic field was changed from down- to upward.

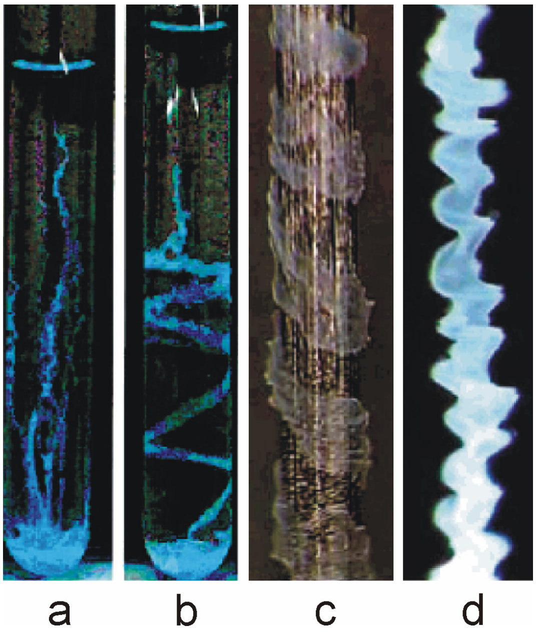

Fig. 22: Growth behavior of membrane tubes grown (a) in the absence of a magnetic field; (b) near the inner surface of the vessel wall; (c) on the outer surface of a graphite rod immersed into the center of the vessel; (d) in the center of the vessel without the influence of a boundary surface. The magnetic field was 15 T and down-directed during growth of b-d.[13]

A boundary-assisted magneto hydrodynamics (MHD) mechanism was found to sufficiently explain all the observed results. In the MHD mechanism, convection of the solution is induced by the Lorentz force on moving ions in a solution exposed to a magnetic field (MHD-induced convection). The boundary-assisted MHD mechanism is the mechanism in which a boundary posed by a wall or a surface serves an important role in determining the direction of MHD-induced convection.

During tube growth, metal salt solution flows out from the opened top of the tube and precipitates as new membrane material at the tube exit. By this reaction, a stream of ionic solution is induced in the tube interior (cf. Fig. 21), containing both positively charged metal and negatively charged counter ions. However, due to rapid precipitation of the metal ions with hydroxyl and silicate ions at the hollow tube exit, the ejecting solution may be transiently and locally enriched with the negative counter ion. (The resulting excess of negatively charged counter ions is rapidly neutralized by diffusion of Na^+ ions to the outflow). Therefore, convection is primarily induced by the negative counter ions in the outflow, spreading horizontally and vertically outward (cf. Fig. 21). In contrast to the vertical outflow, the horizontal motion of the solution enriched in negative counter ions, which is perpendicular to the magnetic field, is affected by the Lorentz force F_L, given by the following equation:

$$F_L = qv \times B \tag{9}$$

where q is the charge of an ion, v is its velocity, and B is the magnetic field flux density.

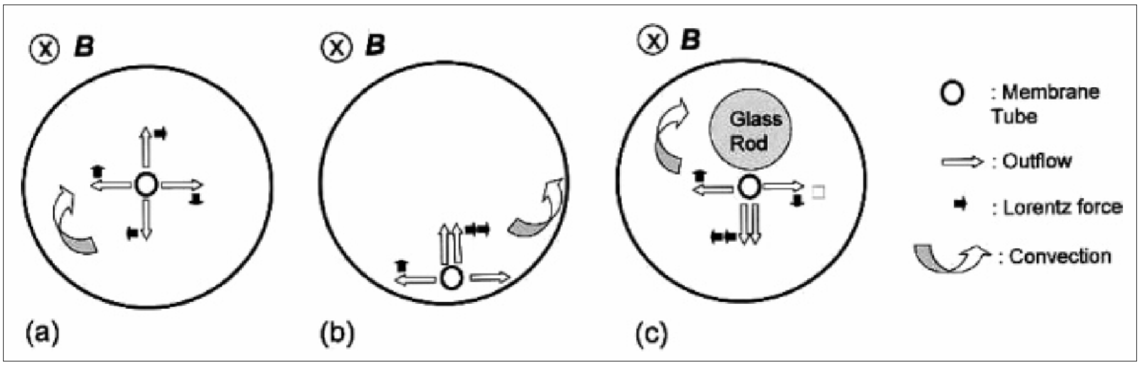

Fig. 23: Mechanism of helical twisted membrane tube formation in a magnetic field (top view): A tube grown (a) apart from the vessel wall, (b) near the vessel wall and (c) near a glass rod's outer surface.[13]

As the magnetic field is directed downward, the direction of the Lorentz force is left-handed, as shown in Fig. 23a. As the tube apart from the vessel wall grows under the steady influence of the left-handed convection, helical tubes with the left-handed twist originate (Fig. 22d). In contrast to this undisturbed induced convection, the motion of the outflow near a surface is influenced by its boundary.

When a tube grows near the inner surface of a vessel wall, the direction of the outflow is limited (cf. Fig. 23b). As a consequence, the outflow moves along the wall in a right-handed direction, thereby inducing convection and tube precipitation in a right-handed chirality.

Reversed restriction of the induced convection is observed when a hollow tube grows near the outer surface of a graphite rod (Fig. 23c). In this case, the outflow moves in the left-handed direction along the outer surface of the rod, thereby inducing left-handed convection and formation of clockwise rotating helical tubes.

3.4.2. Directed Growth by Electric Fields

Micrometer-scale tubular structures were also prepared by placing polyoxometalate-based inorganic crystals into aqueous solutions containing organic polyaromatic cations. By applying a voltage across the solution soon after tube initiation, directional control could be achieved and the forming tubes can be repeatedly turned through 180° by using a two-electrode set-up. Inverting of the polarity of the electrodes induces the directional change of tube growth (see Fig. 24).[59]

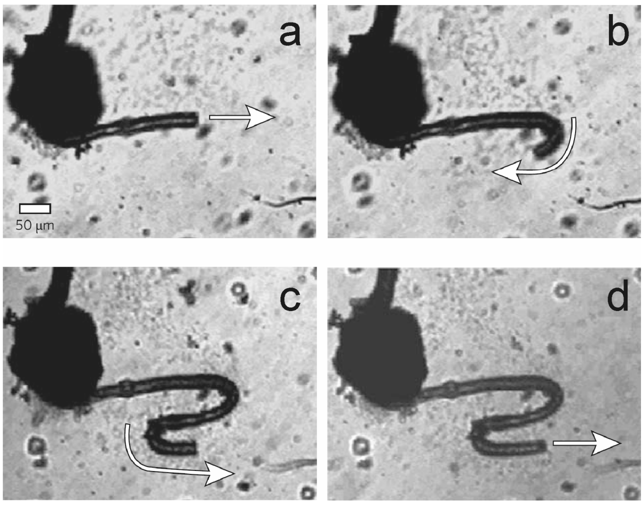

Fig. 24: Control of tube growth direction by applying an electrical field in a two-electrode system. Inversion of the polarity of the electrodes induces directional change of tube growth.[59]

3.5. Growth of Silicate Gardens in the Absence of Gravity

Chemical gardens were also successfully synthesized in space in the absence of gravitational forces. Under these conditions, kinetics were found to be slowed down and became diffusion-limited as effects driven by buoyancy were not active.[15, 60-61] SEM images of silicate gardens prepared in microgravity from $CoSO_4$ and $MnCl_2$ show that the familiar upward-directed tubular growth behavior is not merely observed under gravitational conditions but also develops in microgravity (see Fig. 25). However, randomly oriented tubular growth results under this condition, while in contrast gardens grown on Earth predominantly exhibit vertical directed tube growth.

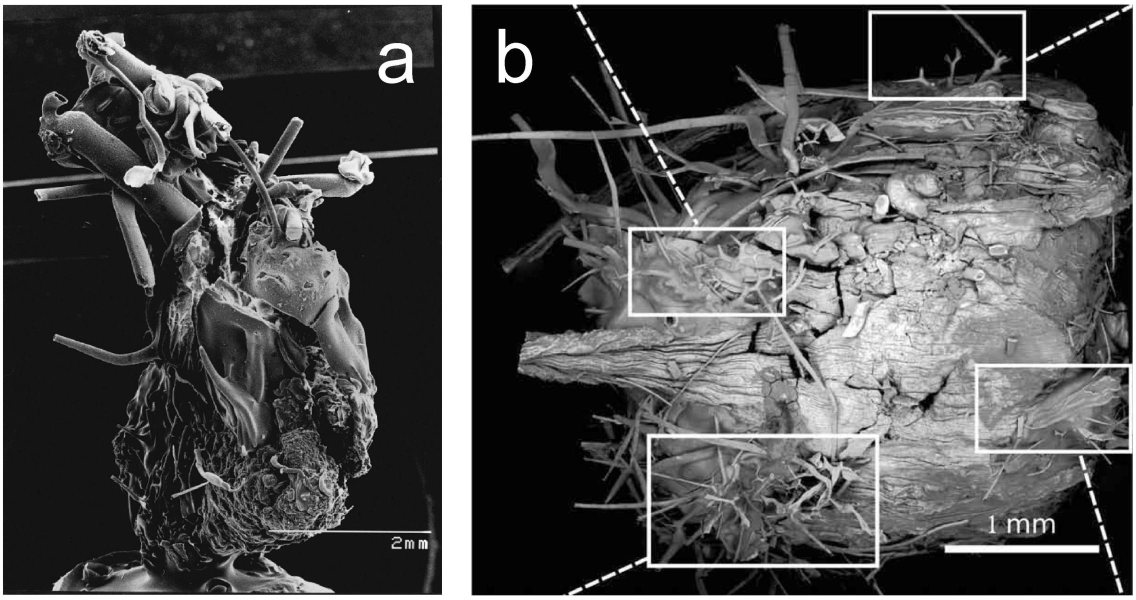

Fig. 25: SEM images of isolated silicate gardens grown from (a) $CoSO_4$ and (b) $MnCl_2$ under microgravitational forces.[15, 61]

Due to elimination of buoyant effects, growth exclusively proceeds with forced convection driven by osmotic pressure. The slower growth under microgravity also indicates a different type of growth that Jones and Walter named “plastic deformation”, in contrast to typically tubular growth. Plastic deformation results in a pronounced swelling of the initial membrane, which remains fluid for a relatively long time due to changes in the kinetics of metal hydroxide precipitation. As density-driven convection is only present in gravitational environment, the boundary layers on both sides of the initially precipitated silica-rich membrane deplete in their precipitant reagents and precipitation processes become diffusion-limited. Therefore, hardening of the membrane is significantly retarded. Further, it is worth mentioning that tubular growth proceeds in oscillations also in the absence of gravity, having similar dimensions as observed for garden growth on Earth. Concerning their chemical compositions, silicate gardens grown from identical metal salts in microgravity and under conventional conditions do not exhibit significant differences in the chemical composition. However, the compositional gradient between the elemental composition of the interior and exterior layer was found to be less pronounced in the absence of gravity.

4. Functionalization of Chemical Gardens

In view of feasible, specially tailored applications for these self-assembled materials, other work focused on the exploration of chemical gardens as suitable catalysts or reactors in simple syntheses.

For example, iron (III) silicate tubes prepared from $Fe(NO_3)_3 \cdot 9H_2O$ appeared to be a promising adsorbent for Zn(II), Pb(II) and Cr(III) in aqueous medium, with loading capacities ranging from 24-35 mg g^{-1}.[55]

Collins et al. demonstrated that silica gardens prepared with $Al(NO_3)_3$ seed crystals act as strong Brønsted acids, when being post-treated by ion exchange processes and subsequent calcination at 530°C. Although the population of Brønsted acid sites in the H^+-exchanged samples were found to be lower than in commercial amorphous aluminosilicates, catalytic tests revealed that calcinated samples have stronger acid sites, and might hence serve as an alternative to the commercially available aluminosilicate catalysts.[20-21]

Steinbock et al. demonstrated that silica/ZnO tubes provide significant photocatalytic properties, which can be used for accelerating the photodegradation of the dye rhodamine B under UV irradiation. Silica/ZnO tubes were prepared from zinc(II) sulfate and diluted water glass and subsequently treated at 250°C to form crystalline ZnO nanoparticles incorporated into the silicate matrix.[22]

Eventually, Maselko et al. prepared a chemical garden by immersion of a mixed pellet of calcium and copper chloride in an aqueous brine of sodium carbonate and dissolved starch and used it simultaneously as reactor and catalyst for the synthesis of iodine from hydrogen peroxide and sodium iodide inside the membrane walls.[62] Results indicated that the chemical reactions inside the cell can be described by the following equations, with Cu^{2+} acting as catalytic species:

$$2\,Cu^{2+} + 2\,I^- \longrightarrow 2\,Cu^+ + I_2 \tag{10}$$

$$Cu^+ + H_2O_2 \longrightarrow Cu^{2+} + OH^\bullet + OH^- \tag{11}$$

$$2\,OH^\bullet + 2\,I^- \longrightarrow 2\,OH^- + I_2 \tag{12}$$

The net reaction is

$$H_2O_2 + 2\,I^- \longrightarrow 2\,OH^- + I_2 \tag{13}$$

From UV-Vis spectroscopy, recording the increasing violet colour of the generated iodine-starch complex at 504 nm, it was shown that the iodine formation can properly be described by a first-order kinetics,

$$c_{I_2}(t) = \frac{1}{2}\,c^0_{I^-} \cdot \left(1 - e^{-k_{eff} t}\right) \tag{14}$$

with $c^0_{I^-}$ as the initial concentration of iodide present in the system and k_{eff} as the effective rate constant. The value of k_{eff} was found to increase proportionally with the catalyst concentration ($c_{Cu^{2+}}$), stemming from various copper contents in the mixed pellets.

5. Relevance of Chemical Gardens and Related Phenomena in Practice

Apart from purely scientific fascination for these exceptional examples of pattern formation, chemical garden-like phenomena were also found to occur in the course of iron and steel corrosion,[6, 63-64] Portland cement hydration,[6, 65-69] and the generation of ferrotubes[70] or hydrothermal vents.[71-73] In all these cases, spontaneous precipitation of an inorganic membrane leads to a separation of media with highly dissimilar composition, thus establishing considerable concentration and pH gradients and, occasionally, pronounced potential differences across the membrane.[71] This section will give a short introduction to the underlying mechanism found for the emergence of the different related phenomena mentioned above.

5.1. Hydration of Portland Cement

Processes similar to those involved during the formation of silicate gardens were found to be at work during the hydration of Portland cement.[65-69] Addition of water to Portland cement paste slowly promotes, on a microscopic scale, the formation of fibrillar structures on the exterior surface of the isolated cement granules, which mainly consist of tricalcium silicate (Ca_3SiO_5). Proceeding growth of these fibrillar structures within periods of several hours to days finally results in an interlocked network and thus to the solidity of the hardened concrete. Fig. 26 shows in a series of SEM pictures the formation of as described tubular filaments on the surface of Portland cement granules.

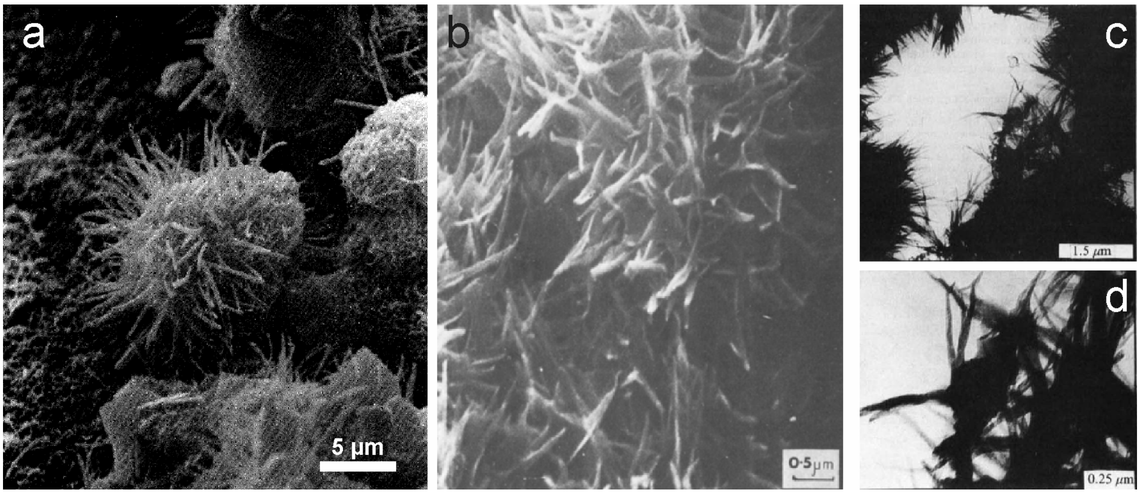

Fig. 26: SEM pictures from independent studies showing fibrillar growth produced during the hydration of Portland Cement paste (a, c, d) and its major constituent tricalcium silicate (b), respectively.[6, 65, 68]

By these systematic observations, the mechanism of Portland cement hydration was elucidated, proceeding in several steps (cf. Fig. 27):[68]

Upon addition of water to cement paste, which mainly contains tricalcium silicate, an initial gel-like layer forms around each grain. Calcium from the grain is leached out into the bulk aqueous phase and the formation of a calcium depleted layer consisting of amorphous silicate gel is observed. This layer increases in depth as hydration proceeds. The leaching-out process increases the pH of the exterior bulk solution to highly alkaline regions (pH~12.5) and leads to a supersaturation of the solution with $Ca(OH)_2$ as well as to a proposed transformation of orthosilicate anions to disilicate anions. At this point, a membraneous precipitate of calcium silicate hydrate (C-S-H) is formed at the surface of the calcium depleted silicate layer. By a combination of in-diffusion of water through the C-S-H layer into the grain and ongoing out-diffusion of calcium ions into the surrounding aqueous phase, the osmotic pressure is increased within the C-S-H membrane eventually causing its rupture. Subsequent ejection of concentrated silicate sol into the supersaturated bulk produces the observed tubular excrescences by continuous precipitation of C-S-H.

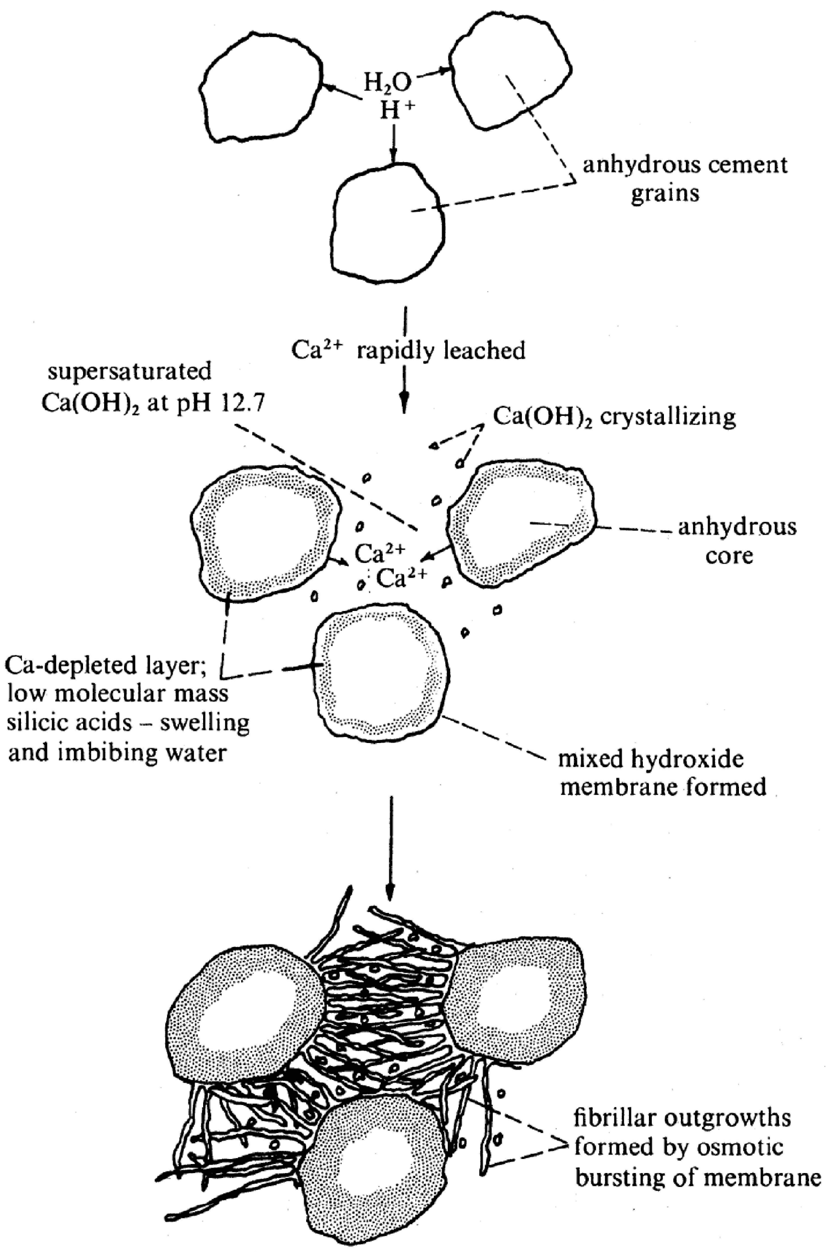

Fig. 27: Schematic model for the hydration and setting of Portland cement.[68]

Thus, the early stages of Portland cement hydration can be summarized by the following chemical reactions:

$$\text{cement grains} + \text{water} \longrightarrow \underset{\text{(surface)}}{\text{orthosilicate anions}} + \underset{\text{(dissolved)}}{\text{calcium hydroxide}} \tag{15}$$

$$\underset{\text{(surface)}}{\text{orthosilicate anions}} \xrightarrow{\text{pH}\approx 12.6} \underset{\text{(surface)}}{\text{disilicate anions}} \tag{16}$$

$$\underset{\text{(surface)}}{\text{disilicate anions}} + \underset{\text{(dissolved)}}{\text{calcium hydroxide}} \longrightarrow \underset{\text{(formed membrane)}}{\text{C}-\text{S}-\text{H}} \tag{17}$$

From this point of view, the chemistry involved in the hydration of cement can be interpreted as an analogon to a reverse silicate garden, based on the observation that a network of calcium silicate hydrate filaments developed from solid tricalcium silicate in contact with aqueous solutions containing metal ions.

5.2. Formation of “Whiskers” and “Ferrotubes”

Further, chemical garden structures appear to play an important role as well in the field of corrosion, given that deposits with tubular morphologies were identified on the surface of rusting steel or iron under certain conditions.[63-64, 74-76] It was found that during long-term exposure of steel tubes to a constant flow of alkaline, carbonate rich water, corrosion processes on the internal surface of the steel tubes lead to the slow and constant deposition of tubular iron oxide “whiskers” as a result of redox processes.[77]

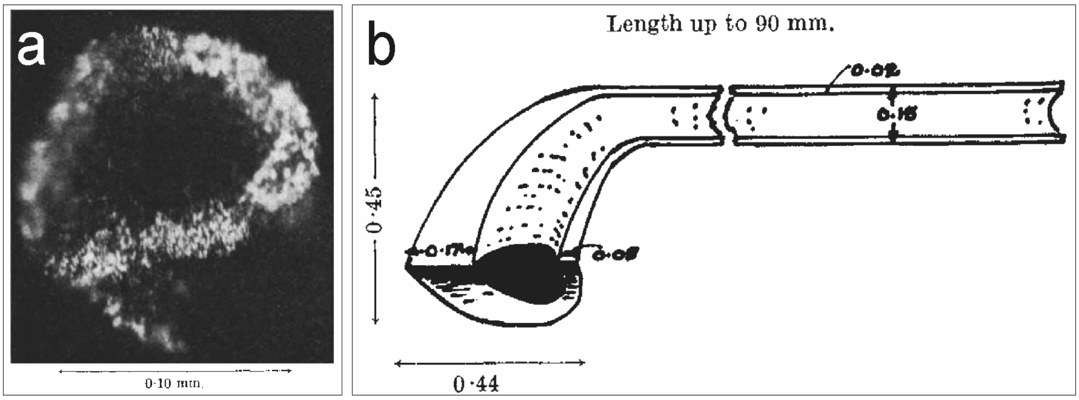

Fig. 28: (a) Photograph showing the cross-section of a whisker. (b) Longitudinal section of a whisker (dimensions in mm).[77]

In the early stages of corrosion, an adherent carbonate layer is deposited on the steel tube interior from the hard water. Subsequently corrosion of iron takes place at local anodic points, generating ferrous ions (Fe^{2+}) and hydroxide ions in the presence of oxygen which readily react with each other to form corrosion products (iron(II)/(III) hydroxides/oxides). However, while in stagnant solution localized corrosion commonly results in the formation of hemispherical domes of corrosion products, the shape of the forming precipitate is significantly disturbed under the influence of vigorous water flow. In this way, hollow tubes are generated which are bent towards the direction of flow. In the course of whiskers formation, ferrous ions, formed at the anodic area at the root of the whisker, diffuse along the tube and become oxidized to Fe^{3+} when coming in contact with the aerated water at the tip of the whiskers tube, leading to a steady precipitation of iron oxide/hydroxides (Fe_3O_4 (magnetite) and FeOOH (goethite)) and thus to an enlargement of the tubuli. A photograph of the cross section of a whisker and a schematic drawing of a whisker with its typical dimensions are given in Fig. 28.

The formation of "ferrotubes" was reported as another self-organized periodic templating mechanism, producing tubular structures electrochemically in iron-ammonium-sulfate solutions.[70] In these experiments, tubular structures grow from the templating action of mixed hydrogen and ammonia gas bubbles, produced at the cathode of an electrochemical cell containing aqueous mixtures of $Fe(NH_4)_2(SO_4)_2 \cdot 7\,H_2O$ and $Fe(NH_4)(SO_4)_2 \cdot 12\,H_2O$. These bubbles support a precipitative film formed at the gas–solution interface. Detachment of the bubbles leaves behind a ring of material that contributes to the tube growth. By repeated bubble formation and detachment, ferrotubes composed of iron hydroxide with varying composition are formed (see Fig. 29a). By variation of the applied current, the tube diameter of the precipitates could be easily controlled (Fig. 29b), while bent ferrotubes were successfully obtained by exposing to a statically magnetic field (Fig. 29c).

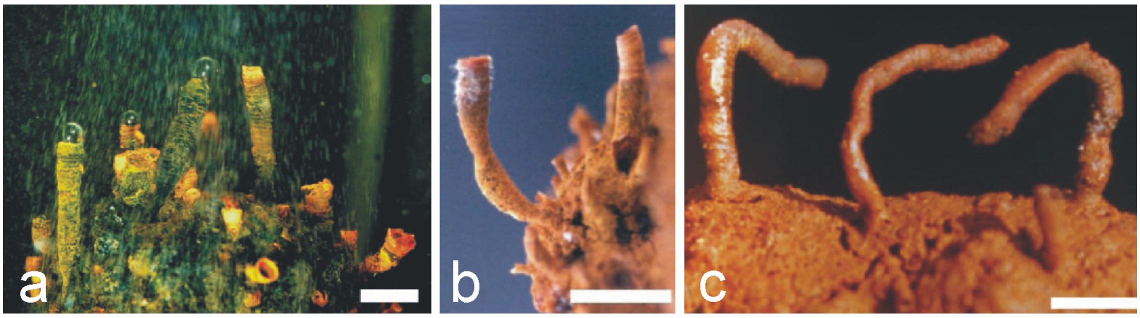

Fig. 29: Photographs of ferrotubes growing in iron-ammonium sulfate solutions with different tube morphologies: (a) Bubble guided growth of ferrotubes under constant conditions. (b) Variation of tube diameter by decreasing (narrow region) and re-increasing (wider upper half of tube) the applied current. (c) Growth of bent tubes under the influence of an external magnetic field (scale bars: 0.5 mm).[70]

Growth of these Ferrotubes is proposed to proceed in five fundamental subsequent stages, starting at the base of the tube and moving up (see Fig. 30). (*i*) Reduction of water and H^+ occurs at the surface of the cathode, producing OH^- and H_2 gas. In addition, NH_3 gas is formed by deprotonation of ammonium ions. (*ii*) The mixed gases move up through the tube as individual bubbles and act as mechanical pumps, pushing the very basic solution up and out of the open top. (*iii*) When bubbles reach the tip of the open tube, the interior basic solution and ammonia react with the exterior acidic, ferrous solution. As a result, green rust ($Fe(OH)_2$) precipitates around the rim and over the surface of the bubble as a thin film. (*iv*) The bubble detaches, leaving a ring of deposited material around the rim. (*v)* Green rust quickly transforms to magnetite within the tube and oxidizes to lepidocrocoite on the outside. As a consequence of these oxidation processes, the walls of these precipitated tubular structures also exhibit a quite layered composition, similar to the silicate garden walls (cf. section II.1.3.1 and II.2.2).

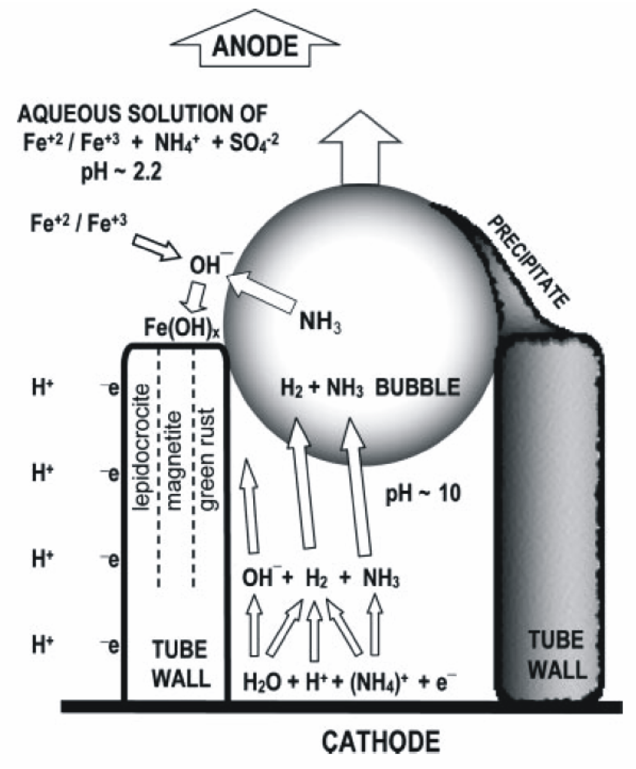

Fig. 30 Mechanisms involved in tubular precipitation of ferrotubes, templated by bubbles.[70]

It was further demonstrated that significant gradients in ion concentration and pH prevail across the precipitated ferrotube wall, separating an alkaline interior ammonia solution ($pH \geq 10$) from an exterior, acidic, ferrous solution ($pH \leq 2.5$). Found conditions correspond to a reversed situation as found in classical silicate garden systems. Interestingly, from a mechanistic point of view, this system also represents a phase-reversed version of soda-straw growth in caves. However, with grow rates of millimeters in tens or hundreds of minutes these structures are formed orders of magnitude faster than their geological counterparts.

5.3. Formation of Deep-Sea Hydrothermal Vent Systems and their Possible Relevance for the Origin of Life

5.3.1. Black Smoker Chimneys

During deep-sea exploration activities in the late 70s of the last century, hitherto unknown hydrothermal vent systems were discovered at depths of around 3000 m below sea level on the deep-sea floor located near and along active spreading centers of the global mid-ocean ridge spreading network on young, hot basaltic crusts.[78] The discovered vent systems comprise active hydrothermal chimneys with dimensions of up to 10 m in height and >50 cm in diameter, emitting hot (>300°C) and supercritical aqueous solutions which become black coloured by precipitation of small particles of iron, zinc, copper and nickel sulfides (see Fig. 31a). Due to their appearance, these tubular chimneys were named and became famous as “Black Smokers”.

Black smokers are located near volcanic activities and result from the seepage of seawater through cracks in the seafloor and its subsequent heating at depth by hot or molten basaltic rocks to temperatures >400°C.[79] By chemical exchange with the hot basaltic rock, the superheated fluid becomes acidic (pH 2-5) and enriched in dissolved metals (Cu, Zn, Fe, Ni) and gases (mainly H_2S and CO_2) (cf. Tab. 1). Subsequently, the hydrothermal fluid re-ascends buoyantly from the underground to the surface of the sea floor. At this point, the heretofore clear and acidic hot vent fluid comes in contact with cold (2°C) and alkaline (pH~8) sea water, and fine-grained particles of metal sulfides and sulfates instantly precipitate, thus changing the optical appearance of the ejecting vent fluid from transparent to deep-black. The generated metal sulfide and sulfate particles deposit as a metal rich sediment layer on the rim of the hydrothermal vent as well as in the surrounding area of the hydrothermal chimney, consequently contributing to the continuing growth of the tubular Black smoker chimneys.

5.3.2. “Lost City” Calcium Carbonate Hydrothermal Vent Systems

In the year 2000, a second type of hydrothermal vent system was discovered by Kelley et al. located at the Lost City Hydrothermal Field (LCHF) on the seafloor mountain Atlantis Massif at a depth of only ~700 m below sea level.[80-83] The LCHF comprises about 30 white chimneys with a height of 30-60 m as well as a number of smaller chimneys, all of them composed of calcium carbonate (see Fig. 31b). In contrast to black smoker systems, the chimneys within Lost City are nearly monomineralic (Tab. 1) and predominantly composed of the carbonate minerals aragonite and calcite ($CaCO_3$). During aging of the deposits, aragonite is progressively converted to calcite. The LHCF chimneys do not contain any sulfide or sulfate minerals or amorphous silica, which are common constituents of high-temperature black smoker deposits (Tab. 1).

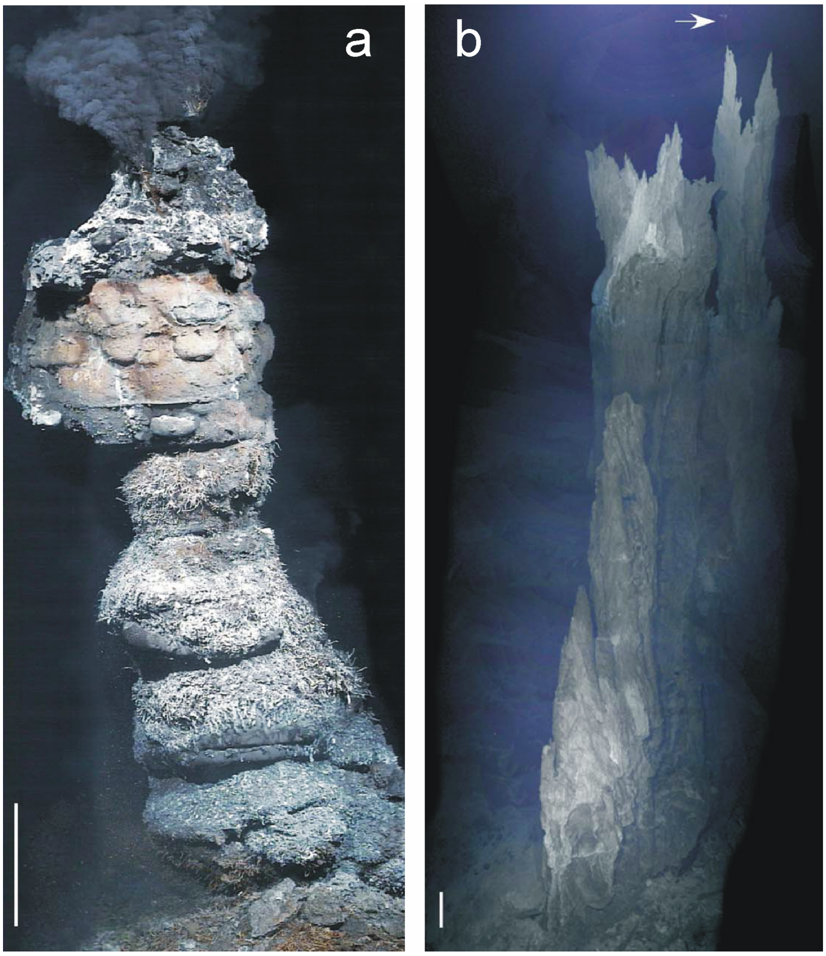

Fig. 31: Pictures of two different types of deep-sea hydrothermal vent systems. (A) Active black smoker edifice composed of metal sulfide with a height of 4 meters, located at the Endeavour Segment of the Juan de Fuca Ridge, Northeast Pacific Ocean. (B) Calcium carbonate venting chimney, found in the "Lost City" Hydrothermal Field (height: 30 m). Scale bars: 1 meter.[81]

Again, the mechanism of formation starts with the migration of seawater down into the subsurface along fractures and smaller cracks. During exothermic serpentinization reactions, the seeped water becomes warmed up to temperatures between 40-90°C in the course of hydration of the mineral olivine [$(Mg,Fe)_2SiO_4$] to serpentine [$Mg_3Si_2O_5(OH)_4$]. Thereby, Fe^{2+} in the olivine is oxidized to Fe^{3+} to form the iron oxide mineral magnetite (Fe_3O_4). As a side effect of the iron oxidation process, significant portions of hydrogen (H_2) are produced by reduction of water (18):

$$\underset{\text{olivine}}{6\,[(Mg_{1.5}Fe_{0.5})SiO_4]} + \underset{\text{seeped water}}{7\,H_2O} \longrightarrow \underset{\text{serpentine}}{3\,[Mg_3Si_2O_5(OH)_4]} + \underset{\text{magnetite}}{Fe_3O_4} + \underset{\text{hydrogen}}{H_2} \quad (18)$$

The resultant reducing conditions, coupled with Fischer-Tropsch type reactions (FTTS) that involve a catalytic activity of iron-nickel alloys, promote the conversion of fossile CO_2 (which is leached out from the mantle rock) to methane (CH_4) and other hydrocarbons (19):[81-87]

$$\underset{\text{(fossile)}}{CO_2\ (aq)} + \underset{\text{(from serpentinization)}}{[2 + (m/2n)]\,H_2} \xrightarrow[\text{Fe−Ni alloy}]{\text{FTTS}} (1/n)\,C_nH_m + 2\,H_2O \quad (19)$$

In addition, the resultant fluids are also enriched in Ca^{2+}, and are highly alkaline (pH 9-11),[88] while the concentrations of CO_2, metal ions and silica in the vent fluids are very low and H_2S is not present. After re-ascension of the modified vent fluid to the surface of the sea bed and upon mixing of the vent fluid with seawater, precipitation of calcium carbonate is driven by the reaction

$$\underset{\text{(from vent fluid)}}{Ca^{2+} + OH^-} + \underset{\text{(from sea water)}}{HCO_3^-} \longrightarrow CaCO_3\ (s) + H_2O \quad (20)$$

In this reaction, the OH^- and most of the Ca^{2+} are from the hot venting fluid, while the HCO_3^- stems from the cold seawater that mixes with the venting fluid.

5.3.3. Comparison of Both Hydrothermal Vent Systems and Their Relevance to Chemical Garden Systems in Laboratory

A comparison of the most relevant characteristics of both the “Black Smoker” and the “Lost City” systems is given in Tab. 1.

Despite of the chemical, compositional and geological diversities found for both hydrothermal vent systems, also fundamental similarities can be pointed out:

First, the overall underlying mechanism of vent formation in both systems requires the seepage or diffusion of sea water through cracks into the bedrock, where heating and dissolution processes between the penetrated water and the mantle rock lead to an enrichment of the seeped fluid with different ionic species and to a significant change in pH. After re-ascending to the ocean floor, the hot, enriched and modified vent fluid comes in contact with the cold and chemically different sea water, leading to precipitation reactions. As these processes take place over a period of thousands of years, large scale tubular chimneys are formed under constant conditions. However, in both vent systems, precipitation occurs due to the existence of permanent and significant differences in temperature, pH and ion concentrations between the ejecting venting fluids and the surrounding sea water reservoir, which are maintained by the precipitated tubular material until the top rim of the hydrothermal chimneys.

Due to these chemical gradients prevailing across a precipitated tubular structure and causing their further growth by continued precipitation, both deep-sea hydrothermal vent systems provide several striking similarities to the classical chemical garden laboratory systems, although formed within a drastically differing time scale.

	Black Smoker Systems	**Carbonate Systems**
Location	near and along active spreading centers, on young, hot basaltic crust	15 km away from the spreading center on 2 million years old and cooled crust
Heat Source	submarine volcanoes	exothermic fluid-mineral reactions (serpentinization process)
Host Rocks	volcanic rocks of basaltic nature	altered mantle rocks (serpentinites)
Venting Temperatures	typically >300°C, up to 407°C	typically 40-90°C
Fluid Compositions	acidic (pH 2-5); metal- and sulfide-rich, variable amounts of silica; no Mg, no sulfate	basic (pH 9-11); extremely poor in metals and silica, enriched in Ca, some sulfate
Volatile Compositions	enriched in CO_2 and H_2S; also contains H_2 and CH_4	enriched in H_2 (by serpentinization); enriched in CH_4 and other hydrocarbons (by FTTS)
Chimney Mineralogy	metal-rich structures: pyrite (FeS_2), chalcopyrite ($CuFeS_2$), sphalerite ($(Zn,Fe)S$); barite ($BaSO_4$), anhydrite ($CaSO_4$); amorphous silica	$CaCO_3$-dominated: mainly calcite, with aragonite as preliminary stage
Plumes	extensive, particle-laden plumes rising 200m in water column	minor plumes, <50m rise height, particle free

Tab. 1: Comparison of generalized characteristics of “Black Smoker” and “Lost City” hydrothermal vent systems.[81]

5.3.4. Hydrothermal Vent Systems as Possible Source for the Origin of Life

Enrichment of the venting fluids with methane and other hydrocarbons with longer chain lengths was detected in both types of deep-sea hydrothermal vent systems, originating from FTT reactions of H_2 (stemming from redox reactions of iron containing minerals and water) with CO_2 (from inorganic carbonate minerals) in the presence of different chromium-, iron- and nickel-bearing catalysts.[85-86] As these vent systems turned out to be the first discovered natural source of abiotically generated hydrocarbons, speculations have been offered that ancient versions of similar hydrothermal vents in the seas of a young earth might have been the origin of all terrestrial life.[71, 85, 89-91]

III. Experimental Part

1. Materials

For the preparation of silica garden tubes, the following metal salts were used as received without further purification (Tab. 2):

Metal salt	**Formula**	**Purity**	**Supplier**
iron(II) chloride tetrahydrate	$FeCl_2 \cdot 4H_2O$	>99%	Merck
iron(II) sulfate heptahydrate	$FeSO_4 \cdot 7H_2O$	>99%	Merck
iron(III) chloride hexahydrate	$FeCl_3 \cdot 6H_2O$	>99%	Merck
iron(III) nitrate nonahydrate	$Fe(NO_3)_3 \cdot 9H_2O$	>99%	Merck
iron(III) sulfate dodecahydrate	$Fe_2(SO_4)_3 \cdot 12H_2O$	>99%	Merck
cobalt(II) chloride hexahydrate	$CoCl_2 \cdot 6H_2O$	>99%	Merck
cobalt(II) iodide hydrate	$CoI_2 \cdot xH_2O$	98%	Alfa
cobalt(II) nitrate hexahydrate	$Co(NO_3)_2 \cdot 6H_2O$	>99%	Merck

Tab. 2: Specifications of metal salts used for the preparation of silicate gardens.

Commercial water glass (sodium silicate solution, Aldrich) served as silica source, which was diluted 1:4 by volume with water and subsequently used for silicate garden preparation. Specifications of the water glass are given in Tab. 3:

Sodium silicate solution	**w(SiO_2) [wt%]**	**w(NaOH) [wt%]**	**c(SiO_2) [mol L^{-1}]**	**c(NaOH) [mol L^{-1}]**
undiluted	27	14	6.2	4.8
diluted 1:4	6.75	3.5	1.55	1.20

Tab. 3: Specifications of undiluted and diluted sodium silicate solution.

AES single-element standard solutions for silicon (Fluka, 1001 mg L^{-1}), sodium (Fluka, 1000 mg L^{-1}), cobalt (Aldrich, 999 mg L^{-1}) and iron (Aldrich, 1000 mg L^{-1}) were diluted in ratios ranging from 1:20 to 1:1000 (v/v) with water and used for concentration calibrations. For iodine, freshly prepared solutions of potassium iodide (Merck, p.A.) served as reference during the AES experiments. Water was taken from a Millipore system.

2. Preparation of Silicate Gardens

2.1. Conventional Chemical Gardens with Random Shape

For a first test on the general suitability of different metal salts, conventional chemical gardens are synthesized by immersion of different metal salt crystal clusters ($NiSO_4 \cdot 6H_2O$, $CoCl_2 \cdot 6H_2O$, $FeCl_2 \cdot 6H_2O$, $Cu(NO_3)_2 \cdot 3H_2O$, $FeCl_3 \cdot 6H_2O$, $Co(NO_3)_2 \cdot 6H_2O$ and $CaCl_2 \cdot 2H_2O$) into 1200 mL of diluted sodium silicate solution (1:4 v/v; dimensions of the vessel: 16x9x10 cm^3).

2.2. Controlled Synthesis of Uniform Tubular Precipitates

For the preparation of macroscopic silica garden tubes with controlled shape, dry metal salt crystals ($CoCl_2 \cdot 6H_2O$, $FeCl_2 \cdot 4H_2O$, $FeCl_3 \cdot 6H_2O$) were ground to fine powder and pressed to tablets at 3.5 bar with a Perkin-Elmer hydraulic press, yielding specimens of defined and reproducible dimensions (type A: m = 0.5 g, d = 13 mm, h = 2 mm). Pellets were then fixed at the bottom of a 120 mL plastic beaker with the aid of a small piece of double-sided adhesive tape. Subsequently, 10 mL of diluted water glass (1:4 v/v) were carefully added at the rim into the beaker with a rate of ~1 mL per second using a plastic syringe onto which a long needle (0.80x120 mm, Braun) was mounted. As soon as the formation of a silicate membrane over the metal salt was observed and the pellet started to dissolve markedly, further 30 mL of diluted sodium silicate solution were added with a constant rate of 1-10 mL per minute via a dosing apparatus (Unita I, Braun). The speed of addition required to obtain hollow tubes with desired diameters depended heavily on the kind of the metal salt, and was adjusted correspondingly. After completion of water glass addition, vertical tubes with a length of about 20 mm and inner diameters of 5-8 mm had grown exhibiting an open end on top (see Fig. 39 in section IV.1). As chloride proved to be not detectable with the used AES device, silica gardens were also prepared using $CoI_2 \cdot H_2O$ as alternative metal salt with a counter-ion suitable for AES analysis. However, due to the strong hygroscopicity of cobalt iodide, tablets had to be prepared in a glove box under nitrogen atmosphere. To that end, a small hand press was employed which gave pellets with slightly different dimensions (type B: m = 0.3 g, d = 5mm, h = 8mm).

It is worth to mention that once an open tube had formed and addition of sodium silicate was stopped, macroscopic growth was essentially terminated. However, continued influx of water occasionally leads to an overflow of the interior solution at the top of the tube. This causes further precipitation of membrane material which proliferates along the air-liquid interface. Repeated analyses yet proved that these precipitation processes did not have a noticeable influence on the progressions of concentrations and pH neither in the interior nor the exterior solution.

2.3. Isolation of Tubular Precipitates for *ex-situ* Examinations

To facilitate the isolation of individual tubes for subsequent *ex-situ* examinations, above mentioned spreading of overflowing solution on the air-liquid interface was prevented by removal of very small volumes of the interior liquid shortly before overflowing would have occurred. As a consequence, very stable and uniform tubes were obtained after growth was abandoned by careful suction of the surrounding water glass. Subsequently, eventually remaining solution in the tube interior was removed with a small syringe equipped with a thin needle. Finally, tubes were thoroughly and repeatedly rinsed with pure water to remove remnants of dissolved sodium silicate and metal salt solution, respectively. For faster drying and to avoid possible dissolution by elongated exposure to pure water, isolated tubes were rinsed with ethanol and dried at ambient temperature in a protective N_2 atmosphere.

3. Characterization

Different *ex-situ* and *in-situ* characterization techniques were applied to obtain information about the structural and elemental composition and the evolution of important parameters in the course of silicate garden formation.

The following *ex-situ* characterization techniques were used for silicate garden analysis:

- Scanning electron microscopy (SEM)
- Energy dispersive X-ray spectroscopy (EDX)
- X-ray powder diffraction analysis (Powder XRD)

In-situ characterizations were performed using the techniques listed below:

- Atomic emission spectroscopy (AES)

- X-Ray absorption spectroscopy (XAS)
- pH measurements
- Measurement of electrochemical potentials
- Time-resolved X-ray diffraction measurements (XRD)

To ensure reliability of the data, most analyses described in the following sections were in general conducted on three independently prepared silica gardens for each type of metal salt, unless otherwise stated. Results showed in principle good reproducibility within a given set of experiments, and individual values were therefore averaged.

3.1. Scanning Electron Microscopy (SEM) and Energy Dispersive X-Ray Spectroscopy (EDX)

Fragments of silicate garden tubes based on $CoCl_2 \cdot 6H_2O$, $FeCl_2 \cdot 4H_2O$ and $FeCl_3 \cdot 6H_2O$ which were prepared and isolated according to the procedures described in sections III.2.1 and III.2.3 were carefully transferred onto alumina SEM holders.

As prepared samples were analyzed on their elemental composition by EDX spectroscopy, using an EDAX Genesis 2000 system attached to a FEI Quanta 400F scanning electron microscope (SEM) operating at a working voltage of 20 kV.

After sputter-coating with a thin Au layer, samples were analyzed on their structural appearance on a Zeiss Leo Gemini 1530 SEM working at acceleration voltages between 2-5 kV at working distances ranging from 3-10 mm.

3.2. Atomic Emission Spectroscopy (AES)

Atomic emission spectroscopy (AES) was used to trace the temporal evolution of the concentrations of the distinct ions present in the interior and exterior solutions (Co^{2+}, $Fe^{2+/3+}$, Na^+, $H_3SiO_4^-$, I^-).

Therefore, silicate garden tubes were prepared according to the routine described in section III.2.1. Upon completion of water glass addition, liquid samples were taken after different times from the interior (10 μL) and exterior (100 μL) solutions of the as-prepared tubes and subsequently diluted with 10 mL water. Sampling of only such small volumes was chosen due to the limited total volume of solution enclosed by the membrane walls (around 0.2-0.5 mL), so as to enable repeated extractions over longer periods of time and to avoid considerable perturbation of the system by removal of a significant fraction of its overall volume.

As-obtained diluted samples were analyzed by AES on a Spectroflame-EOP ICP-AES instrument (Spectro Analytical Instruments GmbH, Kleve, Germany). As the used apparatus did not allow for the detection of chlorine, a set of experiments was also performed on silicate gardens prepared from CoI_2, therefore containing iodide as traceable type of anion.

Prior to the analysis of the samples, concentration calibrations were done by measuring elemental standard solutions (Fluka, Aldrich) diluted with water in ratios ranging from 1:20 to 1:1000 (v/v). The thus generated concentrations of the standards varied within an interval of 0-1.5 mM for cobalt and iron, 0-2.0 mM for sodium and silicon, and 0-5 mM for iodide, and by this fully covering the found range of concentrations for the different species in silica gardens. Resulting calibration curves all exhibited satisfactorily linear behavior with correlation coefficients greater than 0.998. Samples withdrawn from silica gardens were analyzed under conditions identical to those used for the standards.

3.3. X-ray Absorption Spectroscopy (XAS)

For the determination of cobalt and iron ion concentrations, prevailing in the interior of the silicate garden tubes, XAS measurements were performed at the material science beamline I811 of the synchrotron radiation facility MaxLab II in Lund, Sweden.

Silicate garden tubes with open ends on top were generated by the procedure described in section III.2.1, using pellets of $FeCl_3 \cdot 6H_2O$, $FeCl_2 \cdot 4H_2O$ and $CoCl_2 \cdot 6H_2O$, respectively. Repeated extraction of small, undiluted aliquots (10 µL per sample) was carried out after different times by dipping ultra-thin rectangular precision capillaries (VitroCom, inner dimensions: 0.1x2.0x50 mm, wall thickness: 100 µm, borosilicate glass) into the interior solutions of the as-prepared silica garden tubes. Subsequently, filled capillaries were fixed onto a holder and centered relative to the incident X-ray beam (1 mm diameter).

The particular concentration of Co^{2+}or $Fe^{2+/3+}$ present in the analyzed sample was determined by comparison of the edge jump height at the Fe_K and Co_K edge, respectively, which increases linearly with increasing metal ion concentrations (see Fig. 32).

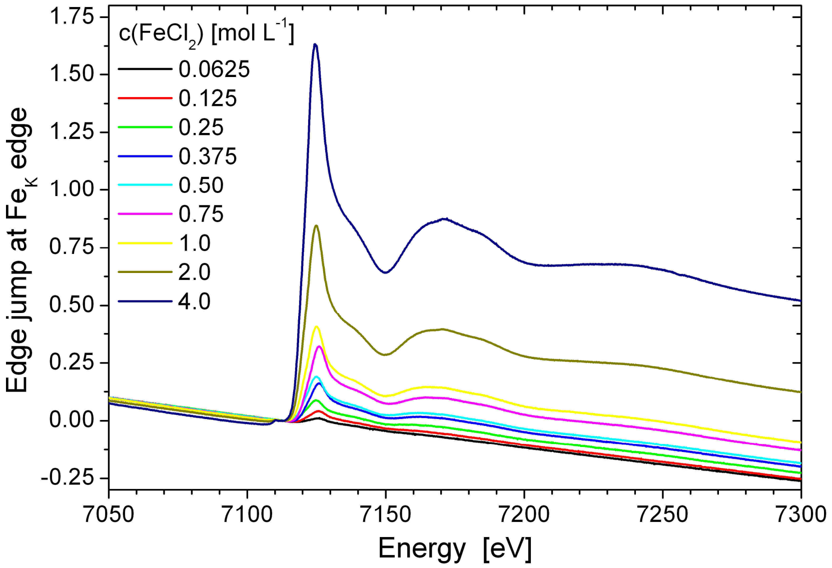

Fig. 32: Height of edge jump at the Fe_K edge for aqueous solutions of $FeCl_2$, depending on the concentration of Fe^{2+}

The actual samples were measured using an extended routine in step-scan mode (-100 to +200 eV relative to edge jump, varying step width between 1-6 eV, 1 s integration time per step, t_a = 600 s). All XAS measurements were done under ambient conditions in transmission mode.

Prior to sample analysis, calibration of edge jump values to metal ion concentrations was achieved by measuring a series of solutions with known concentrations in the range of 0-4 M for all investigated metal salts, using a fast scanning routine (QXAS mode, -100 eV to +370 eV relative to the absorption edge, total acquisition time t_a = 150 s). Gathered data yielded a straight calibration line with good correlation (Fig. 33).

Iron and cobalt metal foils served for energy calibration, giving absorption energies of 7110.75 eV and 7708.78 eV for the Fe_K and Co_K edge, respectively.

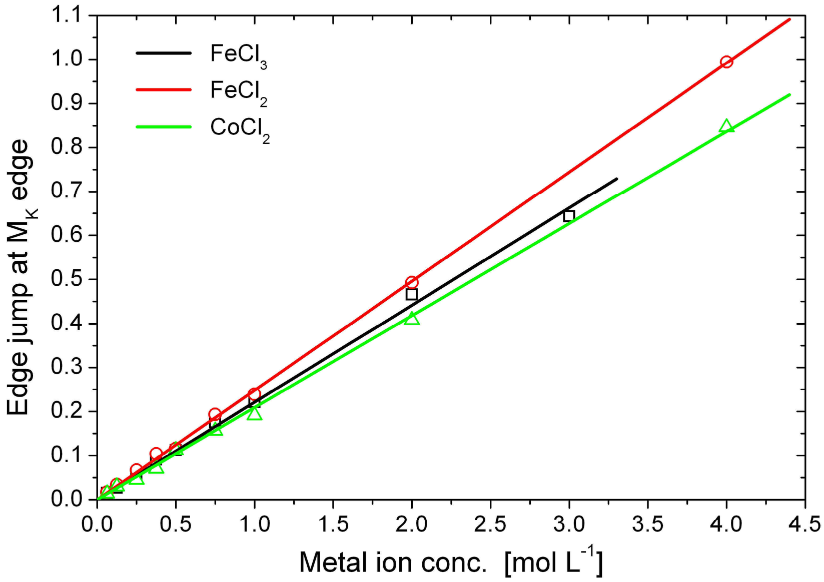

Fig. 33: Linear correlation between the height of the edge jump and metal ion concentrations for the three used metal salts $FeCl_3$ (black), $FeCl_2$ (red) and $CoCl_2$ (green).

3.4. Long-term pH Measurements

Continuous measurements of the pH of the interior solution enclosed by the precipitated membrane were performed to obtain important information about the progression of possible hydroxide ion diffusion across the tubular membrane.

Therefore, open-tube grown silicate gardens were prepared following the procedure described in section III.2.1. Subsequently, a glass micro-electrode was immersed into the interior solutions of the as-prepared silica garden tubes (submersion depth >5 mm). The pH electrode (tip diameter: 3 mm, Mettler Toledo InLab Micro) was used on a digital laboratory pH meter (Schott, model CG 843), which was connected to a PC. pH values were automatically acquired in intervals of 5 s with the aid of a custom-designed software.

The pH of the exterior water glass solution was found to be not subject to noticeable changes with time and was thus only measured at the beginning and end of each experiment.

3.5. Measurement of Electrochemical Potential Differences

For the time-resolved detection of electrochemical potential differences - generated by significant gradients in pH and ion concentrations across the precipitated membrane wall - silicate garden tubes were also prepared as explained in section III.2.1.

Afterwards, a set of identical platinum or Ag/AgCl stick electrodes was immersed into both (the exterior and interior) reservoirs. Electrodes were linked to a multimeter (Metex M-3890D USB) which allowed for data acquisition by a connected PC in constant intervals of 1-5 s. A photograph showing the experimental setup used for the combined measurement of potential differences with a set of Pt (left) and Ag/AgCl (right) electrodes in two simultaneously grown silicate garden tubes is given in Fig. 34.

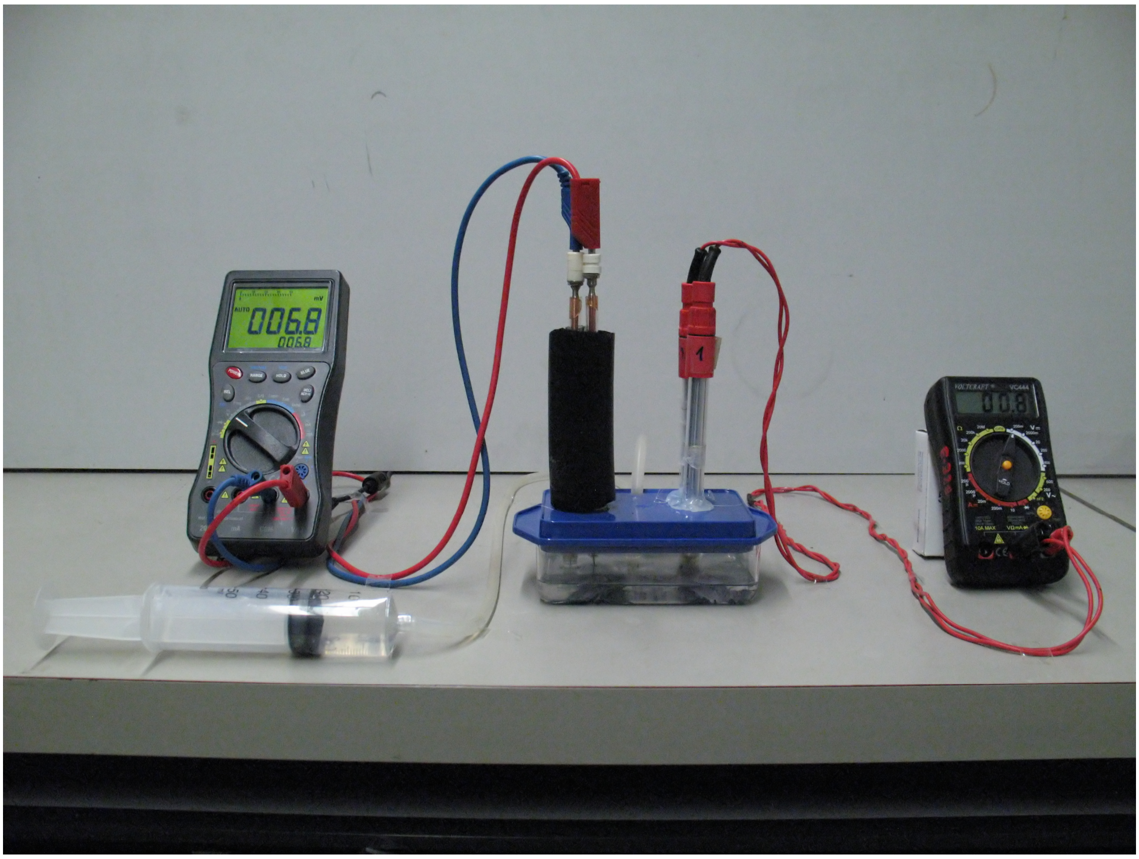

Fig. 34: Experimental setup for the simultaneous measurement of potential differences with two sets of Pt (left) and Ag/AgCl (right) electrodes immersed into two silicate garden tubes grown under identical conditions.

3.6. *Ex-situ* X-Ray Powder Diffraction Analysis

Silicate garden tubes were analyzed *ex-situ* on their crystalline fractions by X-ray powder diffraction techniques. Therefore, tubular precipitates were grown for 24 h and subsequently isolated by removing the surrounding water glass solution, followed by thorough rinsing with water and ethanol. Samples were dried at 60°C over night and finally ground to fine powder. Powder diffraction measurements were performed on a Siemens D5000 diffractometer, operating at a wavelength of 1.54 Å (Cu Kα radiation). The measured 2 Theta range was chosen from 8-80° in steps ranging from 0.02-0.04°. Integration time per step was set to 15 s. Assignment and identification of detected reflexes to crystalline matter was realized by using the reference library of the STOE WinXPOW software package.

3.7. Time-resolved X-Ray Diffraction Measurements (XRD)

Two different sets of experiments were performed at the synchrotron radiation sources *Elettra* (Trieste, Italy) and *Doris III* (HASYLAB, DESY, Hamburg, Germany) for the time-resolved examination of crystallization processes, occurring during the growth of tubular silicate garden precipitates. However, due to different measuring conditions found at the two beamlines F3 (*Doris III*) and XRD1 (*Elettra*), the experimental setup had to be adjusted properly.

3.7.1. XRD Measurements at the XRD1 Beamline (*Elettra*)

For the examination of crystallization processes in silicate gardens, XRD measurements were performed at the *Elettra* beam line XRD1 using a monochromatic X-ray beam ($E = 12.4$ keV, $\lambda = 1.00$ Å), which was obtained by filtering an incoming white X-ray beam (energy range: 4-21 keV) through an optics system, including a double-crystal Si(111) monochromator set.[92] However, as the overall X-ray beam intensity was not high enough to allow the use of thick samples, only very thin samples could be measured to avoid a total absorption of the X-rays by glass, water and other sample components. Therefore, the preparation procedure for silicate gardens growth described in section III.2.1 could not be applied, as tube diameters of 6-8 mm require a minimum sample thickness of at least 1 cm. Instead, miniaturized silicate gardens were grown by placing tiny seed crystals of $FeCl_3 \cdot 6H_2O$, $FeCl_2 \cdot 4H_2O$ or $CoCl_2 \cdot 6H_2O$ at the bottom of thin glass capillary tubes (Mark tubes, length: 85 mm, diameter: 2 mm, wall thickness:

10 μm, glass: no. 50, Hilgenberg) and subsequent addition of small amounts of diluted water glass with a 1 mL syringe equipped with a thin needle (0.8 x 120 mm, Braun). Glass capillaries were fixed onto a specially designed sample holder which was mounted on the magnetic plate of the goniometer head (see Fig. 35c). XRD measurements were started directly after silicate addition with a delay of ~2-3 min, contributed to the time necessary for activating the security buttons and for closing the beamline hutch. XRD measurements were performed at positions near the bottom of the capillary directly above the seed crystal to obtain a maximum intensity of diffraction patterns. In all experiments, 2D diffractograms were recorded with a CCD detector (MarResearch, image diameter: 165 mm), positioned at a crystal to detector distance of 60 mm, giving a final 2 Theta range from 0-106.2° when normalized to $Cu_{K\alpha1}$ (1.54 Å). Beam size was 0.2 x 0.3 mm² for all measurements. Acquisition times varied from 5-80 s, depending on the respective beam intensity which was determined by the actual current of the storage ring. Measurements were repeatedly performed in periods ranging from 3 min at the beginning of silicate garden formation to several hours at later growth times. The experimental setup used at beamline XRD1 is given in Fig. 35.

Data were collected by the use of specially tailored software running on Linux PC workstations. .tiff image files of the 2D diffraction patterns from the CCD detector were generated from the acquired raw data (.mccd files) by a converter (marView). Fit2D was used for extraction of 2 Theta (at λ=1.00 Å) and intensity values from the raw files. In a next step, 2 Theta values were transformed from λ_1=1.00 Å to λ_2=1.54 Å. Subsequently, recorded intensity values of each measurement were normalized to acquisition time and ring current, followed by background subtraction, reflex integration and data smoothing, performed with a specially tailored, LabView derived software (Integrator 3.0, ©by Roger-Jan Kutta). Finally obtained data sets were partially fitted with TableCurve 2D.

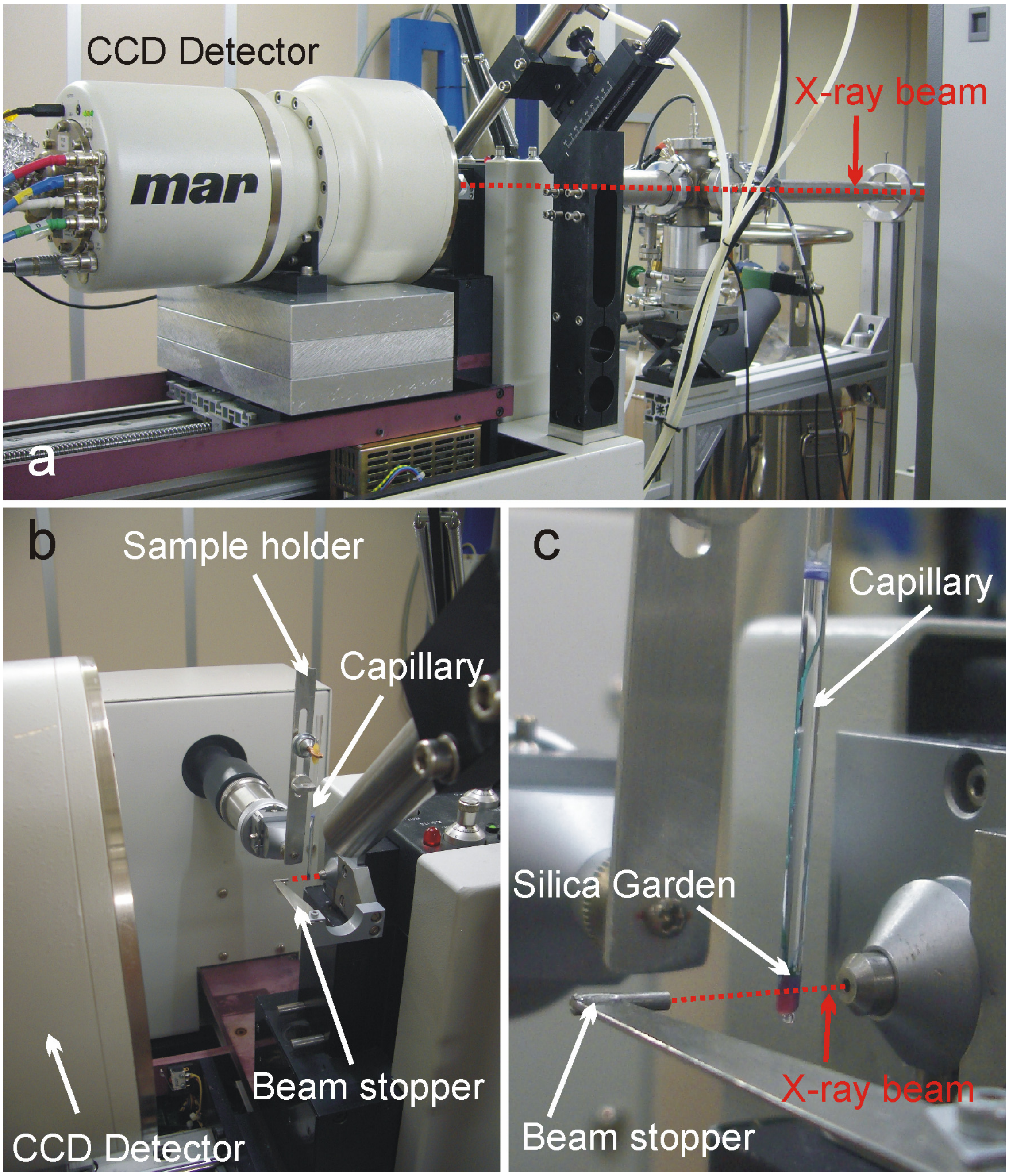

Fig. 35: Photographs of the experimental setup at beamline XRD1. (a) Total view showing incoming X-ray beam and CCD detector; (b) close view on the space between sample and detector; (c) zoom-in showing a glass capillary mounted in the center of the X-ray beam and containing a miniaturized silicate garden prepared from a $CoCl_2$ crystal.

3.7.2. Experiments on the EDXRD Beamline F3 (*HASYLAB, DESY*)

In contrast to the diffraction experiments performed at *Elettra*, beamline F3 of the *Doris III* storage ring provides the performance of energy-dispersive X-ray diffraction experiments with a white X-ray beam (energy range: 6-52 keV). Therefore, thick samples could be analyzed on their crystallinity without causing the problem of total radiation absorption.

The intensity of the incoming white beam was adjusted by a first slit system (S1, Fig. 36 and Fig. 37), using a beam area of 300 x 300 μm^2. Scattered radiation was detected on a Ge detector (2048 energy selective channels, cooled with liquid nitrogen), positioned at a horizontal angle of Theta = 7° from the incident X-ray beam (Fig. 37). A second slit system (S2, Fig. 36) mounted on the detector arm was adjusted in the range of 100 x 100 μm^2 to 200 x 200 μm^2 for the improvement of resolution.

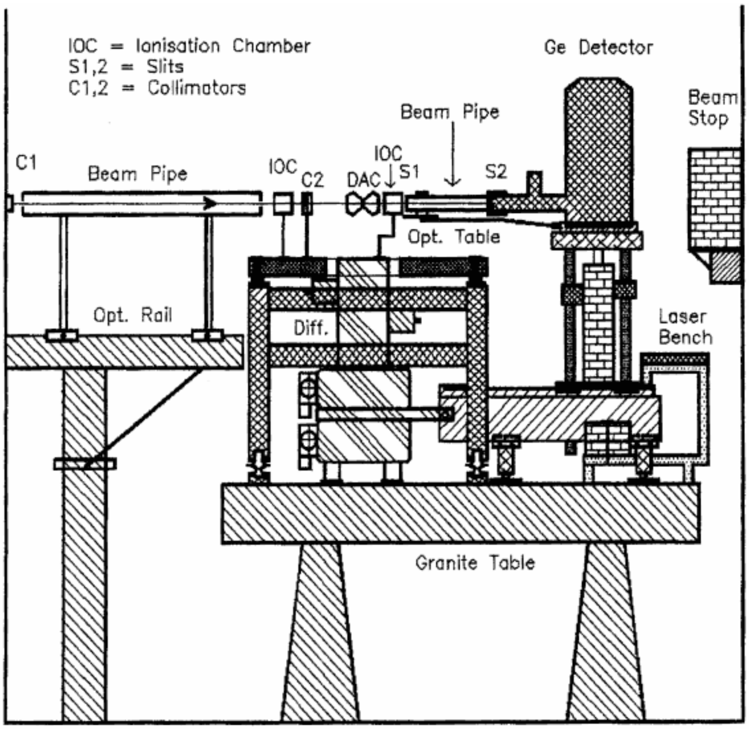

Fig. 36: Schematical depiction of the base setup installed at beamline F3.[93]

Silicate garden samples with tubular structures were prepared in Duran glass tubes (dimensions: 12 x 100 mm, Duran Group) from small pellets of metal salts (listed in Tab. 2) by slow addition of diluted water glass. Subsequently, the as-prepared samples were inserted into a specially designed sample holder (cf. Fig. 37), equipped with two beam windows with sufficient diameter to prevent absorption of scattered radiation by the glass walls of the sample holder. The sample holder was mounted on a magnet stirrer at a certain position, so that the center of the Duran glass tube was exactly at the intersection point where the incident beam hits the virtually prolonged detector arm.

A PC coupled to a multi-channel analyzer was used for data collection and storage in the energy-dispersive experiments, allowing the performance of automated EDXRD measuring runs, with acquisition times of 300 s per run.

As the detectable energy range depended on the used detector angle, a calibration of the detector channels (2048) to the energies of scattered radiation was carried out prior to measurements on silicate gardens, using the fluorescence peaks of a mixture of different metal powders.

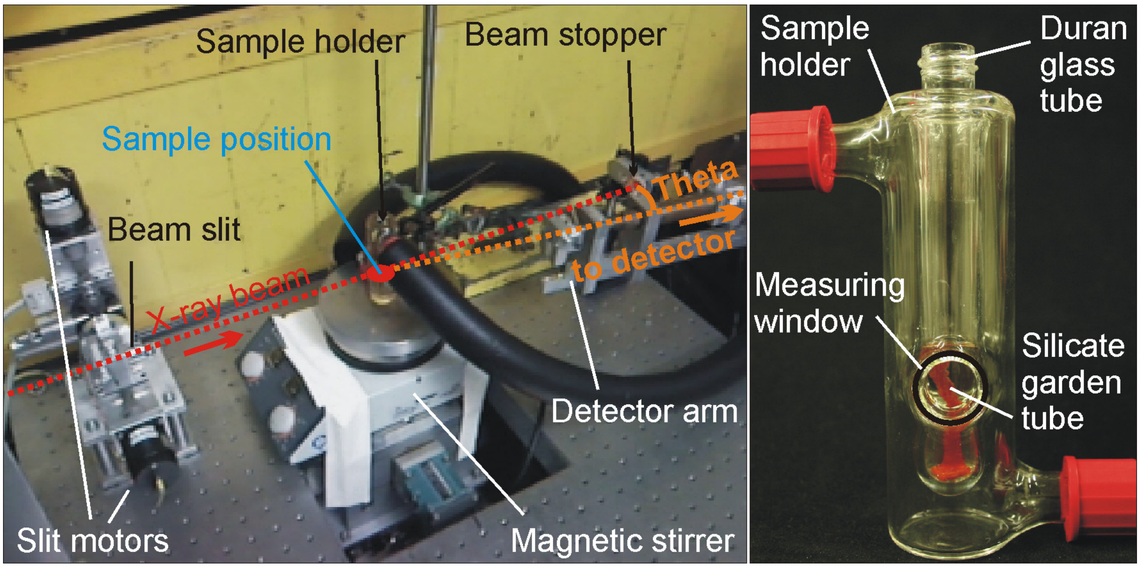

Fig. 37: Experimental setup at beamline F3 used for EDXRD measurements on silicate gardens with open-tube growth.

IV. Results and Discussion

1. Macroscopic Growth Behavior

1.1. Conventional Silica Gardens from Crystal Clusters

Conventional chemical gardens were prepared according to the procedure described in section III.2.1. A series of images is depicted in Fig. 38, showing the typical progression of common chemical garden growth after different periods up to 4 hours growth time.

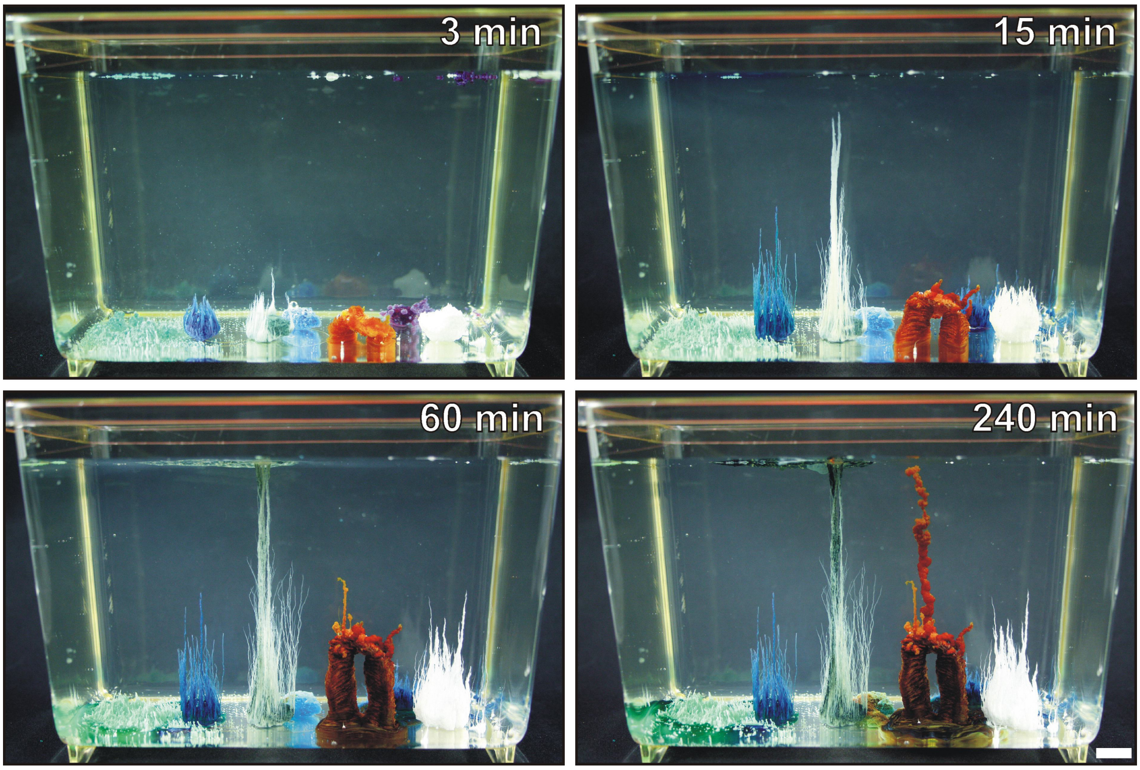

Fig. 38: Series of Images showing the growth of chemical gardens from crystal clusters upon immersion into diluted sodium silicate solution after different times; used metal salts (from left to right): $NiSO_4 \cdot 6\ H_2O$ (cyan), $CoCl_2 \cdot 6\ H_2O$ (blue), $FeCl_2 \cdot 6\ H_2O$ (green), $Cu(NO_3)_2 \cdot 3\ H_2O$ (blue), $FeCl_3 \cdot 6\ H_2O$ (orange), $Co(NO_3)_2 \cdot 6\ H_2O$ (blue), $CaCl_2 \cdot 2\ H_2O$ (white); scale bar is 1 cm.

In summa, conventional growth of silicate gardens proceeds as follows: After crystal clusters are added to the diluted water glass, formation of a colorless silicate membrane layer occurs, followed by the growth of vertical filaments with dimensions of up to

10 cm in length and 2 mm in diameter within a period of approximately 4 h. Resulting precipitates exhibit a seaweed-like shape. At growth times larger than ~4 h, no significant changes in size or shape of the precipitated chemical garden structures can be observed. Besides upwards directed growth of filaments, also horizontal spreading of the precipitated membrane is observed, leading to a proliferation of flat and crusty layers on the bottom of the reaction vessel. From Fig. 38 it is also clearly visible that the growth rates as well as the final dimensions of the vertical filaments differ noticeably. While use of $NiSO_4 \cdot 6\,H_2O$ (cyan, left) and $Cu(NO_3)_2 \cdot 3\,H_2O$ (blue, center) provokes only weak growth of small and tiny filaments, $CoCl_2 \cdot 6\,H_2O$ (blue, 2nd from left), $FeCl_2 \cdot 6\,H_2O$ (green, 3rd from left), $FeCl_3 \cdot 6\,H_2O$ (orange, 3rd from right), $Co(NO_3)_2 \cdot 6\,H_2O$ (blue, 2nd from right) and $CaCl_2 \cdot 2\,H_2O$ (white, right) produce significantly more filaments with larger dimensions.

1.2. Chemical Gardens with Controlled Tubular Shape

Precondition for performing reproducible experiments on silicate gardens is the establishment of an experimental procedure allowing for the preparation of fairly standardized silica gardens with similar shape and size. This was achieved by using pressed tablets of powdered metal salts instead of irregular seed crystals, and by considerably slowing down the addition of water glass solution to the metal salt (cf. section III.2.2). In that way, silica gardens consisting of vertical hollow tubes with ends open to the atmosphere and diameters in the range of several millimeters were obtained (Fig. 39a, b). The relatively large dimensions of the as-synthesized tubular structures enabled facile access to the interior solution and the direct immersion of a microelectrode for continuous pH measurements (Fig. 39c).

The rate of tube formation strongly depends on the kind of metal salt used and is by far fastest in the case of $FeCl_3$. A possible explanation for this finding might be related to the existence of distinct osmotic pressures in the three silica garden systems studied. The osmotic pressure Π of a salt solution in assumption of ideality is defined as

$$\Pi = \mathrm{i} \cdot \mathrm{c} \cdot \mathrm{R} \cdot \mathrm{T} \tag{21}$$

with i being the number of generated ions in case of complete dissociation. Consequently, Π should be proportionally higher in silica gardens based on $FeCl_3$ ($i = 4$) than in those prepared with $CoCl_2$ and $FeCl_2$ ($i = 3$). As a result, the overall rate of exchange of species is propelled by reinforced pumping of exterior solution through the membrane. This effect is visible to the naked eye, as vigorous ascension of freshly created interior $FeCl_3$ solution increases the possible speed of water glass dosing, whereas less intense inflow of water into $CoCl_2$- and $FeCl_2$-based tubes necessitates a significantly slower addition.

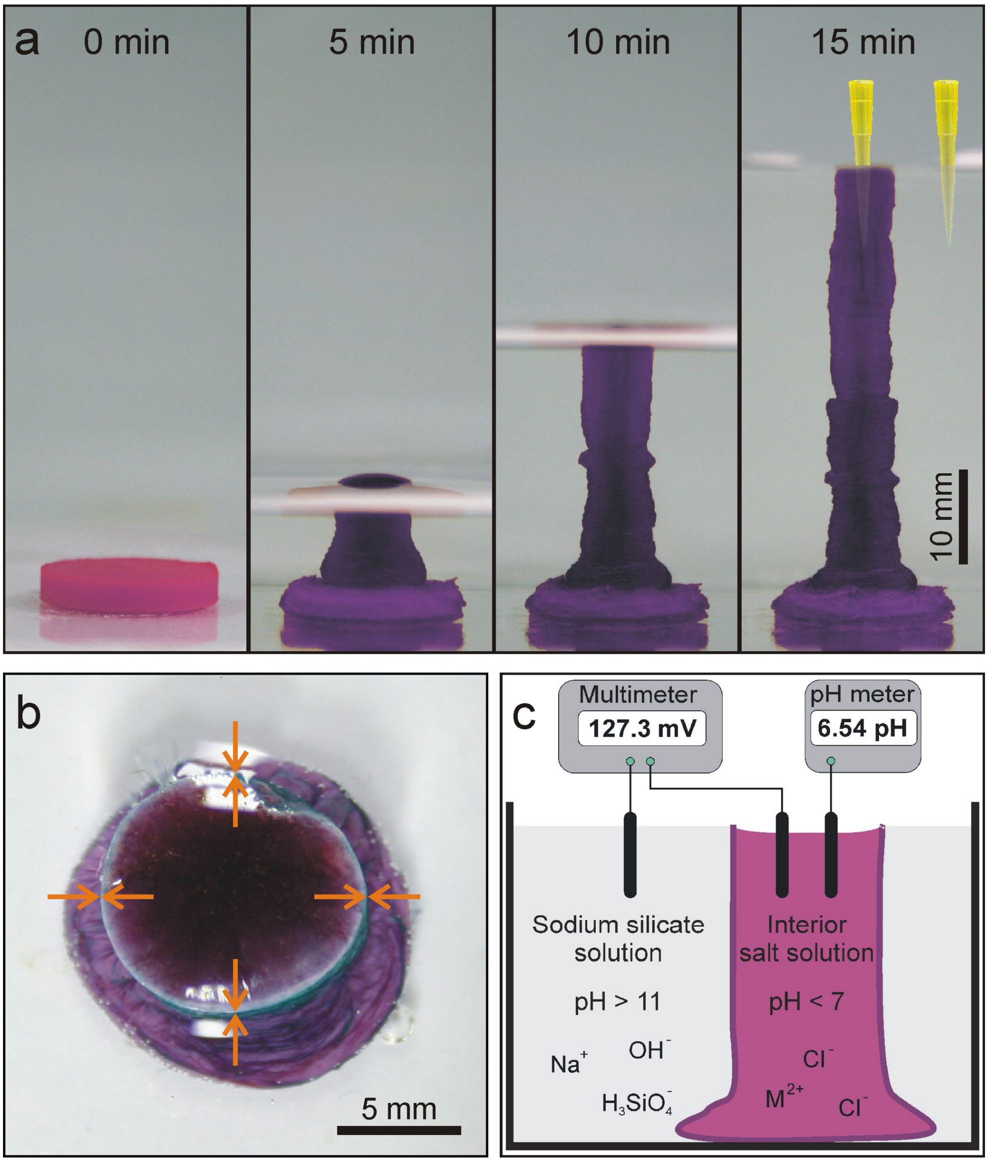

Fig. 39: a) Sequence of images illustrating the formation of a tubular membrane with defined dimensions upon addition of dilute water glass to a tablet of $CoCl_2$. Pipette tips indicate the sampling of the solutions inside and outside the membrane performed for analyzing ion concentrations. b) Top view of the as-prepared tube, showing the open end of the membrane. c) Scheme of the experimental setup used for pH and ΔE_h measurements.

2. *Ex-situ* Characterization of Silicate Garden Tubes

Tubular precipitates based on $CoCl_2$, $FeCl_2$ and $FeCl_3$ were prepared and isolated according to the procedures described in the sections III.2 and IV.1. Subsequently, fragments of the tubes were analyzed by scanning electron microscopy on their structural appearance. EDX spectroscopy was performed at selected positions of the SEM samples to collect information about the qualitative and quantitative elemental composition of the tubes.

2.1. Analysis of $CoCl_2$-based Silicate Garden Tubes

SEM pictures taken from the cross-section of a tubular $CoCl_2$ based precipitate at two different magnifications are given in Fig. 40. From both micrographs it is clearly recognizable that the membrane is constituted of three significantly different layers, as it was also denoted in several previous studies.[17, 29] While a clear differentiation can be made between the first, outer layer (upper right part) and a second intermediate layer, the transition between the intermediate layer and the interior surface (lower left part) proceeds gradually and cannot be clearly separated. Macroscopic porosity of the tube membrane increases from the exterior to the interior surface at first in a distinct step between the outer and the intermediate layer, and subsequently in a continuous way until a rod-shaped structure at the interior surface.

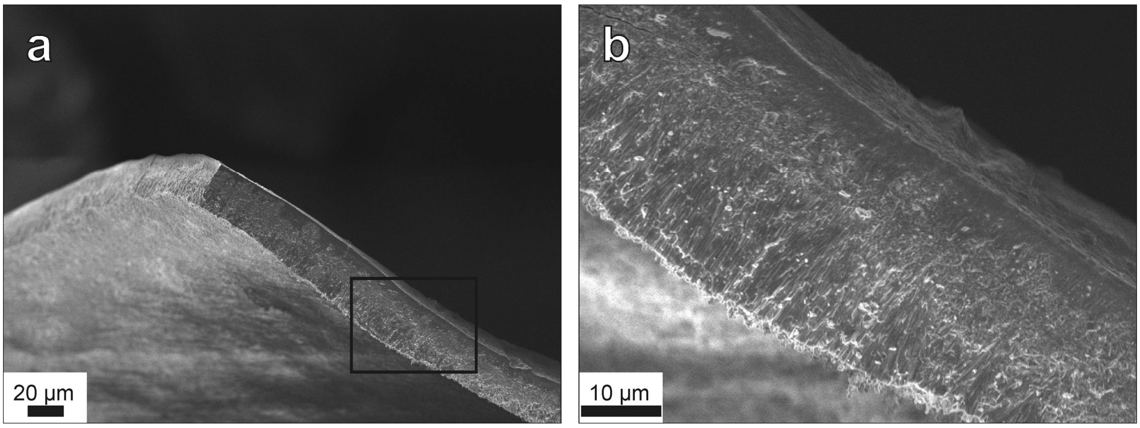

Fig. 40: Series of SEM pictures showing the cross-section of a tubular precipitate prepared from a $CoCl_2$ pellet at different magnifications.

A top view onto the exterior surface reveals a periodically shaped but smooth and compact outer skin (Fig. 41). While the visible cracks originate from the drying process, periodical waviness was generated during the growth of the membrane tube; although sodium silicate solution was added continuously to the vessel containing the metal salt pellet, growth of the tube membrane was observed to proceed in many tiny discontinuous steps due to repeated swelling of the meniscus (caused by ongoing osmotic inflow of water through the membrane) and subsequent overflowing of the interior solution.

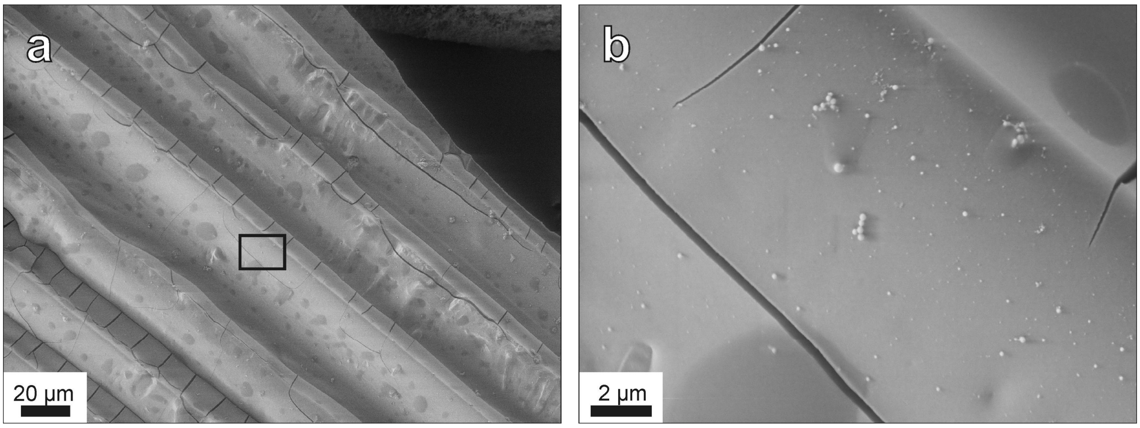

Fig. 41: Series of SEM pictures of the exterior surface of a tubular precipitate prepared from a $CoCl_2$ pellet.

In contrast to the exterior surface, SEM micrographs, taken from the interior surface, show at a first glance a rougher surface and the absence of periodical structures (Fig. 42a, b). This discrepancy indicates that the exterior surface represents an initial layer which is formed prior to the tube's interior surface. A zoom-in further reveals the existence of small crystallites, which are bedded onto an interwoven network of fibers (Fig. 42c, d).

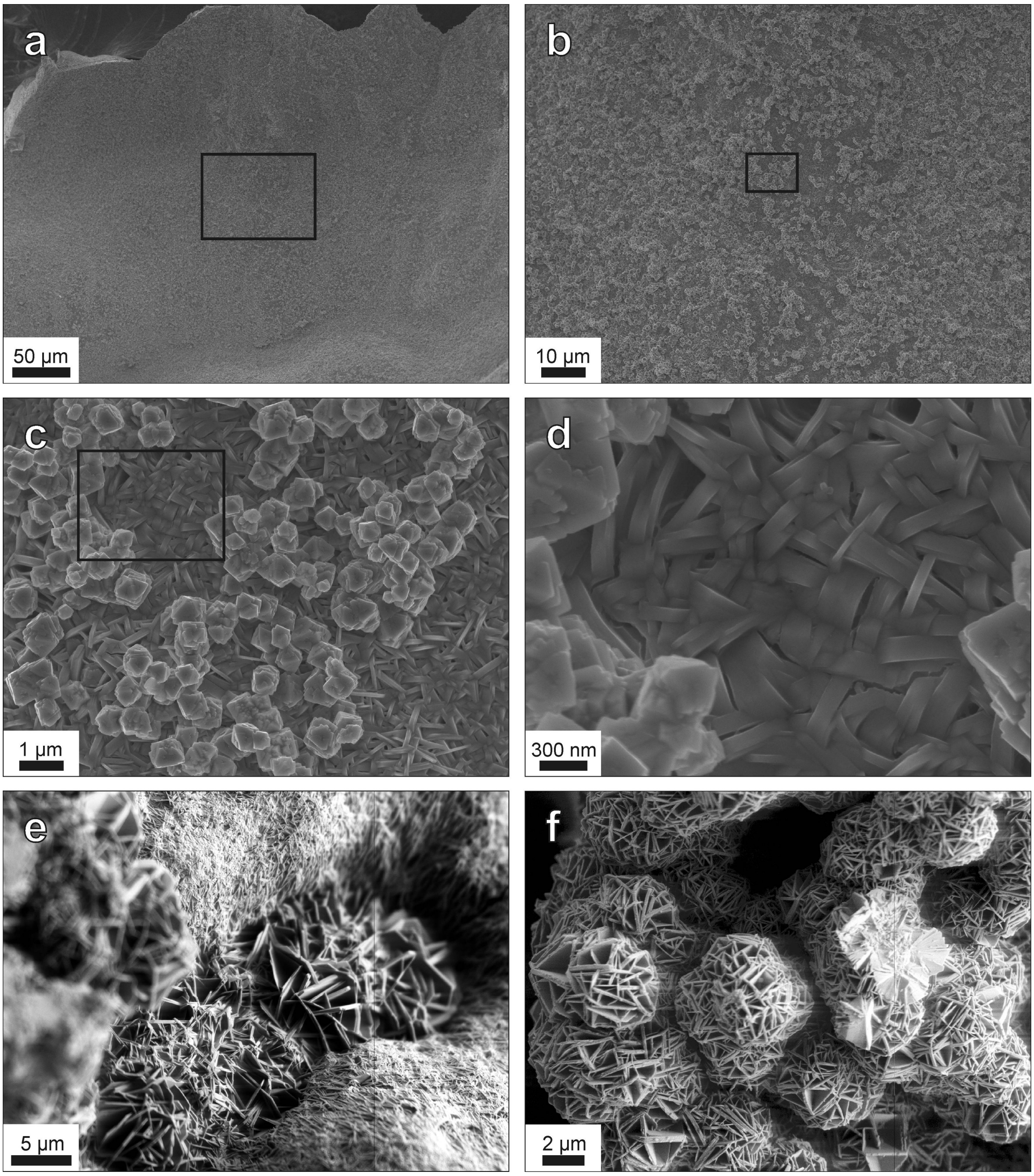

Fig. 42: SEM pictures taken from the interior surface of a tubular precipitate prepared from a $CoCl_2$ pellet. (a-d) Zoom-series showing the presence of crystallites and interwoven filaments in coexistence with (e, f) isolated or intergrown baryte rose-like buds.

Another stunning structuring was also observed at the inner surface, consisting of isolated and inter-grown, rugged globules (Fig. 42e, f), reminiscent to the mineralogical phenomenon of desert rose growth (cf. Fig. 43). Rosettes of crystals composed of cobalt oxide-hydroxide with identical structure were also reported by different authors in the course of silicate garden growth and deposition of $LiCoO_2$ films from solution, respectively.[27, 61, 94]

Fig. 43: Photograph of isolated and intergrown baryte rose buds.[95]

These drastic discrepancies in the structuring of the both, exterior and interior, surfaces of the membrane wall clearly indicates that the elemental composition of both layers must be considerably different. For this reason, qualitative (Fig. 44) and quantitative (Tab. 4) EDX spectroscopy measurements were performed at positions similar to those depicted in Fig. 42.

	(a) exterior		**(b) crystalline interior**		**(c) fibrous interior**	
Element	**Wt%**	**At%**	**Wt%**	**At%**	**Wt%**	**At%**
(C)	(14.2)	(26.5)	(5.5)	(14.2)	(5.1)	(13.3)
O	33.4	46.8	21.7	42.1	23.4	45.4
Si	8.7	7.0	0.8	0.9	0.9	1.0
Na	4.1	4.0	2.3	3.1	---	---
Cl	2.2	1.4	8.2	7.2	8.3	7.3
Co	37.4	14.2	61.5	32.5	62.3	33.0

Tab. 4: Quantitative EDX analysis on $CoCl_2$ tubes derived from spectra presented in Fig. 44

In all three EDX spectra the whole set of elements (Na, Si, O, Co, Cl) was detected which are present in the silicate garden system, although membrane tubes were thoroughly rinsed with water and ethanol before analysis. However, EDX spectra and quantitative analysis also verify the expected differences in the chemical composition of both surfaces, pointing out that the outer membrane layer is significantly enriched in silica, while the tube interior exclusively consists of cobalt, oxygen and chloride. It is further worth to notice that in the tube interior, despite of their clearly different nature, the elemental composition of both, crystalline (Fig. 44b) and fibrous matter (Fig. 44c), does not significantly differ from each other. This might be a hint that crystalline material could originate from transformation of amorphous preliminary stages in the course of silicate garden growth.

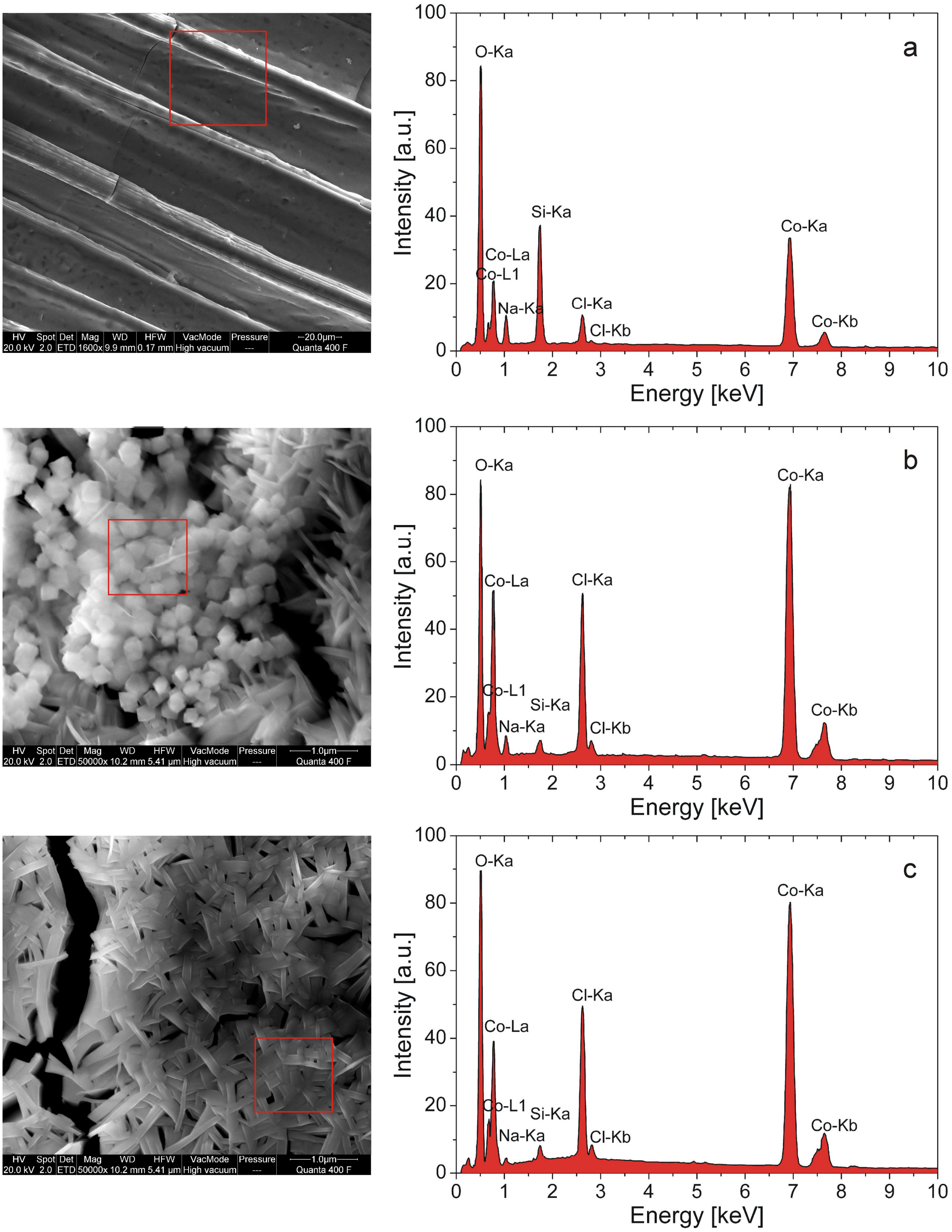

Fig. 44: EDX spectra of (a) exterior and (b-c) interior surface of a tubular membrane prepared from a $CoCl_2$ pellet in sodium silicate solution.

From quantitative analysis, a rough estimation about the composition of the outer and inner surface can be drawn, giving "2 $Co(OH)_2 \cdot SiO_2$" and "2 $Co(OH)_2 \cdot Co_2(OH)_3Cl$" as possible constitution for the outer and inner surface, respectively.

X-ray powder diffraction measurements were performed on powdered samples obtained according to the routine described in section III.3.6. A resulting powder diffractogram of a $CoCl_2$ based silicate garden tube is given in Fig. 45. Comparison with data from the STOE WinXPOW reference library allowed the identification of three different crystalline substances present in the chemical garden powder. The mayor fraction (red lines) could be identified as $Co_2(OH)_3Cl$, coexisting with smaller fractions of $Co(OH)_2$, present as α- and β-phase (blue and green lines). The overall composition therefore roughly correlates with the elemental composition determined by EDX analysis (cf. Tab. 4).

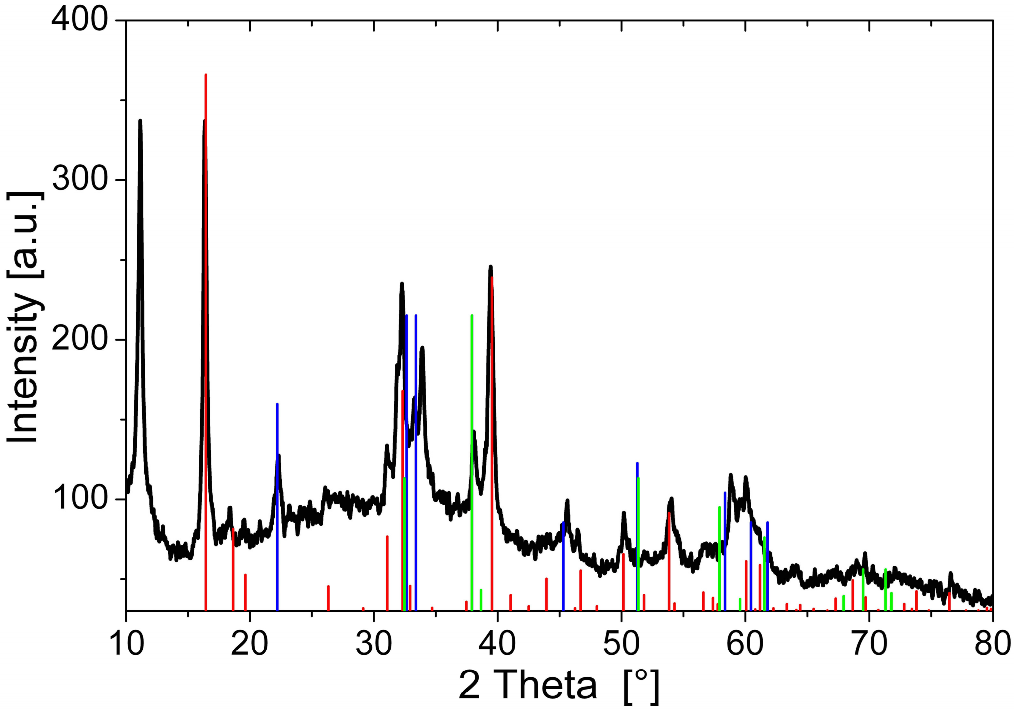

Fig. 45: Powder diffractogram of a silicate garden tube prepared from $CoCl_2$ showing the existence of three different crystalline fractions; red: $Co_2(OH)_3Cl$, blue: $Co(OH)_2$ (α-phase), green: $Co(OH)_2$ (β-phase).

2.2. Analysis of $FeCl_2$-based Silicate Garden Tubes

Exterior and interior surfaces of open-tube grown silicate garden precipitates prepared with $FeCl_2$ were also analyzed on their structure and chemical composition. A zoom-series of SEM micrographs taken from the exterior surface of a tube membrane is given in Fig. 46. Similar to the $CoCl_2$ based membrane, a network of large cracks spreads along the entire surface, caused by drying effects. However, a closer view on the membrane exterior unburdens the existence of randomly dispersed, small agglomerated spherical particles which are loosely spread on an even and uniformly structured, porous surface.

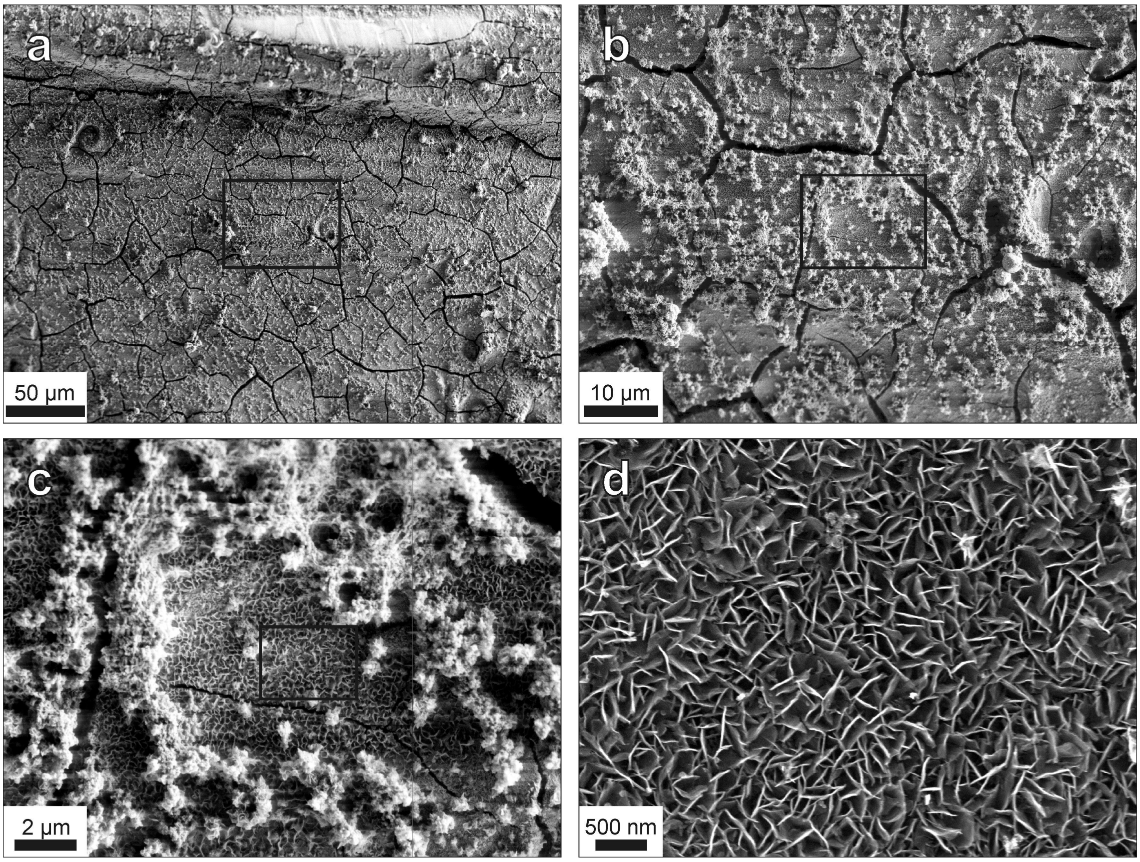

Fig. 46: Zoom-series of SEM pictures taken from the exterior surface of a tubular precipitate prepared from a $FeCl_2$ pellet.

In comparison, a detailed examination of the tube interior, presented in Fig. 47, only shows the presence of isolated, thin cracks. Areas of even structuring (Fig. 47a) coexist with domains consisting of intergrown and isolated spheres (Fig. 47b-f). A porous and regular structure, very similar to the appearance of the outer side of the membrane tube, can be found over a widespread surface area (Fig. 47a-d). However, besides the described uniform porosity, a second type of spherical particles can be found (Fig. 47e, f), exhibiting a more compact shape. Angular sites indicate on the presence of crystalline matter.

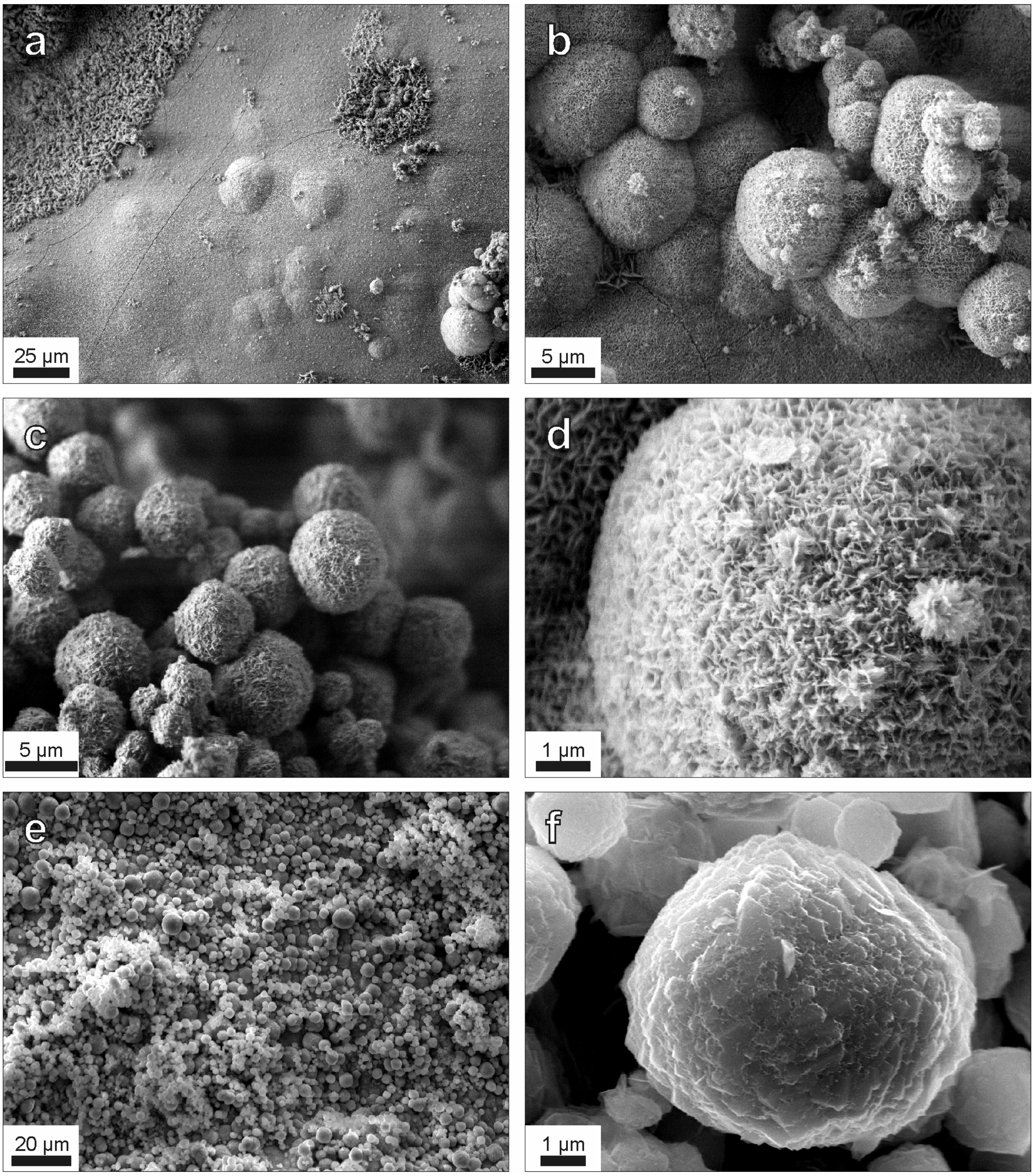

Fig. 47: SEM pictures of the interior surface of a tubular precipitate prepared from a $FeCl_2$ pellet.

According to the consistency of the porous structuring found on both sides of the precipitated membrane, similar chemical compositions might be expectable.

Indeed, a comparison of qualitative (Fig. 48) and quantitative (Tab. 5) EDX analyses of typical structures found on both sides of the precipitate clearly evidence that the chemistry is quite similar and both surfaces are exclusively composed of Fe, Cl and O. This is in contrast to the layering observed for silicate gardens based on $CoCl_2$, where distinct differences in the chemical composition can be stated for both membrane sides (cf. Fig. 44).

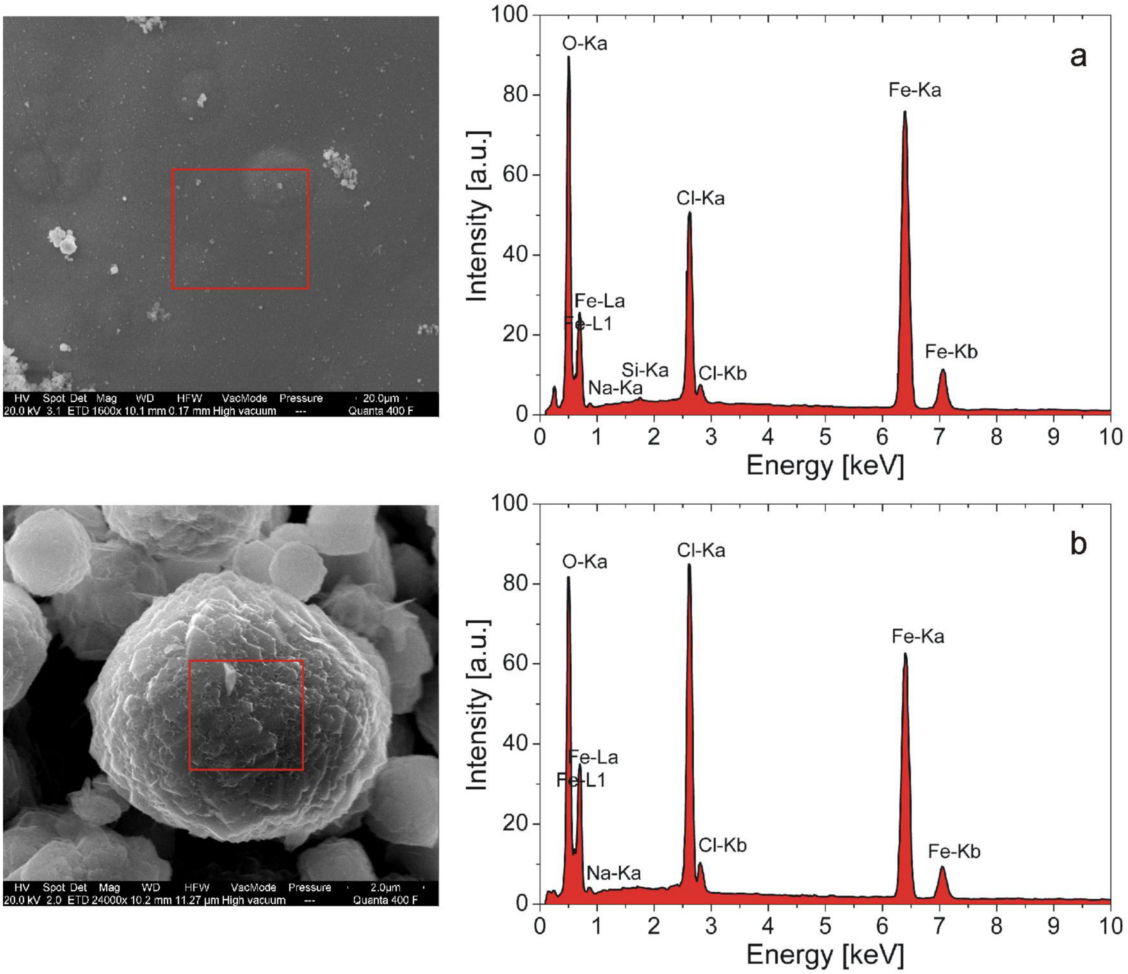

Fig. 48: EDX spectra of (a) exterior and (b) interior surface of a tubular membrane prepared from a $FeCl_2$ pellet in sodium silicate solution.

Again, the possible composition of the outer and inner surface can be estimated from the quantitative EDX analyses, giving "$Fe_2(OH)_3Cl$" and "2 $Fe(OH)_2{\cdot}Fe_2(OH)_3Cl$" as possible constitution for the inner and outer surface, respectively (cf. Tab. 5). Thus, the existence of an external skin containing considerable amounts of metal silicate is not observed for $FeCl_2$ based tubular precipitates. However, the loosely bound particle agglomerates found on the exterior surface (cf. Fig. 46b, c) probably represent the remains of a silica skin which was generated prior to the precipitation of the iron hydroxide/iron hydroxide chloride precipitate at the very beginning of membrane formation. This hypothesis can be affirmed by observations which are visible to the naked eye during the growth of open-tube silicate garden membranes prepared from $FeCl_2$ pellets; as soon as dissolved iron(II) chloride solution from the interior comes in contact with the surrounding sodium silicate solution, a colourless, geleous precipitate is formed which subsequently more and more turns green. As the green colour stems from "green rust" (Fe(II)/Fe(III)hydroxides), this is clear evidence that the hydroxide is formed after initial precipitation of a silica-rich gel-layer. With proceeding growth, the membrane not only becomes more green in colour but also gains in rigidity, which further indicates that precipitation of solid iron hydroxides is favoured in comparison to metal silicate precipitation. Possibly by weak interactions between the initial exterior silica gel layer and the iron hydroxide/chloride precipitated at the membrane interior, most of the silica is simply washed away during the isolation and cleaning procedure when growth was abandoned. It is also possible that the initially precipitated silica, which is formed due to a drop in pH upon contacting with the slightly acidic iron(II) chloride solution, re-dissolves at later growth times when all acidic Fe^{2+} is removed by hydroxide precipitation.

	(a) flat exterior		**(b) globular interior**	
Element	**Wt%**	**At%**	**Wt%**	**At%**
(C)	(9.2)	(21.0)	---	---
O	26.5	45.1	28.8	55.1
Si	---	---	---	---
Na	---	---	---	---
Cl	9.2	7.0	18.4	15.9
Fe	55.1	27.0	52.8	29.0

Tab. 5: Quantitative EDX analysis on $FeCl_2$ based silicate garden tubes derived from spectra presented in Fig. 48.

Again, powder diffraction techniques were applied for the detection of crystalline fractions in the silicate garden system, following the routine described in section III.3.6. The powder diffractogram of a tubular precipitate prepared from $FeCl_2$ is depicted in Fig. 49, together with the reflex positions (vertical coloured lines) of assigned reference substances taken from the STOE WinXPOW library. Three different crystalline substances are obviously present in the powder of $FeCl_2$ derived silicate garden precipitates: Crystalline FeO(OH), which mainly consists of Goethite (red lines) together with a smaller fraction of Akaganeite-M (green lines), coexists with Fe_3O_4 (Magnetite; blue lines), indicating that most of the incorporated Fe(II) has been oxidized to Fe(III) within the course of drying and grinding. This observation is in contrast to the composition of the crystalline structures found during EDX Analysis (cf. Fig. 48 and Tab. 5). Obviously, the highly enlarged surface (caused by grinding) together with elevation of the temperature to 60°C during the drying process significantly changes the composition of the precipitated material.

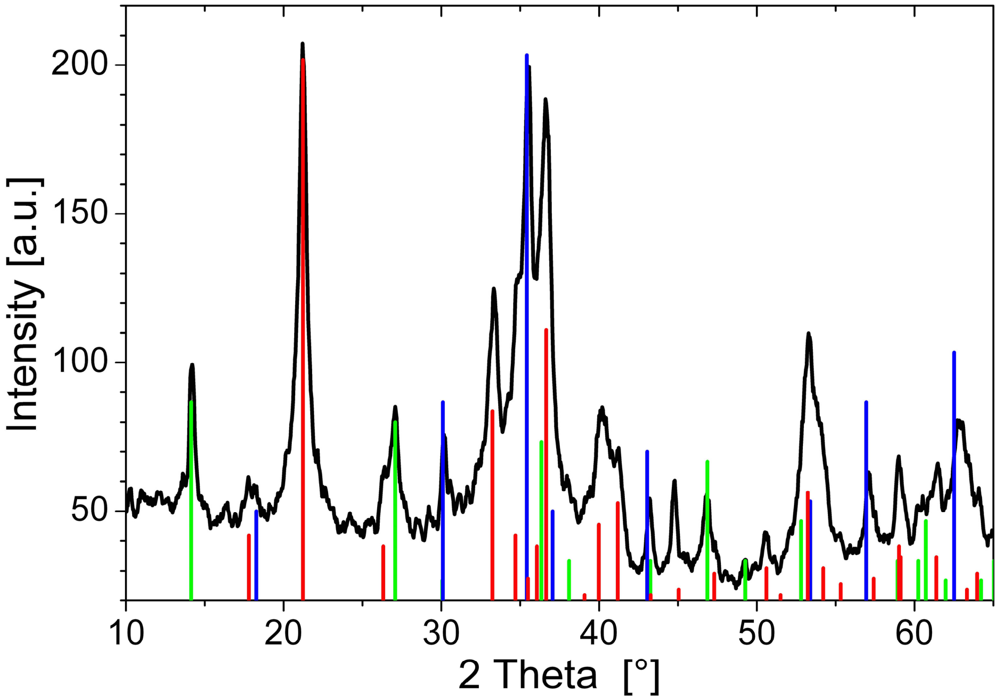

Fig. 49: Powder diffractogram of a silicate garden tube prepared from $FeCl_2$ showing the existence of three different crystalline fractions; red: FeO(OH) (Goethite), green: FeO(OH) (Akaganeite-M), blue: Fe_3O_4 (Magnetite).

2.3. Analysis of $FeCl_3$-based Silicate Garden Tubes

In contrast to the open-top tubes prepared with $CoCl_2$ and $FeCl_2$, which were isolated after a period of 24 h, growth of silicate gardens prepared with $FeCl_3$ was abandoned already after a period of 3 h to prevent complete solidification of the interior solution, which usually proceeds within a period of 3-7 hours after tubes were formed.

A zoom-series of SEM pictures of the membrane exterior of such a $FeCl_3$-based tube is presented in Fig. 50. Both micrographs reveal a dense and relatively smooth outer skin which does not feature any remarkable structuring. The slight waviness visible in Fig. 50a can again be ascribed to the stepwise precipitation during tube formation, as observed for $CoCl_2$ based tubes. A visible network of cracks was not found.

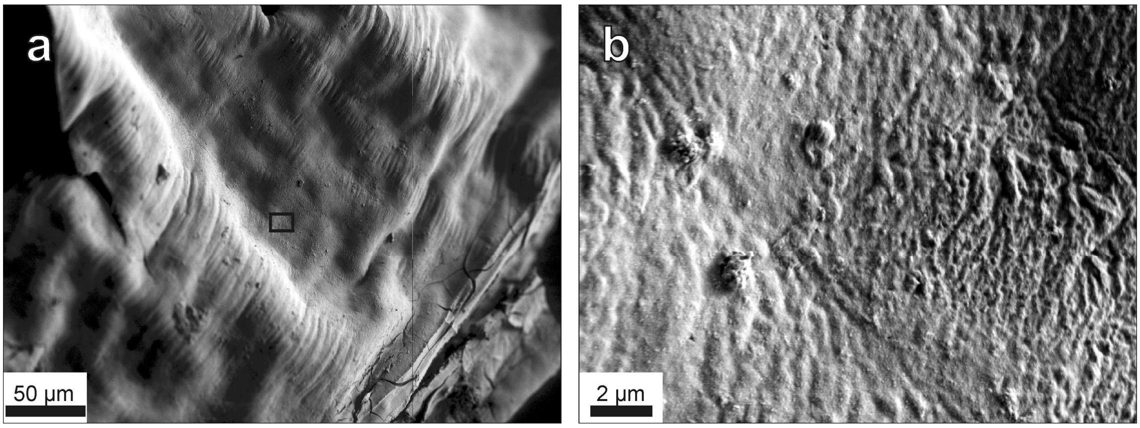

Fig. 50: SEM pictures of the exterior surface of a tubular precipitate prepared from a $FeCl_3$ pellet.

In contrast to the smoothness of the tube exterior, the inner membrane exhibits a wrinkled and ribbon-like structuring, reminiscent of parallel oriented wood fibers. However, all ribbons show multiple cracks, which can be assigned to drying effects as well as to breakage caused by exertion of pressure on the membrane during sample preparation. Reason for this fibrous structure can again be found in the oscillatory growth of the silicate garden tubes. Apart from these two phenomena, no characteristic sub-structuring can be stated as it is found for the other two presented silicate garden types, so that the precipitated matter is quite compacted.

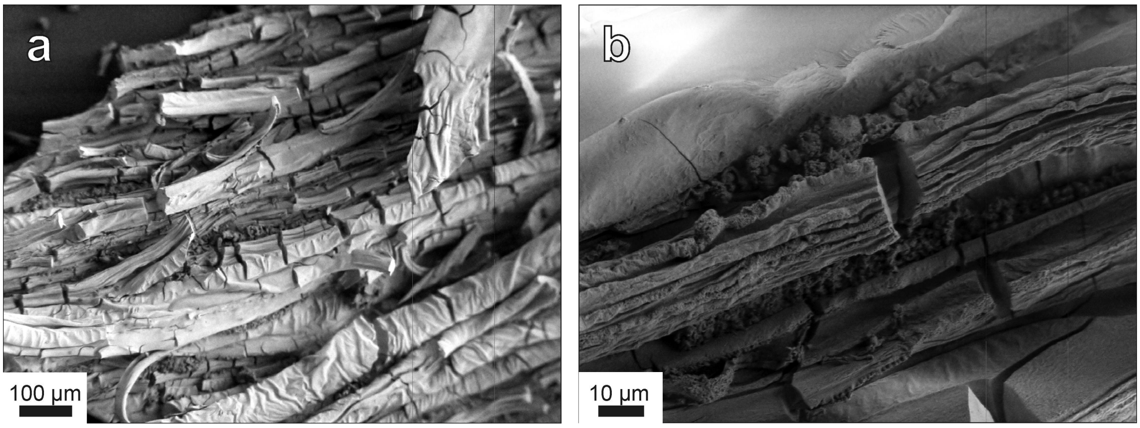

Fig. 51: SEM pictures showing the interior surface of a tubular precipitate prepared from a $FeCl_3$ pellet.

Despite of the compactness found on both sides of the tube wall, qualitative (Fig. 52) and quantitative (Tab. 6) EDX analyses point out significant differences in the chemical composition of the membrane wall.

	(a) exterior		**(b) interior**	
Element	**Wt%**	**At%**	**Wt%**	**At%**
(C)	(10.3)	(15.9)	(10.1)	(21.6)
O	48.0	56.0	30.6	48.9
Si	39.4	26.2	2.7	2.5
Na	2.3	1.9	1.2	1.3
Cl	---	---	1.4	1
Fe	---	---	54.0	24.7

Tab. 6: Quantitative EDX analysis on $FeCl_3$ based silicate garden tubes derived from spectra presented in Fig. 52.

While the smooth outside exclusively consists of Si and O (with traces of Na), the interior surface is mainly composed of Fe and O (with low fractions of Si, Na and Cl). Therefore, the outer membrane surface can be regarded as a pure SiO_2 layer, while the tube interior is predominantly composed of iron(III) hydroxide/oxide, FeOOH.

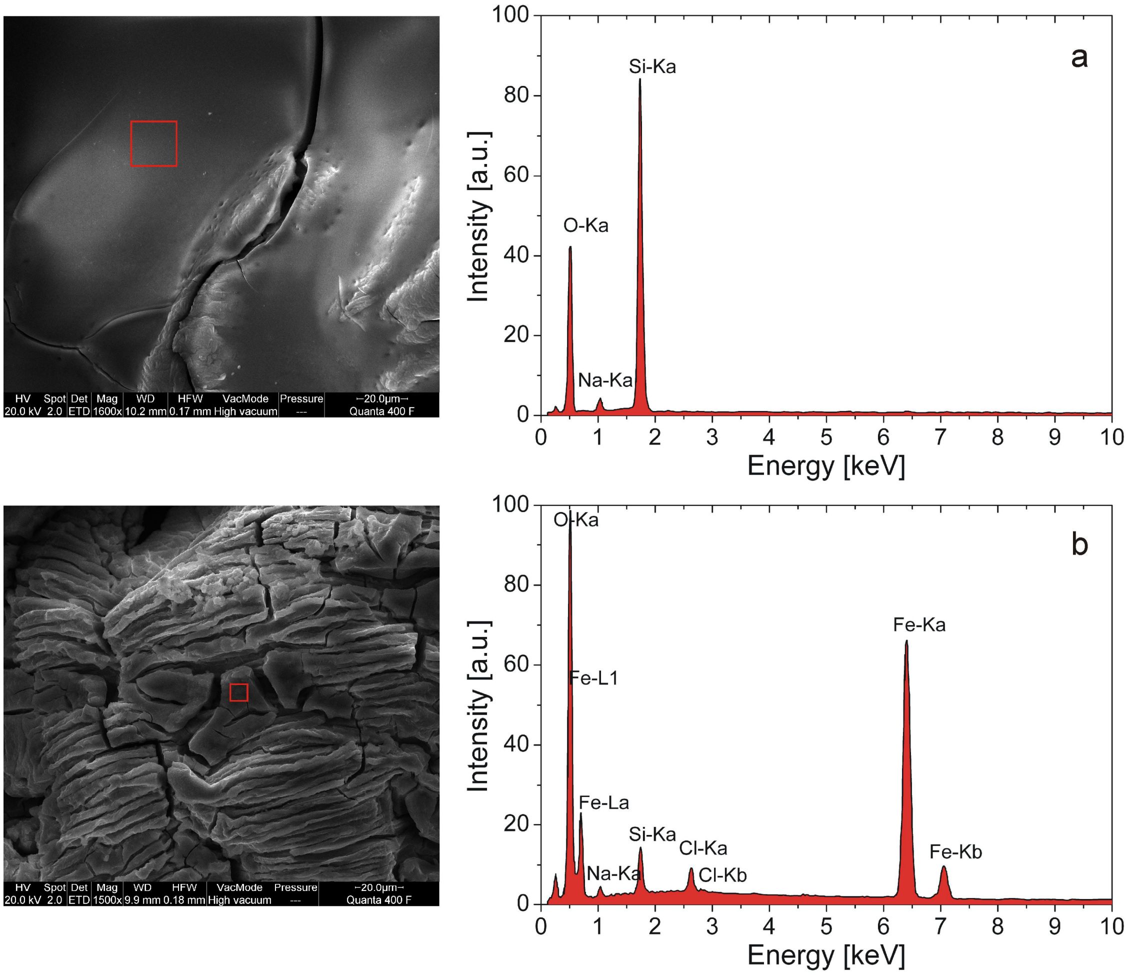

Fig. 52: EDX spectra of (a) exterior and (b) interior surface of a tubular membrane prepared from a $FeCl_3$ pellet in sodium silicate solution.

Ex-situ X-ray diffraction was also performed on powdered samples originating from $FeCl_3$ based tubular precipitates obtained according to the procedure described in section III.3.6. The resulting powder diffractogram is presented in Fig. 53. By using the STOE software package, all existing reflexes of the diffractogram could be assigned to a binary crystalline mixture, mainly consisting of Halite (NaCl, red lines) and traces of Akaganeite-M (FeO(OH), blue lines). The presence of NaCl crystals can be explained by the fact that the slightly soluble sodium chloride was not quantitatively removed from the bulky material which gelified inside the tubular precipitate at growth periods longer than 3-5 hours (see section IV.3.2 for more details). Drying of the whole tubular aggregate then leads to a higher concentration of NaCl in the remaining solid and thus to a significant amount of crystalline sodium chloride. The discrepancy between the amounts in NaCl found in the powder diffractogram and the lacking of sodium and chloride in the EDX analysis (Tab. 6 and Fig. 52) can be explained by the different growth time after which the grown tubules were isolated; while commencing solidification of the tube interior was prevented by abandoning silicate garden growth after 3 h for EDX and SEM analyses, the $FeCl_3$ based silicate garden tube was allowed to evolve for 24 h before samples were isolated for X-ray powder diffraction. Therefore, the tube interior became completely solidified and entrapped sodium and chloride ions could not quantitatively be washed out during the cleaning process.

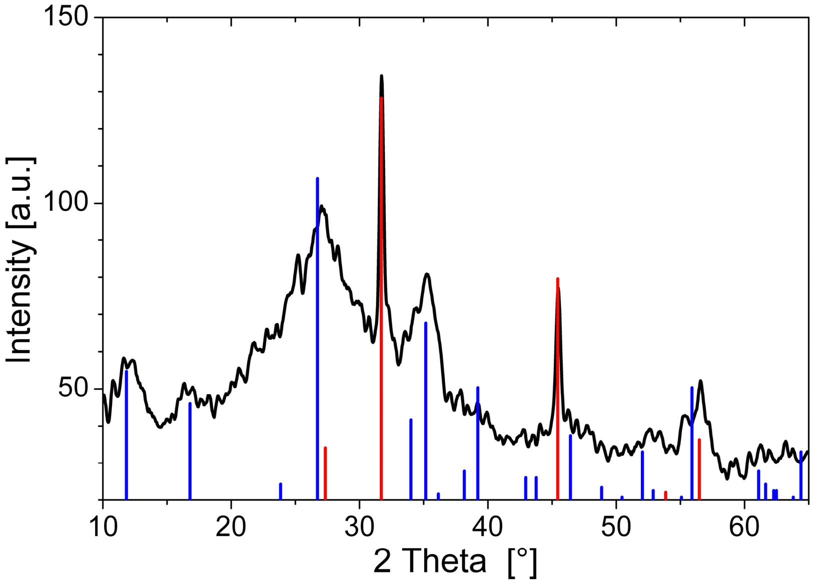

Fig. 53: Powder diffractogram of a silicate garden tube prepared from $FeCl_3$ showing the existence of crystalline fractions; red: NaCl, blue: FeO(OH) (Akaganeite-M).

3. Spatiotemporal Distribution of Ionic Species

Temporal changes in the concentration of the distinct ion species present in the system were traced by AES measurements according to the experimental procedure described in section III.3.2; after preparation of the tubular membranes was finished, samples were taken from the metal salt solutions enclosed by the tube walls as well as from the silica reservoir surrounding them over extended periods of time (8-70 hours) in intervals ranging from 2 min to 5 hours. Subsequently, each of the samples was analyzed by AES spectroscopy with respect to its content of sodium, silicon and iron/cobalt. Typically resulting profiles for the interior solution are shown in Fig. 54.

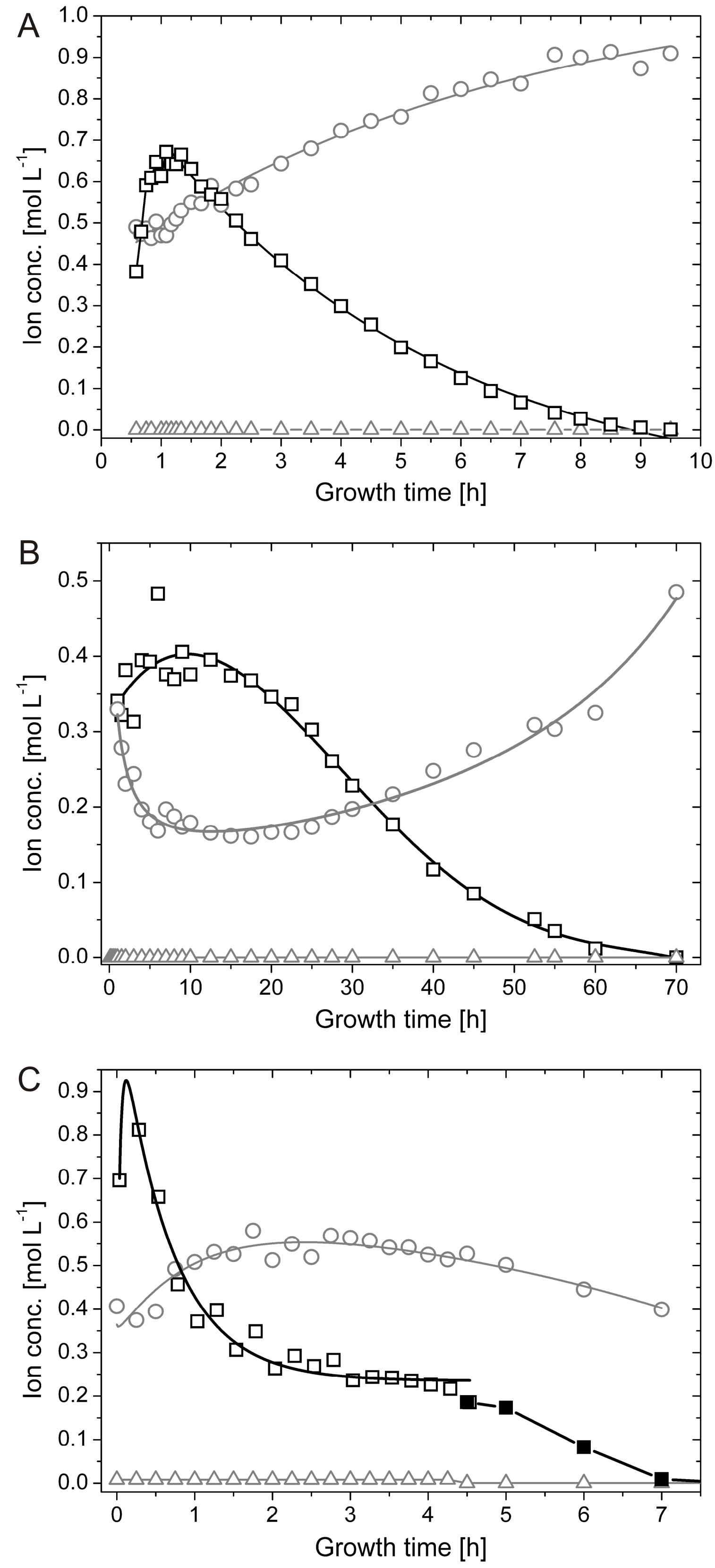

Fig. 54: Time-dependent concentration profiles for divalent metal cations (squares), sodium ions (circles), and silicate species (triangles) in the interior solution of open-tube silica gardens prepared with pellets of (A) $CoCl_2$, (B) $FeCl_2$, and (C) $FeCl_3$ (full squares indicate samples taken after solidification of the interior solution had commenced).

3.1. General Trends

For the three studied types of silica gardens, there are several general similarities concerning the progression of species concentrations in the solutions on both sides of the membrane. First of all, no significant changes in concentration could be distinguished for any of the elements in the exterior silica solution (Fig. 55), due to the huge excess of water glass used for preparation and the poor solubility of multivalent cations in strongly alkaline environments.

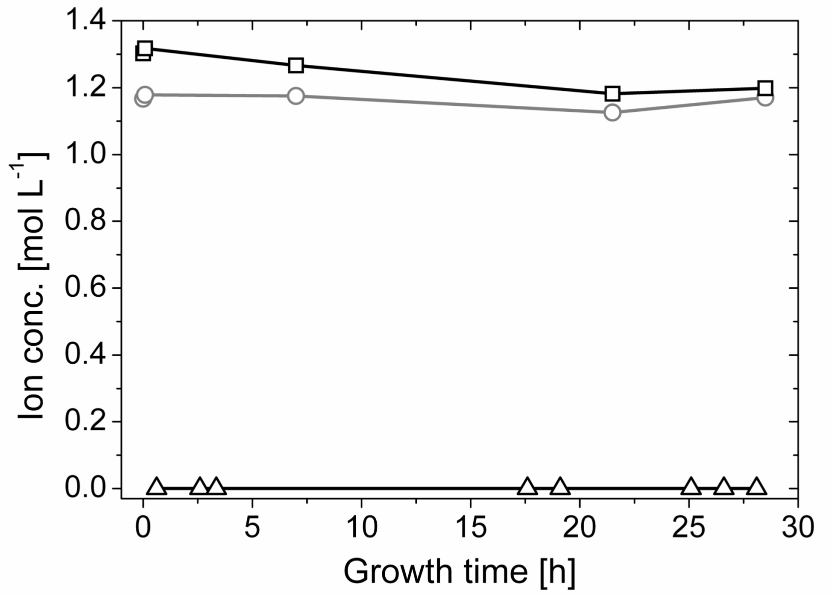

Fig. 55: Measured iron (triangles), sodium (circles) and silicate (squares) ion concentrations as a function of time in the outer water glass reservoir of $FeCl_3$-based silica gardens, indicating quasi-constant conditions. Corresponding data for silica gardens prepared with $FeCl_2$ and $CoCl_2$ were essentially identical and are therefore not shown.

As opposed to that, the curves of the interior metal ion concentrations exhibit a more or less pronounced initial increase which, upon having reached a maximum after differing times, turns into an exponential decrease down to quite low and constant values at the end of the experiments. The amount of sodium inside the tube walls tends to increase over a rather long period of several hours, starting at concentrations of 0.15-0.4 M and reaching values of up to 0.9 M at the end of the examined timeframe. Obviously, a considerable quantity of sodium ions must have entered the interior side of the membrane while an intact tube separating the two solutions was formed. In a second step, sodium ions diffuse gradually through the membrane wall into the interior solution, provoking a further slow increase in concentration over hours, the detailed shape of which varies depending on the type of metal salt used. Apparently, a noticeable sodium ion concentration gradient exists over the membrane even in the long term (e.g. still after 70 hours in the case of $FeCl_2$). This suggests that the tube walls remained intact and no inflow of Na^+ through possible leaks occurred, and that the only feasible way of transport for the ions is diffusion.

In contrast to the above, no significant amounts of silicate could be detected in the interior solutions of all three studied silica garden systems at any time. This finding can be explained by the drastic decrease in pH across the membrane, given that the outer silica sol is highly alkaline (pH~12) while the inner metal salt solution is slightly acidic. Silicate ions trying to penetrate the tube wall become subject to protonation at lower pH and thus liable to condensation reactions.[32] Therefore, the solubility of silica is drastically reduced (cf. section II.1.3 and Fig. 5) and quantitative precipitation occurs, resulting in the amorphous silica-rich regions previously identified on the exterior surface of the tube walls.[17]

3.2. Differences between the Studied Metal Salts

The most obvious difference in the progressions of species concentrations between the three types of silica gardens examined is the actual period during which diffusion and/or precipitation processes are active. This period ranges from roughly 9 hours for silica gardens based on $FeCl_3$ (Fig. 54C) to several days in the case of $FeCl_2$ (Fig. 54B). Reasons for these discrepancies might be related to the different acidities of the used metal salts (see Tab. 7).

Metal salt	**pK_a (298 K) [43]**
$CoCl_2 \cdot 6\,H_2O$	9.6 ± 0.1 (pK_1)
$FeCl_2 \cdot 4\,H_2O$	9.3 ± 0.5 (pK_1)
$FeCl_3 \cdot 6\,H_2O$	2.4 ± 0.1 (pK_1)
	5.7 ± 0.1 (pK_2)

Tab. 7: Acidities of the used metal salts.[96]

Precipitation of metal silicate should be accelerated by metal cations with higher acidity, given that the solubility of silica strongly depends on the pH. These processes are expected to be fastest in the presence of the most acidic cation, herein Fe^{3+}. Therefore, the membranes formed in silica gardens based on $FeCl_3$ should be least dense and exhibit largest pores, which allow for a more efficient exchange between the two solutions surrounding them. As a consequence, the time needed for the system to equilibrate should be shortest in the case of Fe^{3+}, which is in fact observed. Similar arguments can be put forward when considering the solubility of the respective metal hydroxides (see Tab. 8). Since $Fe(OH)_3$ is substantially less soluble than the other two hydroxides, it will be removed most rapidly from the interior solution and hence accelerate the overall evolution of the corresponding silica garden.

Metal hydroxide	**Solubility products**
$Co(OH)_2$	$5.92 \cdot 10^{-15}$ mol^3 L^{-3}
$Fe(OH)_2$	$4.87 \cdot 10^{-15}$ mol^3 L^{-3}
$Fe(OH)_3$	$2.79 \cdot 10^{-39}$ mol^4 L^{-4}

Tab. 8: Solubility products of metal hydroxides.[97]

A second distinction between the three studied systems can be made concerning the progression of the interior metal ion concentrations at later times. While the amount of free ions decreases exponentially and falls eventually below the detection limit in the case of both $CoCl_2$ and $FeCl_2$, the concentration of Fe^{3+} in corresponding silica gardens levels off at moderate values around 0.25 M after approximately 4 hours (Fig. 54C, open squares). Visual observations confirm that the interior solution starts to solidify at this point, which complicates further extraction of samples for AES measurements. As precipitation proceeds, the measured Fe^{3+} concentration decreases again in the following and a yellow-brownish solid gradually fills the entire interior volume. After about 7 hours, no more iron could be detected by AES inside the tube indicating quantitative precipitation (Fig. 54C, full squares). Careful removal of parts of the precipitate with the aid of a pipette creates a small funnel within the open tube, which slowly becomes filled with clear colourless liquid. Continued AES analyses of this solution revealed that the sodium and in particular also the silica concentration now increase with time over a period of more than 35 hours (Fig. 56).

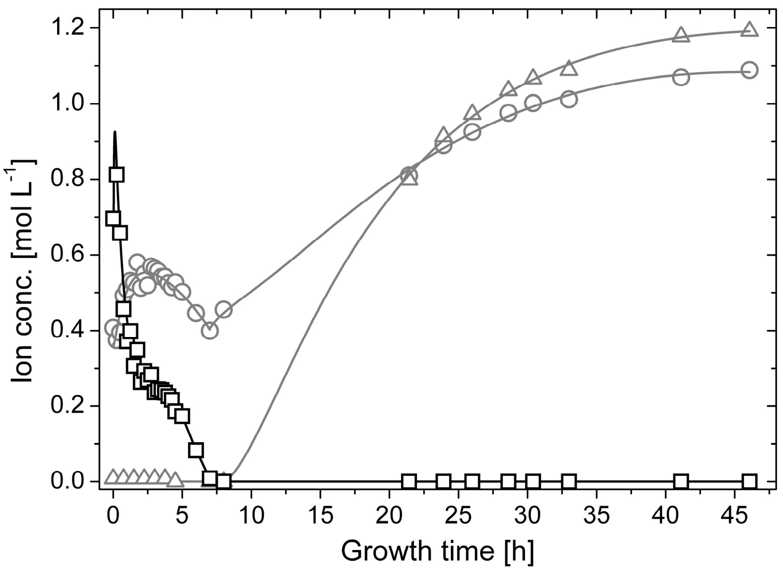

Fig. 56: Long-term evolution of iron (squares), sodium (circles) and silicate (triangles) ion concentrations in the interior solution of $FeCl_3$-based silica gardens over a period of 48 hours.

Starting at 0.4 M for [Na^+] and values below the detection limit for silica after 7 hours, the concentrations of the two species at the end of the experiment after 48 hours are [Na^+] = 1.1 M and [SiO_2] = 1.2 M. In both cases, final inner concentrations are thus only slightly lower than those determined experimentally for the outer water glass solution (Fig. 55). This indicates that the system is close to equilibrium at this stage, and diffusion must succumb as concentration gradients vanish. The gradual increase in the concentration of the two species demonstrates that the walls were still intact after detaching pieces of the precipitate, as in case of a leaking membrane a much faster increase would be expected. Therefore, it can be concluded that the traced time-dependent concentration changes are due to intimate ion diffusion processes across the membrane walls.

During the solidification of the tube interior, two samples of the precipitating matter were isolated after 5 and 15 h for EDX analysis to obtain more information about the composition of the precipitate. The resulting qualitative EDX spectra, depicted in Fig. 57, reveal significant differences in the elemental composition of the extracted precipitate. While no silicon and oxygen could be detected after 5 h in the tube interior (Fig. 57a), significant amounts of the two elements were found in the precipitate taken after 15 h (Fig. 57b). This is clear evidence for a delayed in-diffusion of silicate ions, thus confirming the results of the AES measurements presented in Fig. 56. Results from

EDX measurements further indicate that, at first, small amounts of Fe(OH)$_3$ precipitate in the interior, followed by solidification of significant amounts of silicate at later times.

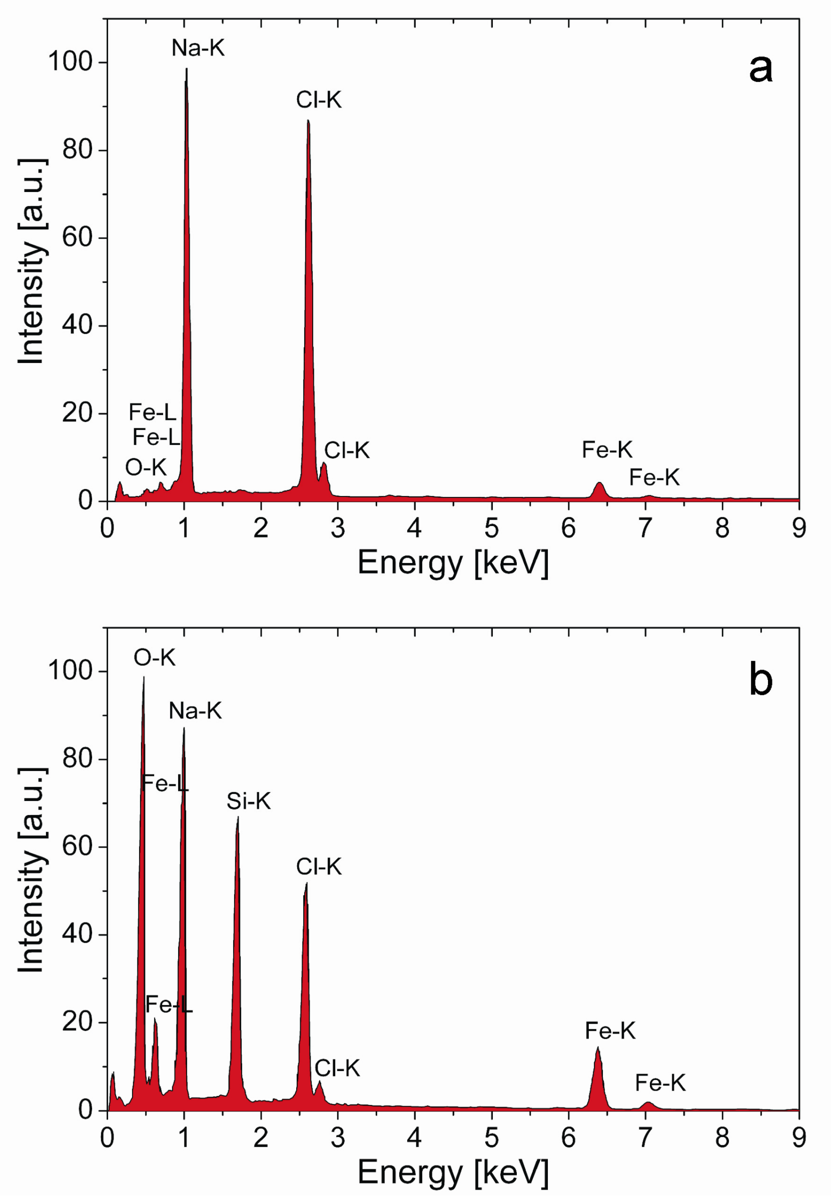

Fig. 57: EDX spectra of gelified material from the tube interior of a FeCl$_3$ based silica garden, isolated (a) 5 and (b) 15 hours after tube preparation, respectively.

It is worth to mention that the significantly varying intensity ratios of Na/Fe between both spectra originate from the different nature of the precipitate in the tube interior at different times; after 5 h, the precipitate was less condensed and of pulpy consistence, while it became much more densified when isolated after 15 h.

3.3. Variation of the Metal Salt Counter-Ion

In order to gain full insight to the spatiotemporal distribution of all species (including the counter-ion), AES measurements were done on samples drawn from the interior solutions of as-grown CoI_2 silica gardens and yielded in concentration profiles as reproduced in Fig. 58.

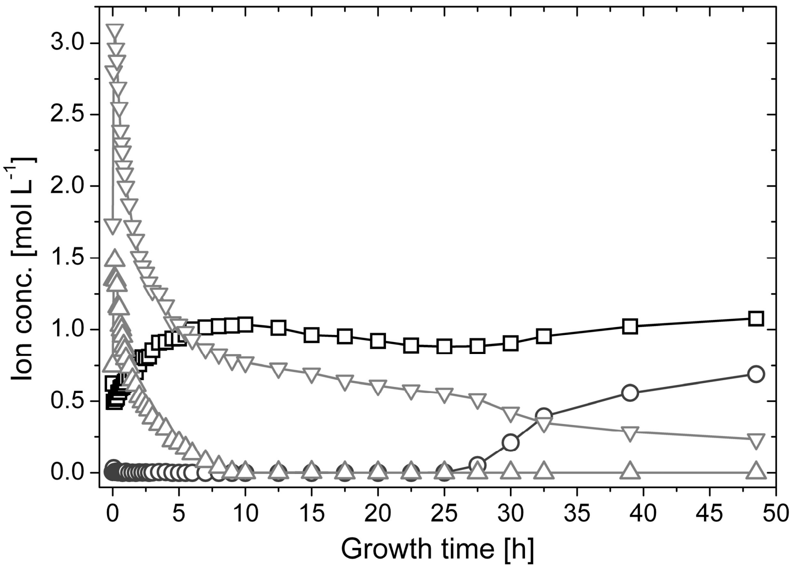

Fig. 58: Progressions of interior cobalt (triangles), iodide (tilted triangles), silicate (circles) and sodium (squares) ion concentrations in silica gardens prepared with CoI_2.

Results agree well with those obtained for the silica gardens prepared with cobalt(II) chloride (cf. Fig. 54A). Again, no silicate is detected inside the tube for a period of more than 24 hours, and the sodium concentration increases from initially 0.5 M to values around 1.1 M after 10 hours. Likewise, the Co^{2+} concentration is found to decrease exponentially with time, and only differs with respect to the initial value, which can most probably be ascribed to varying preparation conditions (different pellet size (type B) and rate of water glass addition). Unlike the experiments done with $CoCl_2$, concentration progressions were recorded for an extended timeframe of 48 hours in order to monitor possibly occurring delayed diffusion processes, as in the case of $FeCl_3$ (Fig. 56). At times greater than 10 hours, a slight decrease in the sodium concentration from 1.1 to 0.9 M after 25 hours can be observed, which is followed by a re-increase towards the end of the experiment. The latter feature is accompanied by a significant and much more pronounced rise in the silica concentration. Even after 48 hours, the interior concentrations of the two species, especially of the silica, deviate notably from those determined in the surrounding water glass solution ($[Na^+]_{int}$ = 1.1 M and $[SiO_2]_{int}$ = 0.7 M vs. $[Na^+]_{ext} \approx [SiO_2]_{ext} \approx$ 1.2 M). As opposed to the $FeCl_3$-based silica garden, the system appears to be still far from equilibrium at the end of the investigated period.

Measurements of the iodide content in the inner metal salt solution showed that its concentration, initially being around 3 M, decreases with time in a similar manner as the cobalt concentration, but does not drop to zero. Instead, a plateau at about 0.75 M is reached after 10 hours, subsequent to which a slow decrease down to 0.25 M after 48 hours can be discerned. To clarify whether the iodide ions were incorporated into the precipitated membrane material or underwent diffusion through the membrane, samples were also taken from the outer silica sol after different times and analyzed for iodide. A comparison of the concentration profiles found for the solutions within and outside the walls reveals a reciprocal correlation between the respective iodide contents over the entire studied frame of time (Fig. 59).

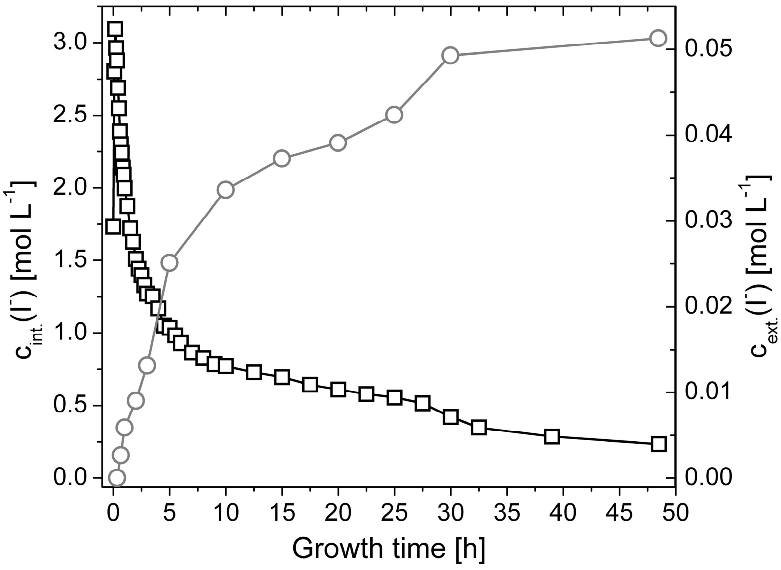

Fig. 59: Iodide concentration profiles for the interior (squares) and exterior (circles) solution in CoI_2-based silica gardens.

This is clear evidence that the anions diffuse from the inside of the silica garden tube through the membrane into the surrounding water glass reservoir. To get an idea about the amount of iodide ions penetrating through the membrane into the exterior water glass, a rough calculation is done in the following:

Assuming a homogeneous distribution for the iodide ions in the bulk of the exterior and interior solution, the quantities of the anions present in the two volumes at the beginning and the end of the experiments can be calculated. For preparation, 0.3 g solid cobalt(II) iodide hydrate were introduced to the system, giving a total molar amount of ~2 mmol iodide [$M(CoI_2 \cdot H_2O) = 330.8\ g\ mol^{-1}$]. Dissolution of the metal salt pellet, formation of the membrane and diffusion of iodide ions into the outer solution effectuate a final inner iodide concentration of about 0.25 M, which corresponds to 0.08-0.125 mmol when approximating the volume inside the tube to 0.3-0.5 mL. In turn, analogous calculations for the outer reservoir ($V \approx 40$ mL, $[I^-]_{final.} \approx 50$ mM) result in an overall molar content of ~2 mmol after 48 hours. Thus, within the limits of error, diffusion of iodide ions through the membrane seems to be more or less quantitative in the course of the experiment.

The thus proven more or less quantitative diffusion of iodide ions through the membrane consequently rules out any significant co-precipitation of iodide with the metal hydroxides and silicates into the membrane.

Obviously, the walls of conventional silica gardens are not semi-permeable in the true sense, but rather allow bidirectional diffusion of multiple ionic species.

4. Evolution of pH in Open-Tube Silica Gardens

To shed more light on diffusion processes in silica garden systems, the pH of both the exterior and interior solution was monitored continuously over prolonged periods of time. In all cases, there were no significant changes in pH detected in the outer water glass reservoir even after days of maturation due to the high excess and in particular the buffering ability of silica. On the other hand, the pH of the inner metal salt solution was found to evolve delicately in the course of the experiments. Typical time-dependent profiles are shown in Fig. 60.

Generally, while starting in the acidic range (pH < 7), the pH increases with time and eventually approaches alkaline values between 11-11.5 after different periods depending on the chosen metal salt (about 9 h for $FeCl_3$, 14 h for $CoCl_2$, and 45 h for $FeCl_2$). The measured final pH values inside the tube are similar to those prevailing in the outer silica sol, indicating that ongoing processes are essentially terminated and the system is close to equilibrium.

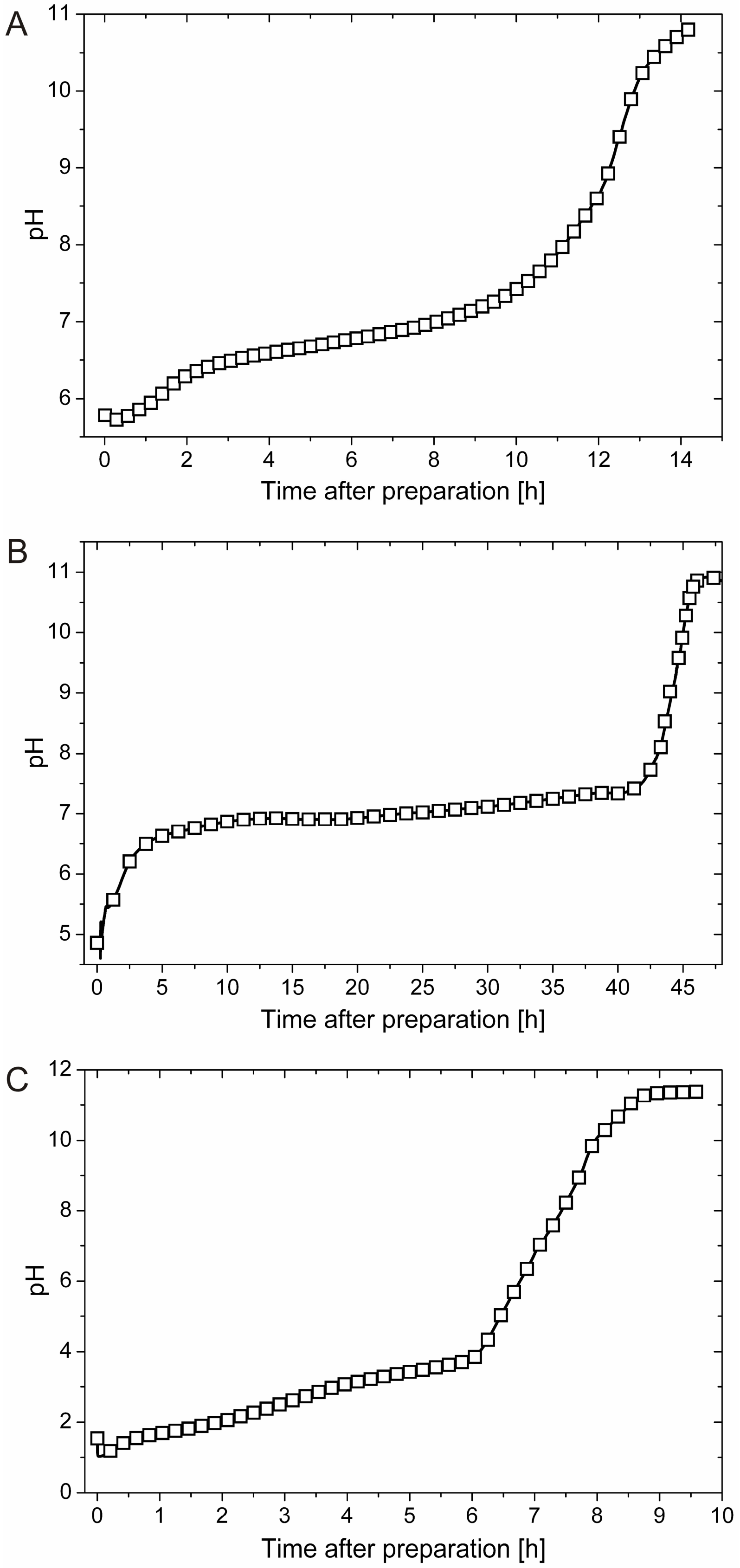

Fig. 60: Evolution of pH with time in interior solutions of silica gardens prepared with (A) $CoCl_2$, (B) $FeCl_2$ and (C) $FeCl_3$.

A closer inspection of the pH curves suggests a classification into two different stages. First, the pH increases slowly to adopt more or less neutral values (pH ≈ 7 for $CoCl_2$ and $FeCl_2$ and pH ≈ 4 for $FeCl_3$) after roughly 6, 10 and 40 h for Fe^{3+}, Co^{2+} and Fe^{2+}, respectively. In the following, a fairly steep rise in pH up to the final (equilibrium) level of about 11.5 is observed in all systems within a period of 2-5 hours. On the whole, the recorded pH progressions thus strongly resemble the appearance of common acid-base titration curves. Reasonably, data reflect the removal of acidic multivalent metal cations from the inner salt solution as a consequence of metal hydroxide and silicate precipitation. Thereby, silica gardens prepared with $CoCl_2$ and $FeCl_2$ (Fig. 60A and Fig. 60B) again show akin behavior, while the results obtained for $FeCl_3$ (Fig. 60C) differ in some fundamental respects. Most strikingly, the initial pH of interior solutions is much more acidic in the latter (pH~1-2) than in the former case (pH~5-6). This difference can be ascribed to the higher acidity of iron(III) chloride as compared to iron(II) and cobalt(II) metal salts (cf. Tab. 7). While Fe^{2+} and Co^{2+} ions act as weak, quasi-monoprotic acids in aqueous solution, hydrated Fe^{3+} ions are strong to medium-strong diprotic acids. Therefore, dissolved Fe^{3+} causes relatively low starting pH values inside the tube and in addition buffers the system, keeping the pH in the acidic range until consumption of metal ions by precipitation, i.e. neutralization, is nearly completed.

Exemplarily, the pH and the concentration of free metal ions were determined simultaneously (by means of AES) for a $CoCl_2$-based silica garden. Correlating the temporal progression of the two parameters (Fig. 61) clearly demonstrates that the pH remains acidic as long as significant amounts of Co^{2+} ions are present in the interior solution. Once all metal ions are quantitatively eliminated by precipitation (here after 9-10 h), the pH starts to increase rapidly finally heading towards the value of the outer silica sol.

Previous studies have indicated that the incorporation of multivalent metal ions to the interior surface of the forming membranes occurs mainly through precipitation in the form of amorphous hydroxides.[17, 24] Findings of this work are in line with these observations, given that the removal of metal ions is completed before measurable traces of silicate species have entered the inner solution. Further, the obtained data evidence that halide anions are not co-precipitated to a noticeable degree with the cations. The material characterizing the interior side of the membrane must hence in fact be more or less pure metal hydroxide.

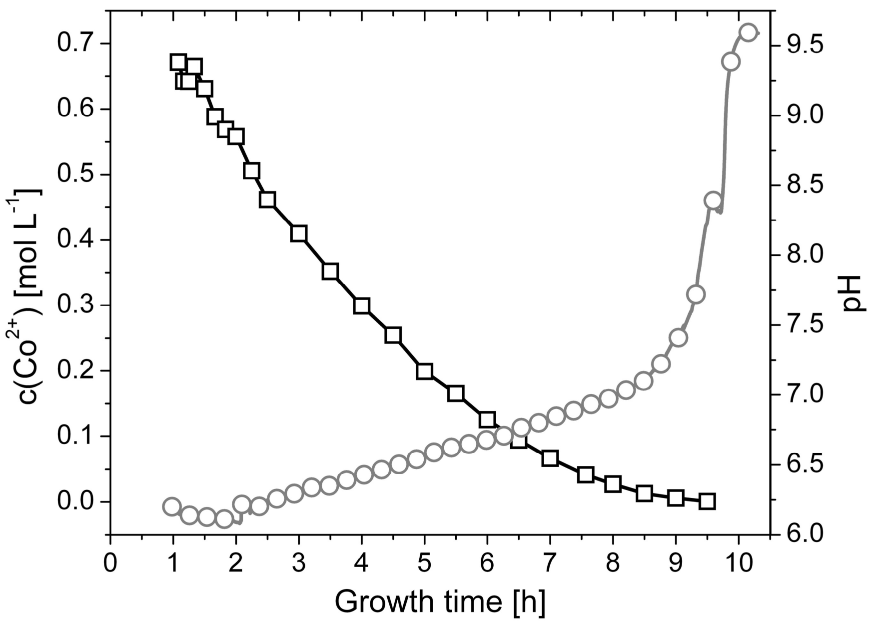

Fig. 61: Time-dependent development of pH (circles) and the cobalt ion concentration (squares) inside the tube of a silica garden prepared with $CoCl_2$.

However, this premises diffusion of hydroxide ions from the outer water glass reservoir across the tube membrane. Once arrived at the inner surface, OH^- ions precipitate as sparsely soluble metal hydroxides during the first stage when the interior solution is still rich in metal cations. This process leads to a continuous decrease in the concentration of free metal ions, and in parallel to a slight increase in pH. As soon as all metal ions are consumed, i.e. the point of equivalence is reached, further diffusion of hydroxide ions into the interior solution provokes a much more distinct rise in pH until eventually the concentration difference in hydroxide ions between the inside and outside of the open-tube system vanishes and the pH is the same in both reservoirs. Figuratively speaking, the inner metal salt solution is thus “titrated” with strong base by continuous diffusion of hydroxide ions. All in all, it can therefore be concluded that the performed *in-situ* pH measurements provide direct evidence for the permeability of conventional silica garden membranes for hydroxide ions, as it was proposed in earlier work.[7, 15, 23-24]

Influence of Trace Amounts of Hydroxide Ions on the pH of Interior Solutions

To check whether the evolution of the interior pH is dominated by the presence and gradual consumption of acidic metal cations or by possible other effects (e.g. temporally increasing amounts of hydroxide ions), the pH measured inside the tube of $CoCl_2$-based silica gardens was compared to values theoretically expected for pure Co^{2+} solutions at concentrations equal to those determined by AES for the interior solution after distinct times (Fig. 62).

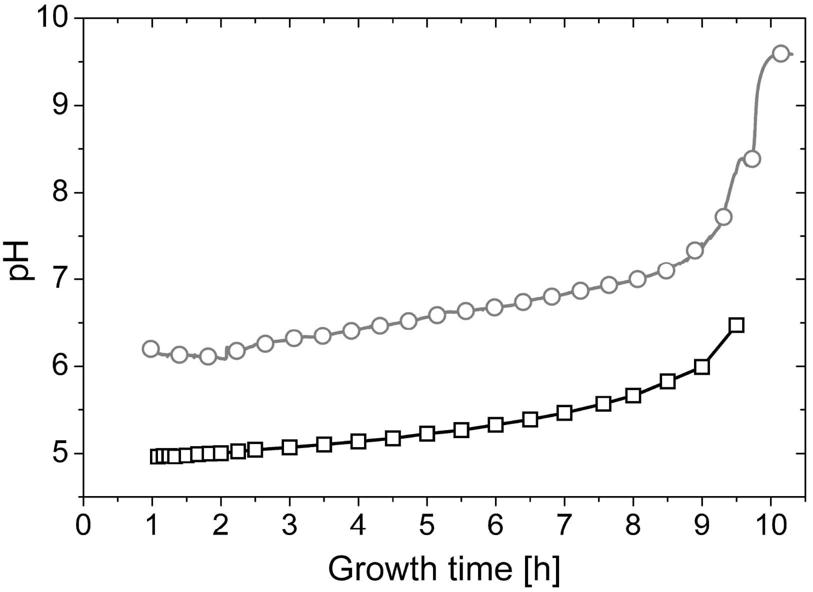

Fig. 62: Comparison of the pH measured in the interior solution of a silica garden prepared with $CoCl_2$ after different times (circles) to theoretical values calculated for pure aqueous Co^{2+} solutions (squares), showing a more or less constant deviation of 1-1.5 pH units over the entire period studied.

Theoretical values were calculated according to the following equation:[98]

$$pH(t) = \frac{1}{2} \cdot \left[\mathrm{pK_a} - \lg\left([\mathrm{Co}^{2+}](t) \cdot \frac{\mathrm{L}}{\mathrm{mol}} \right) \right] \qquad (22)$$

with $[Co^{2+}](t)$ being the concentrations measured by AES at different times t and assuming a pK_a of 9.7 for the cations.[96]

Calculated curves show a qualitatively similar progression, yet with a more or less constant shift in pH by about 1-1.5 units towards more acidic values. This deviation can be explained when assuming that a certain amount of hydroxide ions has entered the inner solution early during the onset of silica garden growth, while subsequently remaining on a constant low level.

To verify these speculations, aqueous $CoCl_2$ solutions with different concentrations ($[Co^{2+}]$ = 0.02-1 M) were titrated with 0.02 M sodium hydroxide, up to a final NaOH content of 1 mM. Thereby, a marked increase in pH by more than 1 unit was observed in all experiments, even at high cobalt salt concentrations (Fig. 63). From this, it can be derived that an initial minor uptake of hydroxide ions can readily account for the elevated pH measured inside the walls of silica gardens, as compared to theoretically expected values.

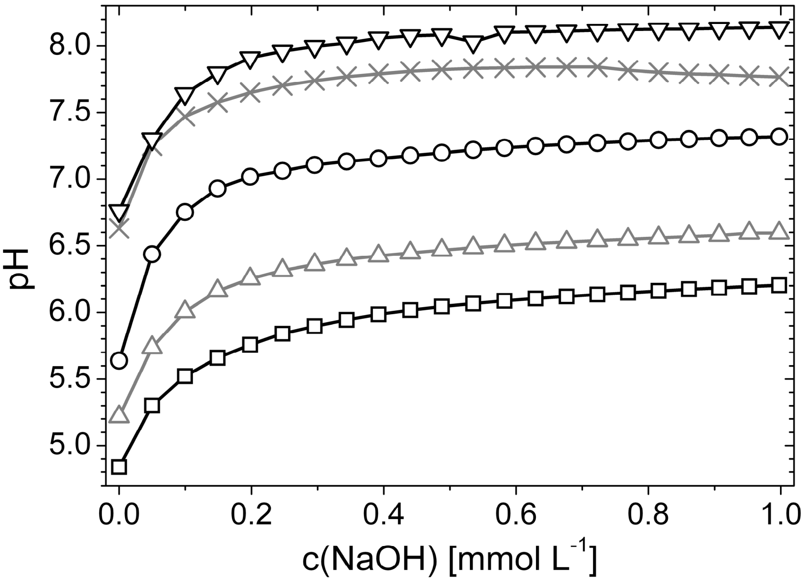

Fig. 63: The pH of aqueous Co^{2+} solutions as a function of the NaOH content, as determined by titration of 1.00 M (squares), 0.60 M (triangles), 0.20 M (circles), 0.06 M (crosses), and 0.02 M (tilted triangles) $CoCl_2$ solution with 0.02 M NaOH. Addition of minor amounts of NaOH to fairly concentrated solutions of Co^{2+} leads to an increase in pH by about 1-1.5 units for all measured concentrations. Precipitation of cobalt(II) hydroxide was not observed in any of the titration experiments. Results are in good agreement with previous studies on aqueous $Co(NO_3)_2$ solutions.[99]

Based on these findings and the results for the inner Na^+ concentration (cf. Fig. 56 and Fig. 58), it can be inferred that significant portions of both sodium and hydroxide ions are transported from the outer alkaline reservoir to the interior metal salt solution at the very beginning of silica garden formation. However, while the sodium remains dissolved after passing the membrane, most of the hydroxide is precipitated on the inner membrane surface and only small amounts of free OH^- ions persist in the interior solution, effecting the observed slight increase in pH.

5. Evolution of Potential Differences in Chemical Garden Systems

Based on the above presented results on long-lasting chemical gradients across the membrane walls, it seems reasonable to assume that the electrochemical potential in the two compartments must be substantially different. To check this, potential differences between the inner and outer solutions of chemical garden systems prepared from $CoCl_2$, $FeCl_2$ and $FeCl_3$ were studied using pairs of either platinum or silver/silver chloride electrodes in an assembly as described in section III.3.5 (cf. Fig. 34 and Fig. 39c).

5.1. Curves of the Recorded Cell Potentials

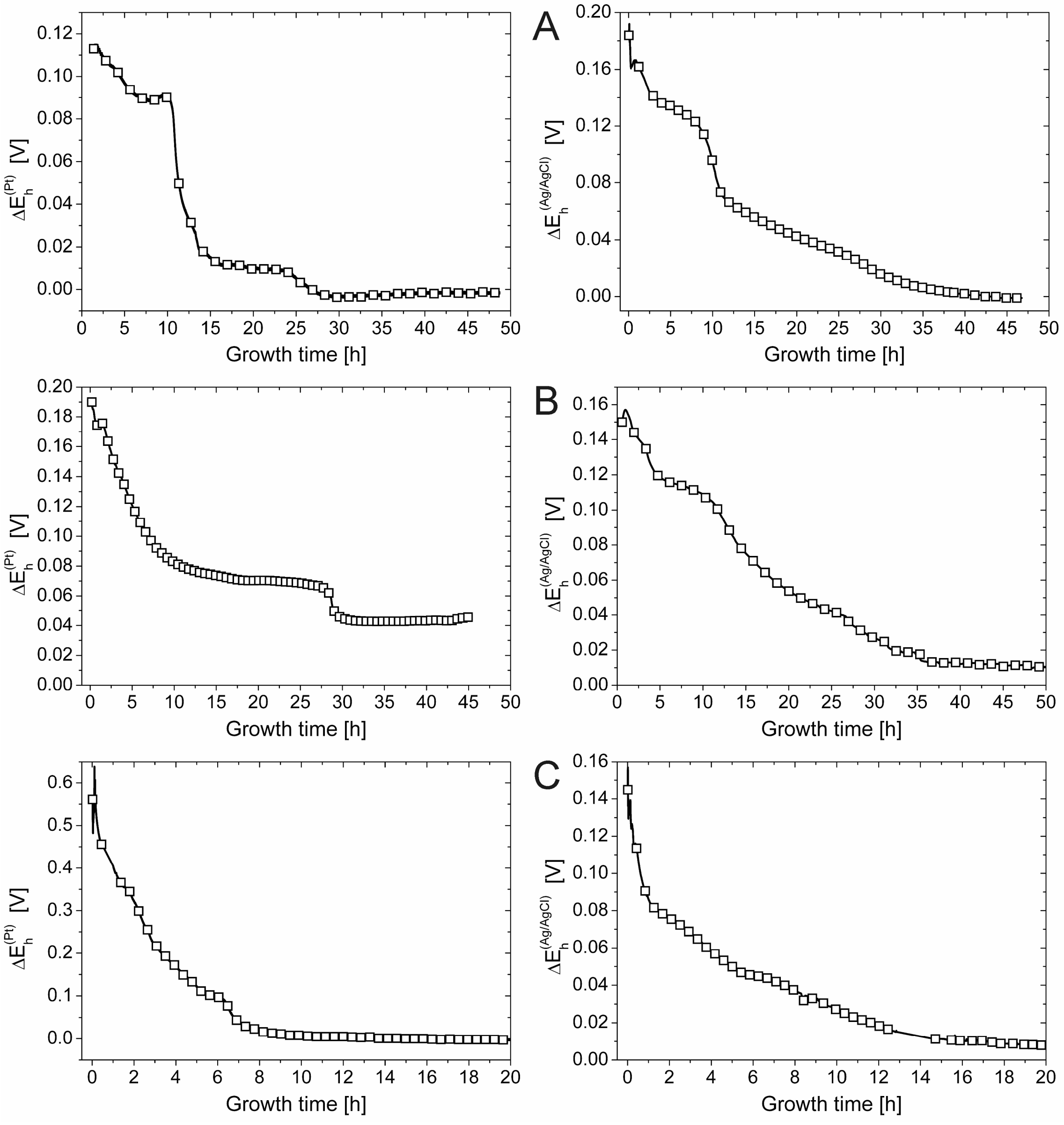

Fig. 64: Evolution of electrochemical potential differences ΔE_h across the membrane of silica gardens prepared with pellets of (A) $CoCl_2$, (B) $FeCl_2$ and (C) $FeCl_3$, as determined by using a set of identical Pt- (left) or Ag/AgCl (right) electrodes, respectively.

Remarkable voltages were measured in all three silicate garden systems immediately after tube preparation, which decayed with time (Fig. 64). The detailed progression of the potential difference ΔE_h depends on the type of metal salt used and electrodes employed for measurement.

5.1.1. ΔE_h in $CoCl_2$ Silicate Gardens

In a setup involving Pt electrodes, the measured potential $\Delta E_h^{(Pt)}$ decreases only slightly during the first 10 h from initially ~115 mV to around 90 mV (Fig. 64A, left), obviously because the presence of metal ions keeps the interior solution acidic and thus maintains a marked pH gradient over the tube wall ($\Delta pH \approx$ 5-6, cf. Fig. 58). Upon completion of cobalt hydroxide precipitation, the cell potential drops to ~10 mV within about 5 h as the interior pH switches to alkaline values and the gradient is considerably diminished ($\Delta pH < 1$, cf. Fig. 60A). Subsequently, $\Delta E_h^{(Pt)}$ remains stable for a period of 10 h before, after ~25 h, another decrease is observed and the potential difference vanishes. This last step coincides with the onset of silicate diffusion into the tube (cf. Fig. 58), which ultimately eliminates any residual concentration gradients.

Time-dependent profiles obtained for the cell potential using Ag/AgCl electrodes (Fig. 64A, right) exhibit initial $\Delta E_h^{(Ag/AgCl)}$ values around 180 mV and subsequently also a similar stepwise decrease after identical growth times and can thus be interpreted likewise. However, steps observed at ~10 h and ~25 h are less pronounced and the cell potential decreases more continuously in comparison to the experiment using Pt electrodes. This deviation indicates that the cell potential is not only determined by the pH gradient but also by the evolution of other ion concentration differences, especially including chloride ions.

5.1.2. ΔE_h in $FeCl_2$ Silicate Gardens

In general, cell potentials in the $FeCl_2$-silicate systems also evolve in several steps, similar to the $CoCl_2$ system. However, in case of using the Pt electrodes, only two stepwise decreases are recorded within the period of measurement (Fig. 64B, left). A first, exponential-like decrease from ~190 mV to ~65 mV takes place during the first 28 hours of growth, followed by a second smaller but more distinct step down to a cell potential of ~40 mV, which was maintained until abortion of measurement after 45 hours. As the cell potential $\Delta E_h^{(Pt)}$ still deviates from zero, thermodynamic equilibrium is obviously not yet reached and concentration gradients are not yet completely eliminated by diffusion.

When Ag/AgCl electrodes were used, cell potentials decrease more or less constantly from ~155 mV at the beginning to ~10 mV after 37 h, subsequently remaining constant until the end of the experiment at 50 h (Fig. 64B, right). The resulting potential curve exhibits only a very weak step after ~26 h, in contrast to experiments using Pt electrodes.

Again, comparison of the potential measurements performed with Pt and Ag/AgCl electrodes reveals a decrease of the cell potentials within similar periods of growth (>35 h), though reproducibility is already limited in this system.

5.1.3. ΔE_h in $FeCl_3$ Silicate Gardens

The evolution of the electrochemical potential differences in the $FeCl_3$-silicate system is given in Fig. 64C. Again, significant cell potentials were detected independent of the used type of electrodes.

However, the values of the detected potential gradients significantly differ from each other, which is in contrast to the other two examined systems. While the initial cell potential $\Delta E_h^{(Pt)}$ was in the range of ~550 mV (Fig. 64C, left), only ~150 mV were recorded when Ag/AgCl electrodes were applied (Fig. 64C, right).

This discrepancy might be caused by the different nature of the electrodes. While Pt exhibits a higher affinity towards protons, Ag/AgCl electrodes are less sensible towards H^+ ions. As the pH gradient in the $FeCl_3$-silicate system is significantly higher due to the higher acidity of the Fe^{3+} (cf. Fig. 60C), an increased cell potential results when Pt electrodes are employed.

In addition, both curves not only differ in the absolute values of the cell potentials but also in the period until low and constant cell potentials are reached. While the cell potential $\Delta E_h^{(Pt)}$ is completely eliminated after ~8 h, $\Delta E_h^{(Ag/AgCl)}$ deviates from zero for a period of $t \geq 15$ h.

5.2. Explanations for the Observed Potential Differences

In order to provide an explanation for the existence and evolution of the measured cell potentials (Figure 4 in the main text), a simplified model of a silicate garden system is introduced and successively refined step by step below.

5.2.1. Diffusion and Membrane Potentials across a Precipitated Tube Wall

Assuming, in an initial step, that the walls of silicate gardens are generally permeable to all ion species present in the system (except for the multivalent metal ions which become subject to complete precipitation), a phase scheme for the setup used for the detection of cell potentials comprising Pt electrodes can be established as follows:

$$\text{Pt (s)}\left|\begin{pmatrix}[\mathrm{H}^+],[\mathrm{M}^{z+}],[\mathrm{Cl}^-], \\ [\mathrm{Na}^+],[\mathrm{H_3SiO_4^-}],[\mathrm{OH}^-]\end{pmatrix}_{\text{int.}}\text{(aq.)}\ \vdots\ \begin{pmatrix}[\mathrm{H}^+],[\mathrm{Cl}^-], \\ [\mathrm{Na}^+],[\mathrm{H_3SiO_4^-}],[\mathrm{OH}^-]\end{pmatrix}_{\text{ext.}}\text{(aq.)}\right|\text{Pt (s)}$$

Herein, the vertical line | represents the phase interface between the solution and a Pt electrode, and the precipitated tube wall which is permeable for all present ions is symbolized by a broken vertical line ¦. Silicate ions are considered to exist only in the singly charged form $H_3SiO_4^-$, as this is the dominant species present in equilibrium under the alkaline conditions prevailing in the used sol (pH ~ 12).

In a situation where the concentrations of all ions differ between the interior and exterior solution, the overall theoretical diffusion potential ΔE_{diff} can be expressed by means of the Henderson equation (23):[100]

$$\Delta E_{diff} = \frac{RT}{F}\cdot\left(\frac{\sum_{\mathrm{i}}\left[a_i^I - a_i^{II}\right]u_i\frac{|z_i|}{z_i}}{\sum_{\mathrm{i}}\left[a_i^I - a_i^{II}\right]u_i|z_i|}\right)\cdot\ln\left(\frac{\sum_{\mathrm{i}} a_i^{II}u_i|z_i|}{\sum_{\mathrm{i}} a_i^{I}u_i|z_i|}\right), \tag{23}$$

wherein T represents the temperature, R is the universal gas constant and F is the Faraday constant. a_i corresponds to the activity of ion species i on side (I) or (II) of the tube wall. In a first approximation, activities can be replaced by molar concentrations ($a_i \approx c_i$). z_i is the ion charge and u_i represents the ion mobility of species i, which can be derived from its equivalent ionic conductivities λ_i by equation (24):

$$u_i = \frac{\lambda_i}{z_i \cdot F}. \tag{24}$$

For a silica garden prepared with dilute silica sol and solid $CoCl_2$, the Henderson equation can thus be written as

$$\Delta E_{diff} = \frac{RT}{F}\left\{\left[\frac{\begin{pmatrix}\underset{\text{I-II}}{\Delta}[\mathrm{Na}^{+}]u_{Na^{+}} - \underset{\text{I-II}}{\Delta}[\mathrm{H_3SiO_4^{-}}]u_{H_3SiO_4^{-}} - \underset{\text{I-II}}{\Delta}[\mathrm{OH^{-}}]u_{OH^{-}}\\ + \underset{\text{I-II}}{\Delta}[\mathrm{Co}^{2+}]u_{Co^{2+}} - \underset{\text{I-II}}{\Delta}[\mathrm{Cl^{-}}]u_{Cl^{-}} + \underset{\text{I-II}}{\Delta}[\mathrm{H^{+}}]u_{H^{+}}\end{pmatrix}}{\begin{pmatrix}\underset{\text{I-II}}{\Delta}[\mathrm{Na}^{+}]u_{Na^{+}} + \underset{\text{I-II}}{\Delta}[\mathrm{H_3SiO_4^{-}}]u_{H_3SiO_4^{-}} + \underset{\text{I-II}}{\Delta}[\mathrm{OH^{-}}]u_{OH^{-}}\\ + \underset{\text{I-II}}{\Delta}[\mathrm{Co}^{2+}]u_{Co^{2+}} + \underset{\text{I-II}}{\Delta}[\mathrm{Cl^{-}}]u_{Cl^{-}} + \underset{\text{I-II}}{\Delta}[\mathrm{H^{+}}]u_{H^{+}}\end{pmatrix}}\right]\cdot\ln\left[\frac{\begin{pmatrix}[\mathrm{Na}^{+}]^{\mathrm{II}}\cdot u_{Na^{+}} + [\mathrm{H_3SiO_4^{-}}]^{\mathrm{II}}\cdot u_{H_3SiO_4^{-}} + [\mathrm{OH^{-}}]^{\mathrm{II}}\cdot u_{OH^{-}}\\ +2\cdot[\mathrm{Co}^{2+}]^{\mathrm{II}}\cdot u_{Co^{2+}} + [\mathrm{Cl^{-}}]^{\mathrm{II}}\cdot u_{Cl^{-}} + [\mathrm{H^{+}}]^{\mathrm{II}}\cdot u_{H^{+}}\end{pmatrix}}{\begin{pmatrix}[\mathrm{Na}^{+}]^{\mathrm{I}}\cdot u_{Na^{+}} + [\mathrm{H_3SiO_4^{-}}]^{\mathrm{I}}\cdot u_{H_3SiO_4^{-}} + [\mathrm{OH^{-}}]^{\mathrm{I}}\cdot u_{OH^{-}}\\ +2\cdot[\mathrm{Co}^{2+}]^{\mathrm{I}}\cdot u_{Co^{2+}} + [\mathrm{Cl^{-}}]^{\mathrm{I}}\cdot u_{Cl^{-}} + [\mathrm{H^{+}}]^{\mathrm{I}}\cdot u_{H^{+}}\end{pmatrix}}\right]\right\} \tag{25}$$

With this expression, it is possible to calculate the diffusion potential ΔE_{diff} theoretically expected for the system at a given time by using experimentally determined pH and ion concentration data as well as the equivalent ionic conductivities and ion mobilities given in Tab. 9.

Ion species		**λ_0 [cm^2 Ω^{-1} mol^{-1} z^{-1}]**	**u$_i$ [m^2 s^{-1} V^{-1}]**
Cations	H^+	349.8	$3.63\cdot10^{-7}$
	Na^+	50.1	$5.19\cdot10^{-8}$
	Co^{2+}	55	$2.85\cdot10^{-8}$
	Fe^{2+}	53.5	$2.77\cdot10^{-8}$
	Fe^{3+}	68	$2.35\cdot10^{-8}$
Anions	OH^-	198.3	$2.06\cdot10^{-7}$
	Cl^-	76.35	$7.91\cdot10^{-8}$
	I^-	76.9	$7.97\cdot10^{-8}$
	$H_3SiO_4^-$	30-35	$3.42\cdot10^{-8}$

Tab. 9: Equivalent ionic conductivities (λ_0) at infinite dilution and ion mobilities (u_i) for participating cations and anions present in the silicate garden systems.[97, 101-102]

However, as diffusion of several ion species was found to be blocked either permanently (in case of the multivalent metal ions) or temporarily (for hydroxide and silicate ions) by proceeding precipitation processes (cf. Fig. 54, Fig. 56, Fig. 58 and Fig. 60), the tube wall cannot exclusively be regarded as a diaphragm (which is permeable for all ion species) but also has properties of a membrane, which is completely or over certain periods impermeable for the mentioned ions.

Consequently, the measured potential differences may also originate from membrane potentials, which are generated by different ion concentrations across the precipitated membrane and are temporarily maintained by the apparent "semi-permeable" nature of the wall. It should be emphasized that the ability of the membrane to block penetrating ions can, however, not be regarded as true semi-permeability in the classical sense, because suppression of ion diffusion is not caused by size exclusion mechanisms but rather by elimination of ions due to precipitation processes.

Two models exist which describe the formation of potential differences across a semi-permeable membrane. In the first model, the membrane is totally and permanently impermeable for at least one ion species, while all other ions as well as water molecules are able to pass through. Starting from different ion concentrations in both separated compartments, concentration gradients of permeable ions are then diminished by diffusion processes, while the gradients of the blocked ion species remain unchanged. When the system reaches thermodynamic equilibrium and there is no net ion flow across the membrane, the resulting equilibrium potential (Donnan potential) is determined by the concentration ratio of the permeable ion species in both compartments according to the Nernst equation:[103]

$$\Delta E_{Donnan} = \frac{RT}{z_i F} \cdot \ln \frac{a_i^{II}}{a_i^{I}} \tag{26}$$

Yet, this model only allows for an estimation of static potential differences in the status of thermodynamic equilibrium and cannot be applied to describe dynamic processes in evolving systems. Therefore, it is not suitable to explain the potential differences found in silica gardens. Indeed, the fact that the equilibrium potential observed at the end of measurements (cf. Fig. 64) is close to zero for all examined silicate garden systems (except for $FeCl_2$ based silicate gardens, which is caused by premature termination of the potential measurements) confirms this notion and is clear evidence that the walls of silica gardens do not possess persisting semi-permeable characteristics

Therefore, an alternative second model must be chosen, in which the membrane potential is created and dominated by the imperfectness of the semi-permeable properties. In this case, the relative permeability (P_i) of the membrane to each ion species i is taken into account during the evaluation of the resulting membrane potential (ΔE_m), which is then given by the Goldman-Hodgkin-Katz (GHK) voltage equation:[103]

$$\Delta E_m = \frac{RT}{F} \cdot \ln \left(\frac{\sum_{\mathrm{j}}^{\mathrm{m}} P_{M_j^+} \cdot [\mathrm{M}_{\mathrm{j}}^{+}]^{II} + \sum_{\mathrm{k}}^{\mathrm{n}} P_{A_k^-} \cdot [\mathrm{A}_{\mathrm{k}}^{-}]^{I}}{\sum_{\mathrm{j}}^{\mathrm{m}} P_{M_j^+} \cdot [\mathrm{M}_{\mathrm{j}}^{+}]^{I} + \sum_{\mathrm{k}}^{\mathrm{n}} P_{A_k^-} \cdot [\mathrm{A}_{\mathrm{k}}^{-}]^{II}} \right) \tag{27}$$

Actually, the GHK equation describes resting membrane potentials under constant conditions and, in its original form, only includes monovalent metal ions (M^+) and anions (A^-). Therefore, this model must be extended to also consider multivalent ions.

Assuming the formation of a membrane potential across the precipitated wall of a silicate garden tube prepared from sodium silicate and $CoCl_2$, the following expression can be derived for the membrane potential:[103-104]

$$\Delta E_m = \frac{RT}{F} \cdot \ln\left(\frac{P_{H_3SiO_4^-} \cdot [H_3SiO_4^-]^I + P_{Cl^-} \cdot [Cl^-]^I + P_{OH^-} \cdot [OH^-]^I + P_{H^+} \cdot [H^+]^{II} + P_{Na^+} \cdot [Na^+]^{II} + 4P'_{Co^{2+}} \cdot [Co^{2+}]^{II}}{P_{H_3SiO_4^-} \cdot [H_3SiO_4^-]^{II} + P_{Cl^-} \cdot [Cl^-]^{II} + P_{OH^-} \cdot [OH^-]^{II} + P_{H^+} \cdot [H^+]^I + P_{Na^+} \cdot [Na^+]^I + 4P'_{Co^{2+}} \cdot [Co^{2+}]^I \cdot e^{\Delta E_m F/RT}} \right) \quad (28)$$

In this expression, concentrations of all participating ions in the exterior (Na^+, $H_3SiO_4^-$, OH^-) and interior (Co^{2+}, Cl^-) cell compartment as well as their relative permeabilities (P_i, P_j') are taken into account, with

$$P'_{Co^{2+}} = P_{Co^{2+}} \cdot \left(\frac{1}{1 + e^{\Delta E_m F/RT}} \right).$$

With respect to the above, the overall potential difference prevailing between the two reservoirs at a given time, $\Delta E_h(t)$, should result from the interplay of diffusion and membrane potentials, and can hence be written as the sum of both contributions:

$$\Delta E_h\,(t) = \Delta E_{diff}\,(t) + \Delta E_m(t) \quad (29)$$

Combining equations (23) and (27) then leads to the following generalized expression

$$\Delta E_h = \frac{RT}{F} \cdot \left\{ \left(\frac{\sum_i^l \left[a_i^I - a_i^{II} \right] u_i \frac{|z_i|}{z_i}}{\sum_i^l \left[a_i^I - a_i^{II} \right] u_i |z_i|} \right) \cdot \ln\left(\frac{\sum_i^l a_i^{II} u_i |z_i|}{\sum_i^l a_i^I u_i |z_i|} \right) + \ln\left(\frac{\sum_j^m P_{M_j^+} \cdot [M_j^+]^{II} + \sum_k^n P_{A_k^-} \cdot [A_k^-]^I}{\sum_j^m P_{M_j^+} \cdot [M_j^+]^I + \sum_k^n P_{A_k^-} \cdot [A_k^-]^{II}} \right) \right\} \quad (30)$$

which, in analogy to equation (25) and (28), can be converted to a working equation for a silica garden prepared with $CoCl_2$ by introducing concentrations (under the assumption of ideal solutions) and permeabilities for the involved ions on both sides of the wall:

$$\Delta E_h = \frac{RT}{F}\left\{ \begin{aligned} &\left[\frac{\left(\begin{aligned}&\underset{\text{I-II}}{\Delta}[\mathrm{Na}^+]u_{Na^+} - \underset{\text{I-II}}{\Delta}[\mathrm{H_3SiO_4^-}]u_{H_3SiO_4^-} - \underset{\text{I-II}}{\Delta}[\mathrm{OH^-}]u_{OH^-}\\ &+\underset{\text{I-II}}{\Delta}[\mathrm{Co}^{2+}]u_{Co^{2+}} - \underset{\text{I-II}}{\Delta}[\mathrm{Cl^-}]u_{Cl^-} + \underset{\text{I-II}}{\Delta}[\mathrm{H^+}]u_{H^+}\end{aligned}\right)}{\left(\begin{aligned}&\underset{\text{I-II}}{\Delta}[\mathrm{Na}^+]u_{Na^+} + \underset{\text{I-II}}{\Delta}[\mathrm{H_3SiO_4^-}]u_{H_3SiO_4^-} + \underset{\text{I-II}}{\Delta}[\mathrm{OH^-}]u_{OH^-}\\ &+\underset{\text{I-II}}{\Delta}[\mathrm{Co}^{2+}]u_{Co^{2+}} + \underset{\text{I-II}}{\Delta}[\mathrm{Cl^-}]u_{Cl^-} + \underset{\text{I-II}}{\Delta}[\mathrm{H^+}]u_{H^+}\end{aligned}\right)}\right] \cdot \ln\left[\frac{\left(\begin{aligned}&[\mathrm{Na}^+]^{II} u_{Na^+} + [\mathrm{H_3SiO_4^-}]^{II} u_{H_3SiO_4^-} + [\mathrm{OH^-}]^{II} u_{OH^-}\\ &+2\cdot[\mathrm{Co}^{2+}]^{II} u_{Co^{2+}} + [\mathrm{Cl^-}]^{II} u_{Cl^-} + [\mathrm{H^+}]^{II} u_{H^+}\end{aligned}\right)}{\left(\begin{aligned}&[\mathrm{Na}^+]^{I} u_{Na^+} + [\mathrm{H_3SiO_4^-}]^{I} u_{H_3SiO_4^-} + [\mathrm{OH^-}]^{I} u_{OH^-}\\ &+2[\mathrm{Co}^{2+}]^{I} u_{Co^{2+}} + [\mathrm{Cl^-}]^{I} u_{Cl^-} + [\mathrm{H^+}]^{I} u_{H^+}\end{aligned}\right)}\right] \\ &+ \ln\left(\frac{P(t)_{H_3SiO_4^-}[\mathrm{H_3SiO_4^-}]^I + P(t)_{OH^-}[\mathrm{OH^-}]^I + P_{Cl^-}[\mathrm{Cl^-}]^I + P_{H^+}[\mathrm{H^+}]^{II} + P_{Na^+}[\mathrm{Na^+}]^{II} + 4P'_{Co^{2+}}[\mathrm{Co}^{2+}]^{II}}{P(t)_{H_3SiO_4^-}[\mathrm{H_3SiO_4^-}]^{II} + P(t)_{OH^-}[\mathrm{OH^-}]^{II} + P_{Cl^-}[\mathrm{Cl^-}]^{II} + P_{H^+}[\mathrm{H^+}]^{I} + P_{Na^+}[\mathrm{Na^+}]^{I} + 4P'_{Co^{2+}}[\mathrm{Co}^{2+}]^{I}\cdot e^{\Delta E_m F/RT}}\right) \end{aligned} \right\} \tag{31}$$

Results from AES analyses (cf. Fig. 58 and Fig. 59) and pH measurements (cf. Fig. 60A) on silicate gardens prepared from $CoCl_2$ and CoI_2 were used to calculate temporal progressions of ΔE_{diff}, ΔE_m and ΔE_h with the aid of equations (23), (28) and (30).

For this purpose, the permeabilities of the distinct ion species are needed, which, however, are *a priori* unknown. To estimate these values, it seems reasonable to assume that the permeability of any ion species depends on its size as well as on its mobility. Therefore, and since relative magnitudes are sufficient, P_i was taken to be the ratio of the ionic mobility (u_i) (cf. Tab. 9) and the hydrated ionic radius (r_{ih}) according to:

$$P_i \propto \frac{u_i}{r_{ih}} \tag{32}$$

Values for the ionic radii were either directly taken from literature or derived from corresponding hydrated molar ionic volumes,[S7] except for r_h of $H_3SiO_4^-$, which had to be estimated as there was no information available in literature. Data are listed together with the resulting relative permeability for each of the involved ions in Tab. 10.

Ion species		Hydrated molar ionic volume (V_{ih}^{∞}) [cm^3 mol^{-1}]	Hydrated ionic radius (r_{ih}) [Å]	Relative ion permeability (P_i)
Cations	Na^+	109.0	3.51	0.65
	H^+	---	2.82	5.5
	Co^{2+}	169.6	4.07	0
Anions	Cl^-	93.6	3.34	1
	I^-	92.8	3.33	1
	OH^-	---	3.00	3
	$H_3SiO_4^-$	---	(3.3)	0.5

Tab. 10: Hydrated ionic radii r_{ih}, as reported in literature or derived from molar ionic volumes V_{ih}^{∞},[105] as well as the resulting permeabilities P_i for the different ions present in $CoCl_2$- and CoI_2-based silica gardens, respectively.

As already indicated above, the permeabilities of the participating ion species do not only differ from each other, but partially also become subject to alterations during the evolution of the system with time and only reach the values given in Tab. 10 once quantitative precipitation at the wall has expired. With regard to the collected pH (cf. Fig. 60A) and ion concentration data (Fig. 58 and Fig. 59), this holds true essentially for hydroxide ions (whose transport through the wall is negligible within the first 10 hours but becomes possible at later times) as well as for silicate species (whose diffusion was found to be blocked for even longer times, such that noticeable concentrations were detected only after more than 20 hours in the interior solution). In turn, AES analyses show that sodium and chloride ions can readily diffuse through the tube wall over the entire growth period investigated, whereas permanent impermeability applies for the cobalt ions due to quantitative precipitation under alkaline conditions.

On this account, constant P_i values of 1, 0.65 and 0 were used for chloride/iodide, sodium and cobalt at all times. The permeabilities of hydroxide and silicate ions were adjusted such that they are zero before noticeable in-diffusion occurs, and then vary between 0-3 and 0-0.5 (cf. Tab. 11), respectively, until the next data point is reached and precipitation is no longer active. These circumstances are illustrated in Fig. 65. Moreover, as the relative permeabilities of iodide and chloride exhibit identical values, data acquired from silica gardens prepared with CoI_2 were combined with those obtained from systems based on $CoCl_2$ (note that CoI_2 was used in some experiments because iodide ions could be traced with the employed AES instrument, whereas chloride ions could not).

Growth time [h]	P(Cl^-)	P(Na^+)	P(H^+)	P(OH^-)	P($H_3SiO_4^-$)	P(Co^{2+})
0-10	1	0.65	0	0	0	0
10-15	1	0.65	0-5.5	0-3	0	0
15-20	1	0.65	5.5	3	0	0
20-50	1	0.65	5.5	3	0-0.5	0

Tab. 11: Assumed relative ion permeabilities P_i(t) for all participating species in a $CoCl_2$ based silicate garden at different growth times.

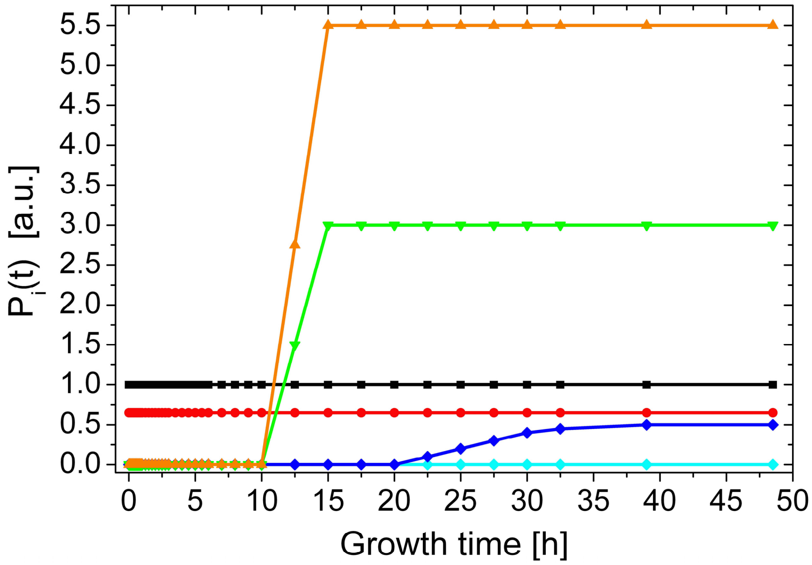

Fig. 65: Plot of the values assumed for the relative permeability $P_i(t)$ of chloride (black), sodium (red), hydroxide (green), oxonium (orange), silicate (blue) and cobalt (cyan) ions in a $CoCl_2$-based silicate garden at different growth times

From concentration values determined by AES and pH measurements, combined with the assumed permeabilities of all relevant ions given in Tab. 11, progressions of ΔE_{diff}, ΔE_m and ΔE_h were then calculated using equations (23), (28) and (30), respectively. Ideality was assumed for the system, therefore ion activities were replaced by their molar concentrations. Results of these calculations are depicted in Fig. 66.

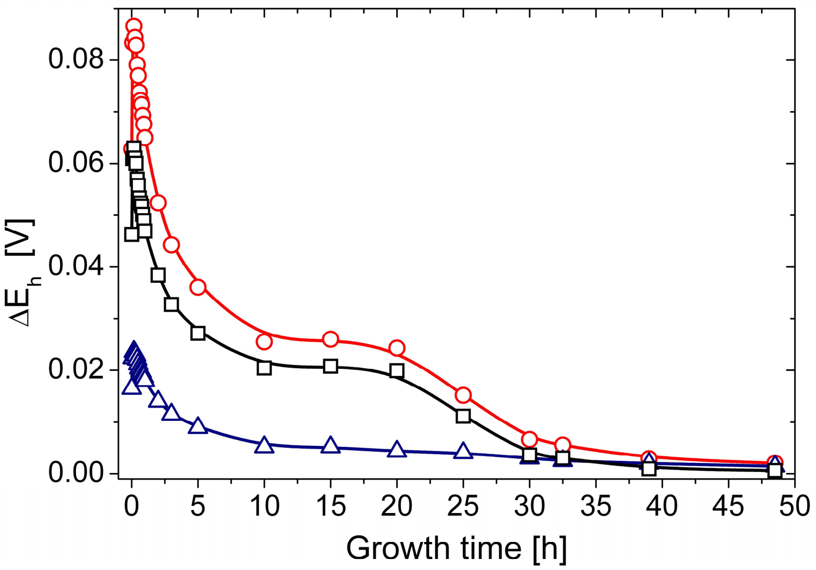

Fig. 66: Curves of diffusion *(*ΔE_{diff}, blue triangles), membrane (ΔE_m, black squares) and overall potential (ΔE_h, red circles) in a CoI_2 based silicate garden, calculated from results of AES concentration measurements according to equation (23), (28) and (30), respectively.

As visible from Fig. 66, calculated courses of the membrane (ΔE_m, black squares) and diffusion (ΔE_{diff}, blue triangles) potentials both exhibit an exponential-like decrease within the first 10 hours, followed by a period of 10 hours with constant potentials. At growth times between 20-40 h, a second stepwise decrease can be observed for both potentials before ending up in constant potential values close to zero. Superposition of ΔE_{diff} and ΔE_m results in a curve for the overall potential (ΔE_h, red circles), exhibiting starting values around ~90 mV and final potentials around zero voltage. Apparently, ΔE_h is dominated by the membrane potential, while the diffusion potential plays a less important role.

Fig. 67 gives a comparison of calculated ΔE_h values with potentials that were directly measured in a $CoCl_2$-based silica garden using Pt electrodes. It is evident that both curves show generally good agreement, especially at times greater than 15 h where calculated values nearly coincide with experimental ones even in absolute terms. This suggests that the implemented model of an interplay between membrane and diffusion potentials is well suitable to describe the phenomena occurring in the as-prepared silica gardens and, furthermore, that the assumptions made for estimating relative permeabilities are widely acceptable.

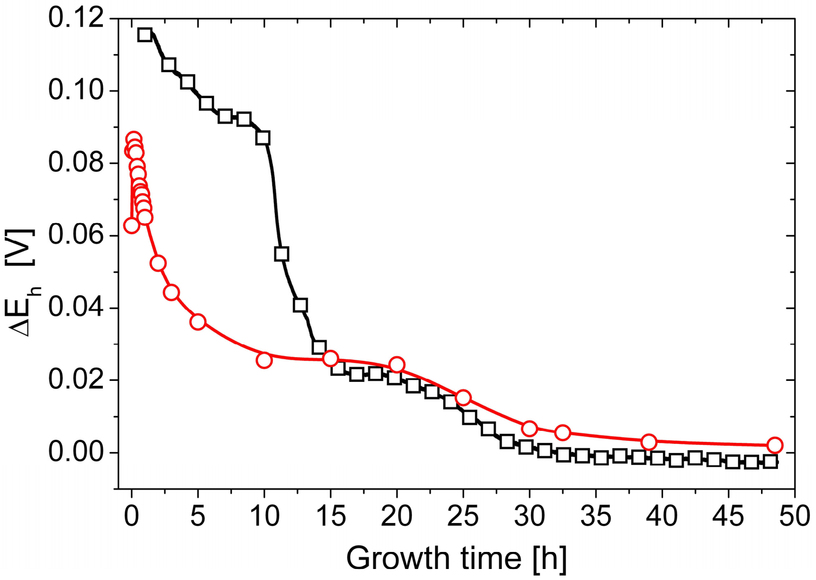

Fig. 67: Comparison of ΔE_h curves obtained from direct measurements in a $CoCl_2$ based silicate garden (black squares) and by calculation from AES concentration data in a CoI_2 silicate system (red circles, cf. Fig. 66), respectively.

However, there is also significant discrepancy between the two curves in Fig. 67: while the theoretically expected potential (red circles) decays continuously and in an exponential-like manner from ~90 mV to ~25 mV within the first 10 h, measured values (black squares) exhibit only a relatively weak decrease from ~115 mV to ~90 mV during the same period, before dropping steeply down to ~20 mV in the following 5 h.

To obtain a better understanding about the reasons for this noticeable deviation of both curves in the first period from 0-10 h, it is worth to draw attention to other possible processes which might occur under real experimental conditions within this first period. Especially, a closer look on the correlations between the evolution of the potential and pH differences seems to be of special interest.

5.2.2. Correlation between the Evolution of ΔE_h and ΔpH

By using data from above presented pH and potential measurements (cf. Fig. 60 and Fig. 64), a detailed comparison of both parameters was realized for the three examined silicate garden types based on $CoCl_2$, $FeCl_2$, and $FeCl_3$, respectively. Results are depicted in Fig. 68.

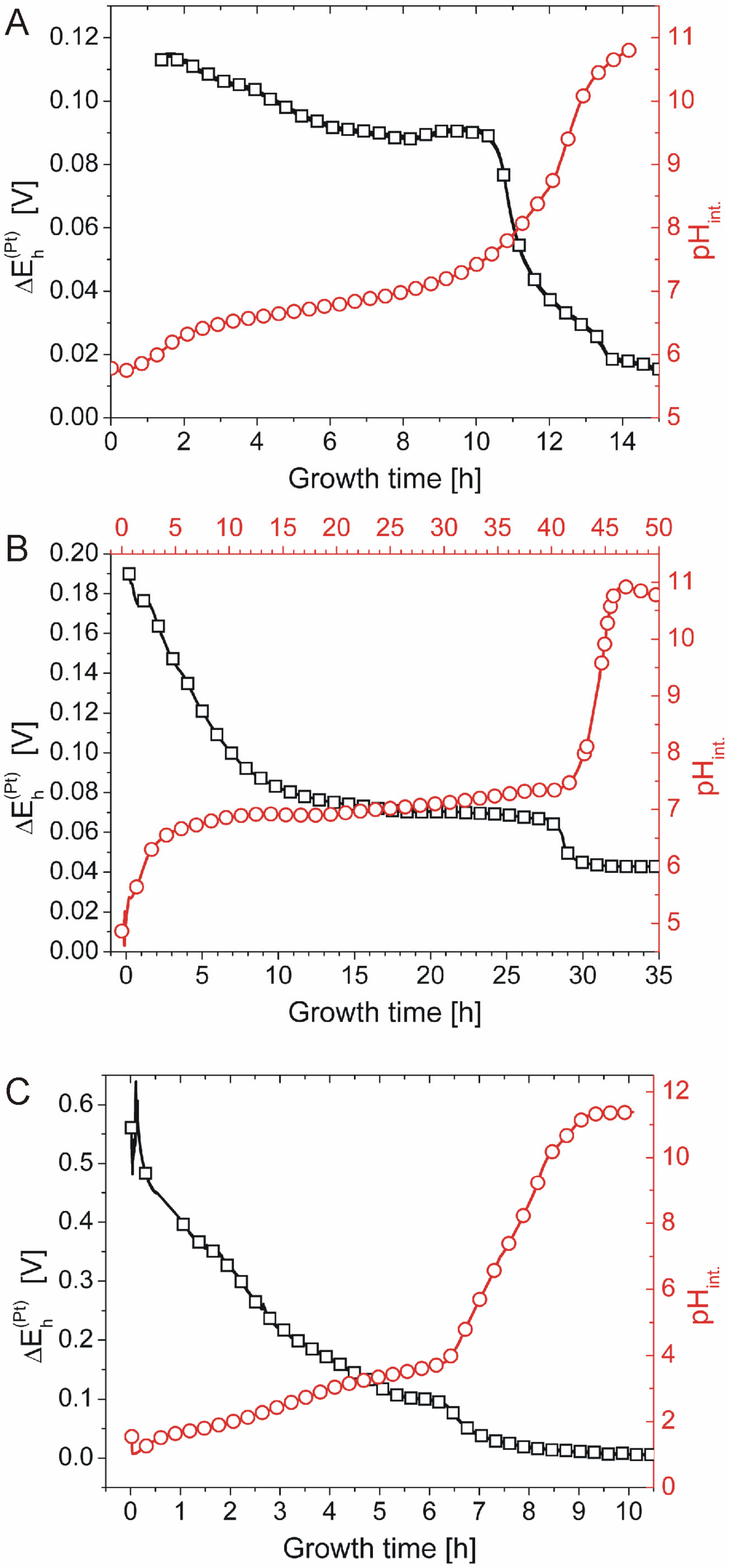

Fig. 68: Correlation between the evolution of cell potentials and $pH_{int.}$ for silicate garden systems prepared from (A) $CoCl_2$, (B) $FeCl_2$ and (C) $FeCl_3$ pellets.

Progressions of the curves uncover coinciding alterations in both parameters for all three examined silicate garden systems, that is, the potential drops to markedly lower values almost at the same time as a sharp increase in pH is observed and the pH difference between the two compartments tends to zero. This correlation is strong evidence that the measured potentials are substantially affected by existing pH gradients across the tube walls during this period. As the pH of the interior solutions is determined by the concentration of the dissolved metal ions (which act as Lewis acids), pH slowly increases with ongoing metal ion elimination by precipitation of new wall material. Accompanied, potential differences decrease significantly as the pH gradient across the membrane is diminished by precipitation and delayed in-diffusion of hydroxide and silicate ions.

5.2.3. Explanations for the Existence of a pH-induced Extra-Potential

Two different explanations can be found for the observed strong influence of the pH gradient on the detected cell potentials (section IV.5.2.2) and thus for the deviation between the calculated and experimentally obtained curves of ΔE_h (cf. Fig. 67). Both different models will be presented in the following.

5.2.3.1.Generation of a Redox Potential by Existing pH Gradients

The first argumentation involves the existence of possible redox potentials in the used experimental system. A theoretical setup comprising two identical Pt electrodes immersed into compartments separated by a membrane in contact with the atmosphere can be described by the following phase scheme:

$$\mathrm{Pt\,(s)}\;\big|\;\mathrm{O_2^{atm.}\,(g)}\;\big|\;[\mathrm{H^+}]_{\mathrm{ext.}}\mathrm{(aq)}\;\big\|\;[\mathrm{H^+}]_{\mathrm{int.}}\mathrm{(aq)}\;\big|\;\mathrm{O_2^{atm.}\,(g)}\;\big|\;\mathrm{Pt\,(s)}$$

As no other redox-active species are present in the system, a redox potential might possibly originate from existing proton gradients in the system. As oxygen is also present in the system, the same corresponding redox pair is present in both compartments, but in different concentrations. For this reason, the half-cell potentials for the following hypothetical reaction differ in both separated solutions:

$$4\,\mathrm{H^+} + 4\,\mathrm{e^-} + \mathrm{O_2} \longrightarrow 2\,\mathrm{H_2O}$$

When assuming, in a rough approximation, ideality for both solutions, the pH induced redox potential ΔE_{pH} can be written as a difference of the both half-cell potentials, giving the following expression:

$$\Delta E_{pH} = E_{pH}^{int.} - E_{pH}^{ext.} = -\frac{\mathrm{RT}}{4\mathrm{F}} \cdot \ln\left(\frac{[\mathrm{H}^+]_{\mathrm{ext.}}}{[\mathrm{H}^+]_{\mathrm{int.}}}\right)^4 = \frac{\mathrm{RT}}{\mathrm{F}} \cdot \ln 10 \cdot \left(\mathrm{pH}_{\mathrm{ext.}} - \mathrm{pH}_{\mathrm{int.}}\right) \quad (33)$$

The resulting redox potential should therefore be proportional to the pH gradient across the membrane:

$$\Delta E_{pH} \propto \Delta pH \quad (34)$$

5.2.3.2.Additional Membrane Potentials by Hydroxide Concentration Gradients

A second explanation for the observed correlation between pH gradients and cell potentials ΔE_h lies in the circumstances that the silicate/hydroxide membrane is impermeable for hydroxide ions within the first period of 10-15 h, consequently maintaining a high pH gradient. Therefore, an extra potential is generated by the difference in hydroxide ion concentrations in both compartments due to the following argumentation:

Assuming that the electrochemical potential for OH^- is equal at both sides of the membrane within this first period, the following equation applies

$$\mu_{OH^-}^{0} + RT\ln a_{OH^-}^{int.} + zF\,E_{pH}^{int.} = \mu_{OH^-}^{0} + RT\ln a_{OH^-}^{ext.} + zF\,E_{pH}^{ext.}\,. \quad (35)$$

As the standard chemical potential μ^0_{OH} is the same for both solutions, ,and with $z = -1$, this expression simplifies to

$$RT\ln a_{OH^-}^{int.} - F\,E_{pH}^{int.} = RT\ln a_{OH^-}^{ext.} - F\,E_{pH}^{ext.}\,. \quad (36)$$

With $a_{OH,}$ being the activity of OH^- in the exterior and interior compartment, the pH-induced potential difference (ΔE_{pH}) between both sides of the wall finally results in

$$\Delta E_{pH} = E_{pH}^{ext.} - E_{pH}^{int.} = \frac{RT}{F}\left(\ln a_{OH^-}^{ext.} - \ln a_{OH^-}^{int.}\right) = \frac{RT}{F}\ln\left(\frac{a_{OH^-}^{ext.}}{a_{OH^-}^{int.}}\right). \quad (37)$$

With $pOH = -\lg a_{OH^-}$ and $pOH + pH = pK_W$, equation (37) becomes:

$$\Delta E_{pH} = \frac{RT}{F}\ln 10\left(pOH_{int.} - pOH_{ext.}\right) = \frac{RT}{F}\ln 10\left(pH_{ext.} - pH_{int.}\right). \tag{38}$$

Thus, the potential difference arising from persisting hydroxide ion (or, equivalently, proton) concentration gradients across the tube wall should be proportional to the actual pH difference between the compartments:

$$\Delta E_{pH} \propto \Delta pOH \propto \Delta pH \tag{39}$$

5.2.3.3.Comparison of the two Models with Experimental Data

Both presented models yield identical correlations between existing pH gradients and the generation of a pH-induced potential, ΔE_{pH} (cf. equations (33) and (38)).

To check, whether these equations sufficiently elucidate the observed discrepancy between the two ΔE_h curves plotted in Fig. 67, potential values calculated on the basis of equation (31) (= $\Delta E_{diff} + \Delta E_m$) were subtracted from experimentally measured ones (= ΔE_h).

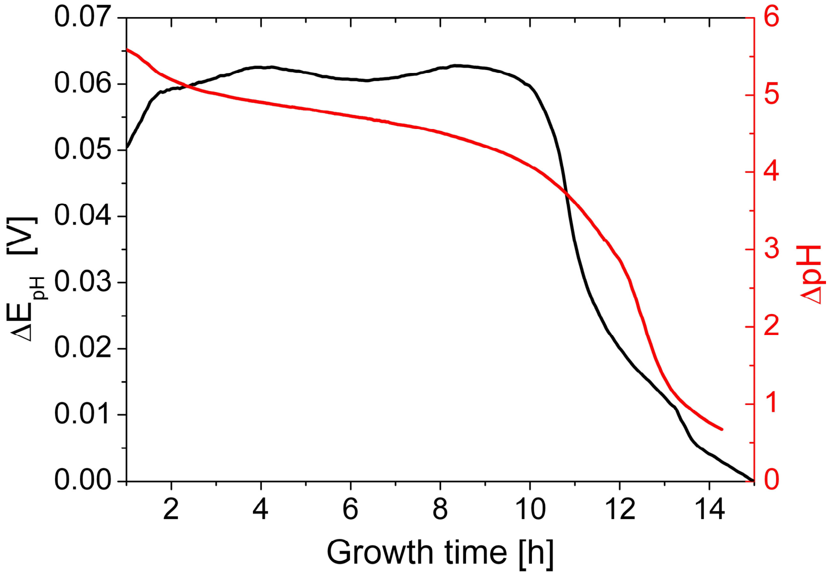

Fig. 69: Comparison of the time-dependent progressions of ΔE_{pH} (calculated by subtracting the sum of membrane and diffusion potential from the measured overall cell potential) and ΔpH (derived from experimental data presented in Fig. 67 and Fig. 68A) in Co^{2+}-based silica gardens.

Comparison of ΔE_{pH} progressions thus obtained with the temporal evolution of ΔpH between the inner and outer solution (Fig. 69) shows indeed good qualitative correlation within the first 15 h and hence corroborates the existence of pH-induced potential differences in the system according to one of the both models presented above. However, from the data presented in this work, no final position can be taken, which of the two presented models for a pH-induced potential applies in the end.

5.2.4. Conclusions

In conclusion, the observed evolution of the overall potential difference (ΔE_h) across the precipitated tube walls was found to be explainable by an interplay of diffusion (ΔE_{diff}) and membrane (ΔE_m) potentials, in combination with a pH-induced potential (ΔE_{pH}) which is either caused by a redox potential or by an additional membrane potential, originating from high gradients in proton and hydroxide concentrations:

$$\Delta E_h = \Delta E_{diff} + \Delta E_m + \Delta E_{pH} \tag{40}$$

In this case, the observed potential curves can be interpreted as follows (cf. Fig. 70):

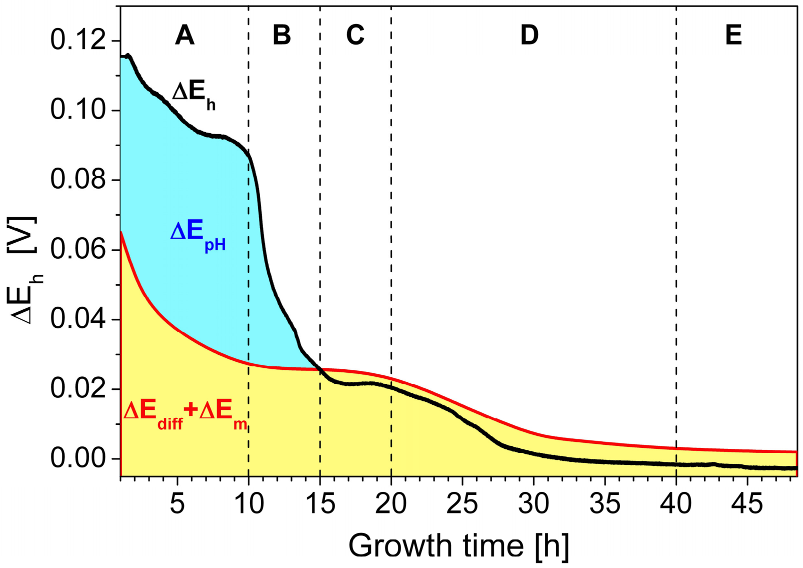

Fig. 70: (A-E) Stages of ΔE_h evolution as a combination of diffusion (ΔE_{diff}), membrane (ΔE_m) and pH induced (ΔE_{pH}) potentials.

(A) Unhindered but slow counter diffusion of inner chloride and outer sodium ions leads to diminishing concentration gradients and thus to smaller values for the diffusion and membrane potential at the beginning of silicate garden evolution. In parallel, the effective permeability of the tube wall for hydroxide ions is very low, as penetrating OH^- ions precipitate with free multivalent metal ions on the interior surface of the tubes. Therefore, the gradient in pH is only slightly diminished by removal of the dissolved and acidic iron/cobalt ions due to precipitation.

(B) At the point of complete elimination of the dissolved iron/cobalt ions, permeability of the tube wall to hydroxide ions rapidly increases and in-diffusion of OH^- into the tube interior not only eliminates pH gradients but also the pH induced potential (ΔE_{pH}) within a few hours (visible as distinct dropping down of ΔE_h after 10-15 h).

(C) Subsequently, the cell potential ends up at nearly constant values which comply well with the sum of altered membrane and diffusion potentials.

(D) When the interior pH has finally reached sufficiently alkaline values, no more silica is deposited on the outer skin of the tube walls and the permeability to silicate ions also becomes significantly elevated. Consequently, in-diffusion of silicate ions leads to ongoing changes in the observed diffusion and membrane potentials, clearly visible in a second distinct step in the progressions of the potential differences. Delayed recording of silicate in-diffusion can also be explained by the sixfold lower ion mobility of $H_3SiO_4^-$, compared to OH^- (cf. Tab. 9).

(E) With completion of diffusion processes and resulting equilibration of all ion concentrations in both compartments, remaining cell potentials finally become completely eliminated.

Comparison of the potential curves recorded either with two identical Pt or Ag/AgCl electrodes further reveals that the evolution of the cell potential is generally independent of the employed electrodes and proceeds in several distinct steps (cf. Fig. 64). This is clear affirmation that the precipitated walls of silicate garden tubes can indeed be regarded as a combination of a time-dependent membrane and a diaphragm. However, it is also visible that the characteristics of the individual steps is less pronounced when Ag/AgCl electrodes were applied, indicating that the detailed progression of the cell potential also depends on the used sort of electrode material, which can be more sensible to one or several sorts of ions (e.g. protons or chloride ions).

Finally, it can be stated that experimental data fit well to the established hybrid model of a membrane/diaphragm tube wall, although several parameter had to be estimated (e.g. the estimation of explicite values for the relative permeabilities of all ion species as well as their changes during the evolution of silicate garden growth).

Results of the performed experiments could furthermore demonstrate that, though starting from easily understandable and simple basic materials, growth of the examined silicate garden systems turned out to be of a quite complex nature, involving several processes which occur in parallel as well as in subsequent steps after different periods.

6. Time-Resolved XRD Measurements

6.1. Identification of Crystalline Material

Measurements on both XRD beamlines (EDXRD beamline F3 at *Doris III, DESY* and XRD1 beamline at *Eletta*) revealed the formation of crystalline material in the course of silicate garden growth, when using the metal salts listed in Tab. 2 (section III.1) with the exception of cobalt(II) iodide. Besides their necessary ability to form macroscopic silicate garden tubes within a short preparation period, selected metal salts were also chosen to provide a variation of the metal as well as of the counter ion and thus to allow the drawing of utilizable conclusions on the influence of both ion types on the resulting crystallinity of the precipitated membranes.

As the experimental procedures for the XRD measurements performed at both synchrotron facilities significantly differ from each other, the dimensions and the growth rate of the resulting silicate gardens also exhibit large differences (cf. Fig. 35 and Fig. 37). From these deviations, one might expect the crystallization of different material in both XRD experiments. Therefore, it is worth to mention that these alterations in the setup did not affect the quality of crystallization, thus leading to the formation of the same crystalline materials.

However, signal to noise ratios were quite poor for the EDXRD measurements at beamline F3, thus complicating background subtraction and assignment of reflexes to known references.

On this account, only the diffractograms with the best performance from both XRD experiments are presented in the following, together with reflexes of the corresponding reference materials taken from the Stoe WinXPow reference library.

6.1.1. Crystallinity of Silicate Gardens Prepared from Co(II) Salts

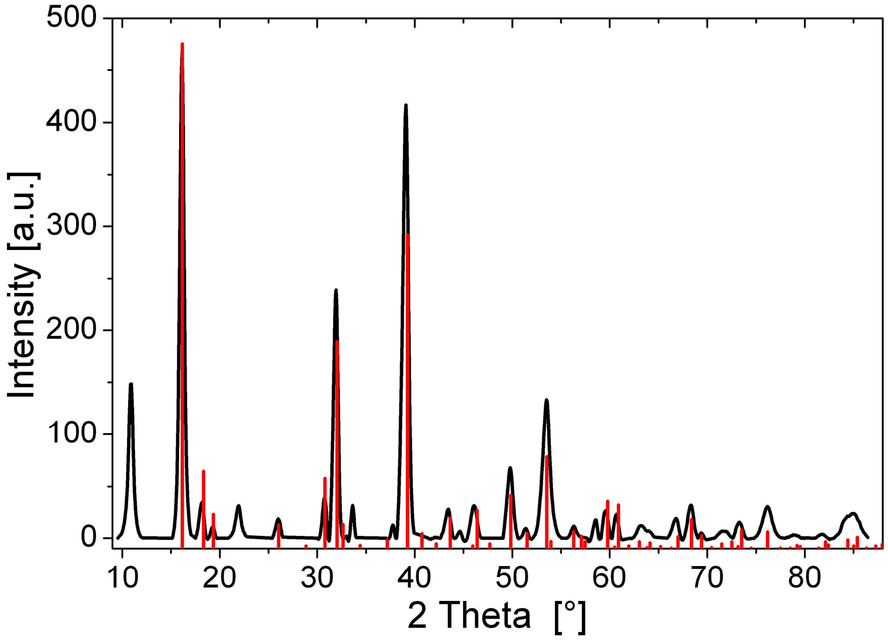

Fig. 71: Crystallization of $Co_2(OH)_3Cl$ in capillary grown silicate gardens prepared from a $CoCl_2$ crystal.

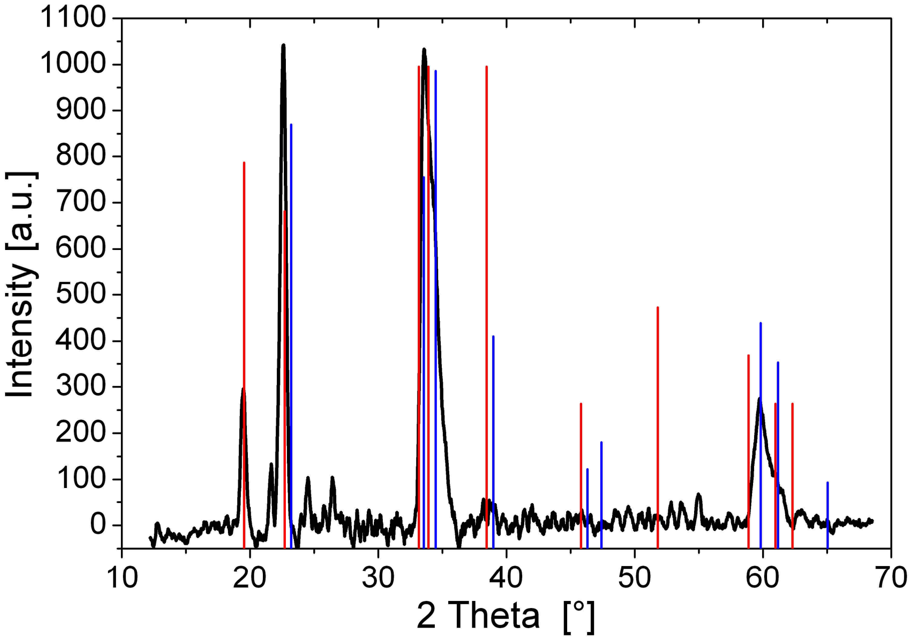

Fig. 72: Crystallization of $Co(OH)_2$ (red) and $Co_5(O_{9.48}H_{8.52})NO_3$ (blue) in macroscopic silicate gardens with open-tube growth prepared from a $Co(NO_3)_2$ pellet.

Use of both cobalt(II) salts ($CoCl_2$ and $Co(NO_3)_2$) leads to the formation of crystalline fractions in the precipitating silicate garden tubes. When $CoCl_2$ was used for silicate garden growth, the resulting crystalline phase corresponds to cobalt hydroxide chloride, $Co_2(OH)_3Cl$ (see Fig. 71).

In contrast, crystallization of a mixture of $Co_5(O_{9.48}H_{8.52})NO_3$ (blue) and $Co(OH)_2$ (red) was observed for silicate gardens prepared from $Co(NO_3)_2$ (see Fig. 72).

6.1.2. Crystallinity of Silicate Gardens Prepared from Fe(II) Salts

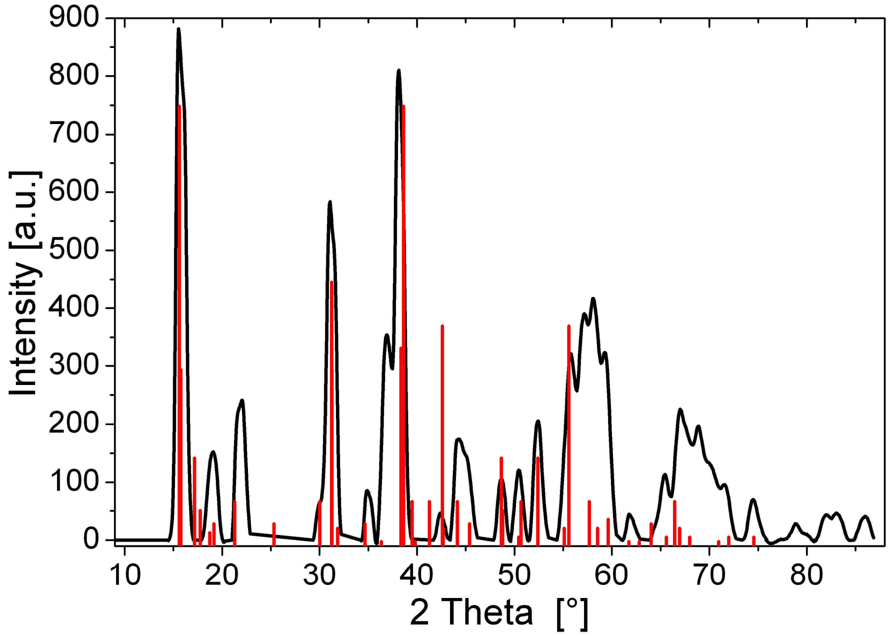

Fig. 73: Crystallization of $Fe_2(OH)_3Cl$ in capillary grown silicate gardens prepared from a $FeCl_2$ crystal.

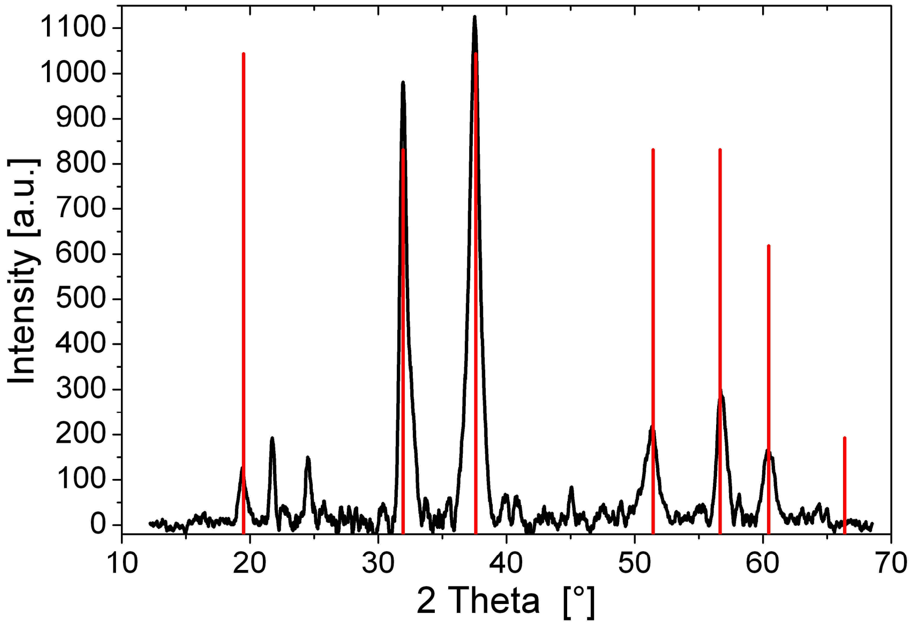

Fig. 74: Crystallization of $Fe(OH)_2$ in macroscopic silicate gardens with open-tube growth prepared from a $FeSO_4$ pellet; additional reflexes indicate the presence of a second crystalline phase.

$FeCl_2$ and $FeSO_4$ were used as iron(II) salts for silicate garden preparation. In the former case, crystallization of $Fe_2(OH)_3Cl$ was observed (see Fig. 73), while in the latter case $Fe(OH)_2$ crystallites form in the membrane material (see Fig. 74).

Possibly, small fractions of a second crystalline substance are present in the $FeSO_4$ based silicate garden system, as additional weak reflexes appear in the diffractogram. However, assignment of these weak reflexes to a certain reference was not successful.

6.1.3. Crystallinity of Silicate Gardens Prepared from Fe(III) Salts

Three different Fe(III) silicate gardens were analyzed on their crystallinity, using $FeCl_3$, $Fe(NO_3)_3$ and $Fe_2(SO_4)_3$ as crystalline starting material. In general, silicate gardens prepared with Fe(III) salts grew with a higher rate compared to Fe(II) and Co(II) salts.

Crystalline material was only detectable when $FeCl_3$ was used for preparation (Fig. 75), while the latter two precipitates remained completely amorphous (diffractograms not shown).

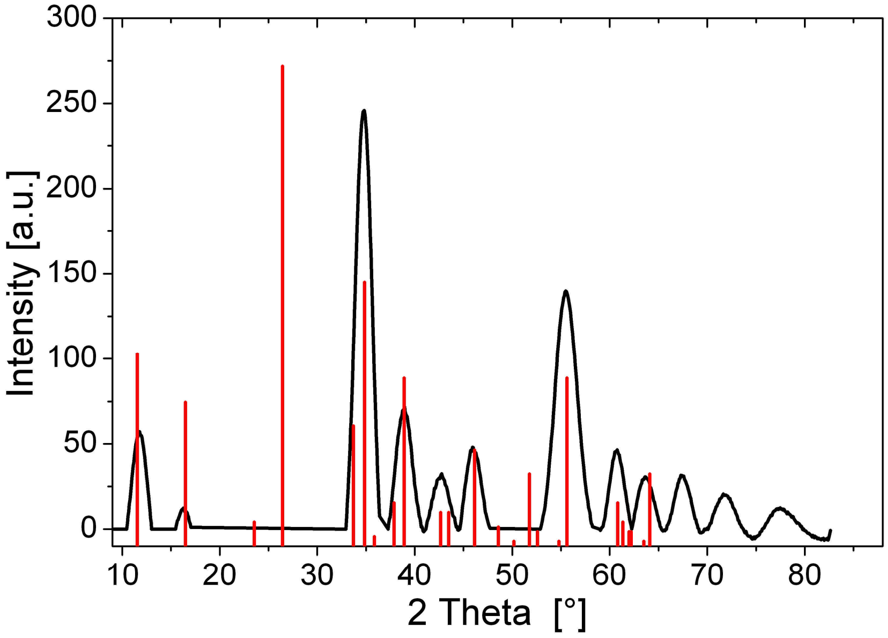

Fig. 75: Crystallization of FeO(OH) (Akaganeite-M) in capillary grown silicate gardens prepared from a $FeCl_3$ crystal.

6.2. Time-resolved EDXRD Experiments at Beamline F3 (*Doris III, DESY*)

Crystallization processes in macroscopic silicate gardens (typical dimensions: d ≈ 3-5 mm; h ≤ 30 mm; cf. section III.3.6) were examined at beamline F3. Although the experimental setup theoretically allowed the collection of time-resolved diffractogram series, the recording of progressions in crystallinity turned out to be quite difficult. One of the two mayor obstacles within the performance of the XRD measurements can be found in the beam size which was limited to a very small area (max. 300x300 µm²), thus reducing the probability to hit crystalline matter incorporated in the membrane. A second reason for the frequent failures to record a series of good diffractograms lies in the positioning of the tubular membrane wall, which must be exactly in the intersection point where the virtually prolonged detector arm meets the incident X-ray beam (cf. Fig. 37). As soon as the membrane is positioned out of focus, no crystalline matter can be detected.

Altogether, relevant data on the onset of crystallization were only obtained for a $CoCl_2$ based silicate garden within the first two hours of growth (Fig. 76), while in all other cases, time-resolved tracing of crystalline fractions was limited to several isolated diffractograms. Consequently, no evolution of crystallization processes could be followed.

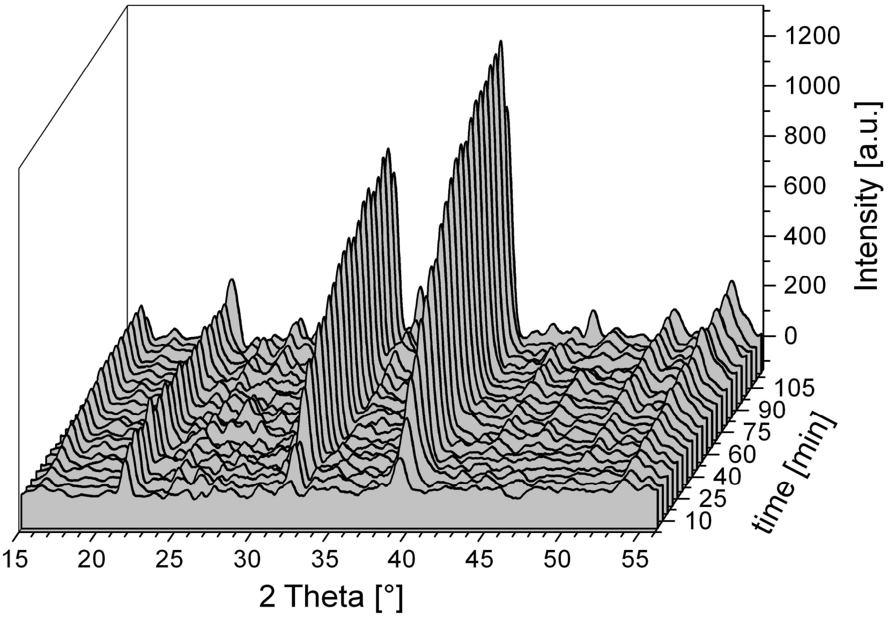

Fig. 76: 3D plot of diffractograms vs. growth time showing the progressive crystallization of $Co_2(OH)_3Cl$ in open-tube silicate gardens prepared from a $CoCl_2$ pellet.

Diffractograms in Fig. 76 show the crystallization of $Co_2(OH)_3Cl$ within the first 120 min of garden growth. It is clearly visible that the amount of crystalline matter increases significantly within the progress of tube evolution. A more quantitative analysis on the evolution of crystallization can be done by plotting the averaged integrals of the strongest reflexes versus the growth time, giving the results displayed in Fig. 77. Obviously, the degree of crystallization evolves in a characteristic manner and can sufficiently be described by a fitting curve (red line) according to a kinetic model which will be presented in section IV.7.2.

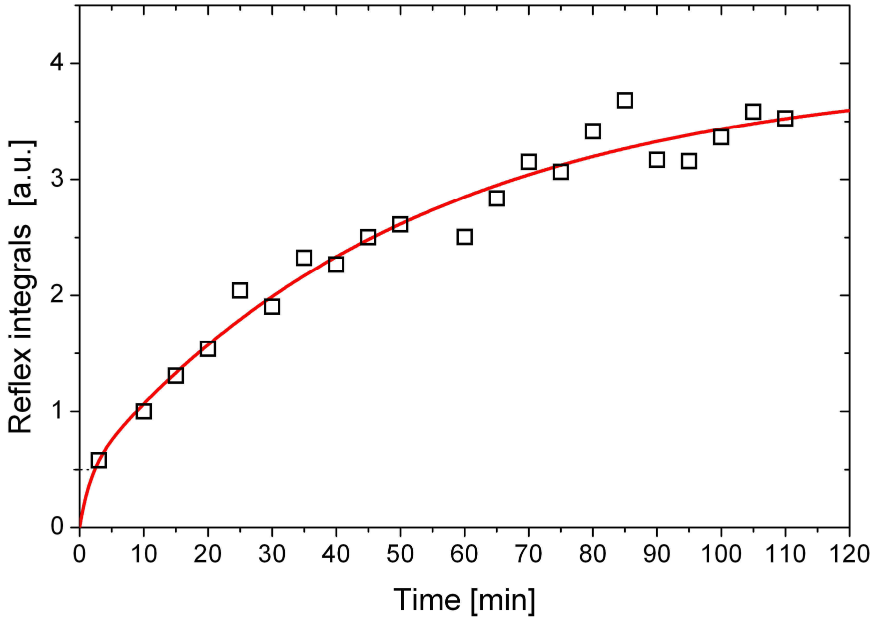

Fig. 77: Time-resolved Evolution of averaged relative reflex integrals derived from the diffractograms of $Co_2(OH)_3Cl$ crystallization given in Fig. 76. Red line correlates to a fit model, explained in section IV.7.2.

6.3. Results from XRD Measurements on Beamline XRD1 (*Elettra*)

In contrast to the more or less sparse results derived from time-resolved experiments at the EDXRD beamline F3, XRD measurements performed at the *Elettra* beamline XRD1 on miniaturized silicate gardens (cf. section III.3.7.1) appeared to be more promising. Successful collection of 2D-diffractogram series for the three examined silicate garden types based on $FeCl_3 \cdot 6H_2O$, $FeCl_2 \cdot 4H_2O$ and $CoCl_2 \cdot 6H_2O$ results in the 3D plots presented in Fig. 78.

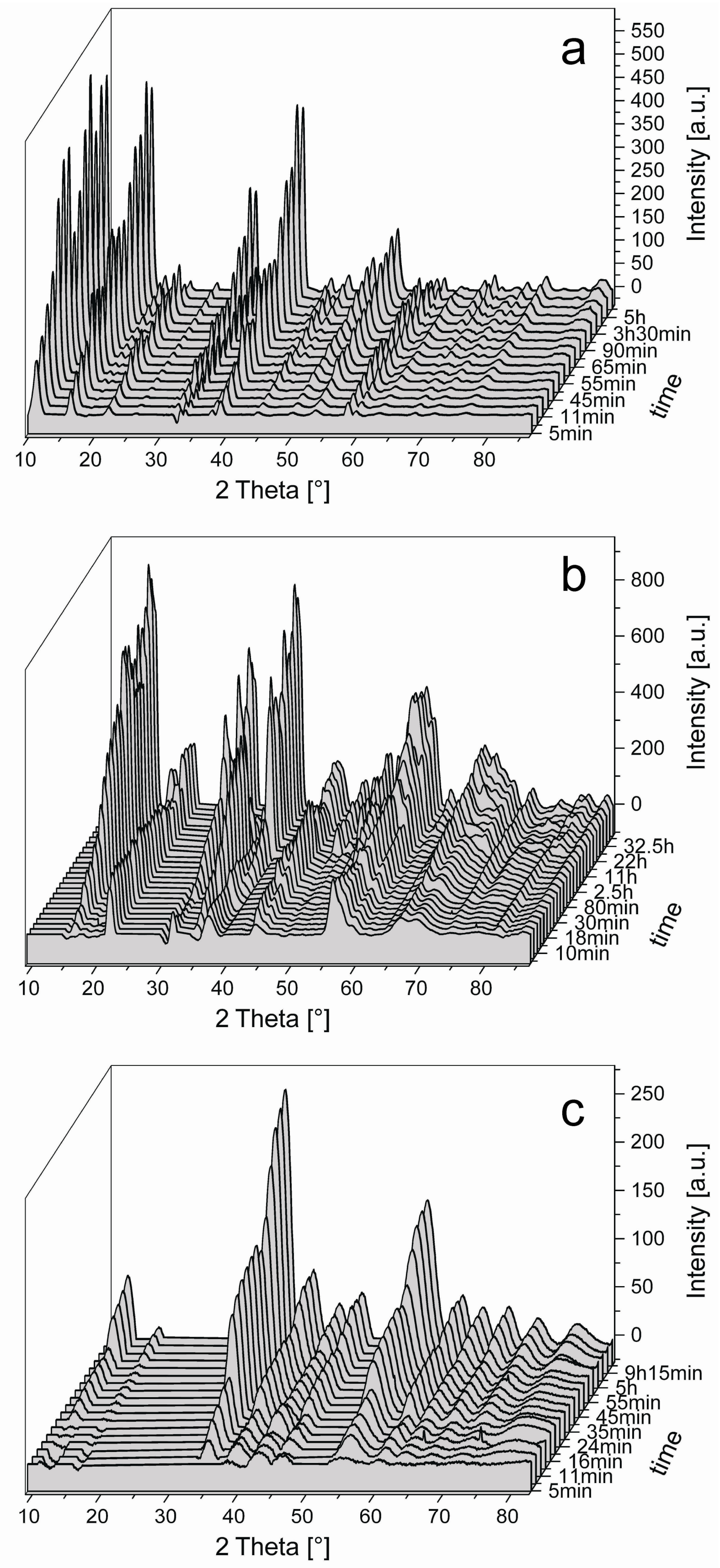

Fig. 78: 3D plots of diffractograms versus growth time showing the progressive crystallization of (a) $Co_2(OH)_3Cl$, (b) $Fe_2(OH)_3Cl$ and (c) FeO(OH) in silicate gardens prepared in capillaries from $CoCl_2$, $FeCl_2$ and $FeCl_3$ crystals, respectively.

In all three systems, crystallization of (a) $Co_2(OH)_3Cl$, (b) $Fe_2(OH)_3Cl$ and (c) FeO(OH) starts right from the beginning of tube formation and continues within periods of several hours, clearly visible by increase in reflex intensities.

As measurements were not performed in equidistant intervals, a continuous increase of the reflex intensities is in some cases not easily recognizable. Therefore, a quantitative analysis on the course of the crystallization processes will be presented in the next section, focusing on the kinetics of silicate garden growth.

7. Observations on the Kinetics of Silicate Garden Evolution

In this section, new and already presented results obtained from time-resolved measurements on the evolution of metal ion concentrations and crystallization processes will be used for the establishment of a suitable kinetic model, sufficiently describing ongoing dissolution, precipitation and crystallization processes occurring during silicate garden evolution. Therefore, in the first part, detailed results will be presented on the evolution of the interior metal ion concentrations (Co^{2+}, Fe^{2+}, Fe^{3+}) to allow the analysis of the kinetics of metal salt dissolution and subsequent precipitation of metal silicates and hydroxides. In a second subsection, results from time-resolved XRD measurements (cf. section IV.6.3) will be analyzed to allow the establishment of a kinetic model for the observed crystallization processes.

7.1. Kinetics of Dissolution and Precipitation Processes

In order to shed light on the kinetics of metal ion incorporation to the forming membranes, interior solutions of silica gardens based on $CoCl_2$, $FeCl_2$ and $FeCl_3$ were analyzed on their metal ion contents after different periods independently by means of atomic emission (AES) and X-ray absorption (XAS) spectroscopy, to assure reliability of the results. (For details on silicate garden preparation and analysis by AES and XAS see sections III.2.1, III.3.2 and III.3.3).

Measured values for the metal ion concentrations obtained by both methods are shown in Fig. 79, together with the fitting curves (red lines) calculated by assuming the kinetics of an underlying irreversible consecutive reaction which will be discussed at the end of this section.

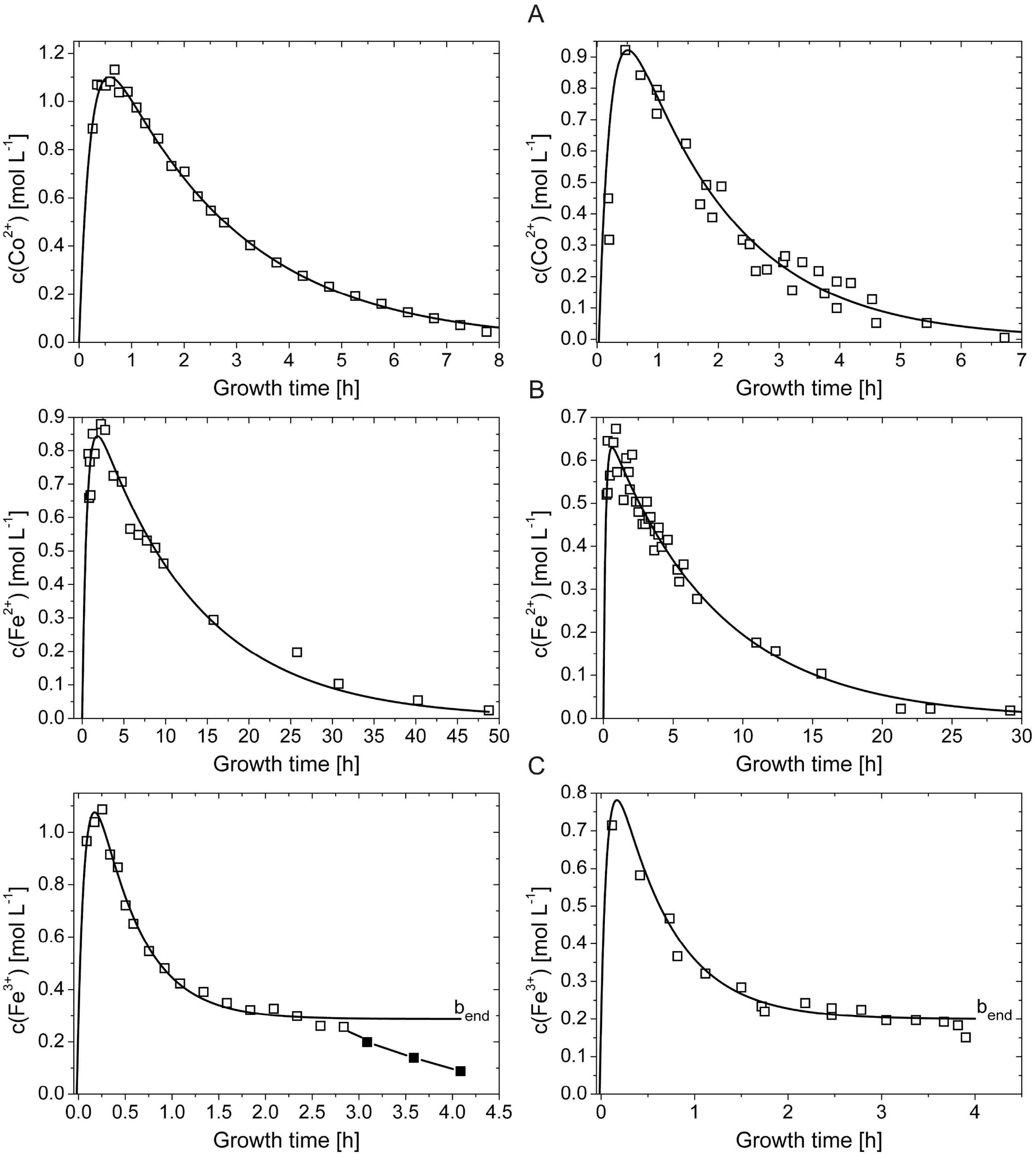

Fig. 79: Measured cobalt and iron ion concentrations (squares) as a function of time inside the tubes of silica gardens prepared with pellets of (A) $CoCl_2$, (B) $FeCl_2$ and (C) $FeCl_3$, as determined by AES (left) and XAS (right). Full squares indicate samples taken after solidification of the interior solution had commenced. Full lines represent fitting curves calculated on the kinetics of an irreversible consecutive reaction.

It is obvious that both techniques yielded comparable concentration profiles, similar to those described in section IV.3 (cf. Fig. 54). In all cases, a characteristic initial increase was observed which was followed by an exponential decrease. As already observed in section IV.3, concentration progressions obtained for silica gardens based on $FeCl_3$ differ from the other two systems in that the metal ion concentration does not decrease continuously to zero, but levels off at values around 0.2-0.3 M (Fig. 79C), owing to solidification of the interior solution. Observed similarities in the progressions of the metal ion concentrations, independent of the used technique, are clear evidence that the results describe a general effect which can be sufficiently described by one kinetic model. Differences between the results of the two techniques may be attributed to the limited reproducibility of preparation even with the improved procedure applied in the present work, or to the fact that growth was carried out at slightly higher temperatures (~ 25°C) in the case of the XAS experiments than otherwise throughout this study (20°C).

In a first approach, the found general evolution of metal ion concentrations with time in the interior solutions of the analyzed silica gardens can be rationalized when considering the ongoing processes as an irreversible consecutive reaction (Fig. 80). Starting from a solid pellet (A), dissolution of the metal salt first leads to an increase in concentration of free metal ions in the solution (B). Subsequently, released metal ions are eliminated by precipitation of hydrous metal hydroxides and silicates (C).

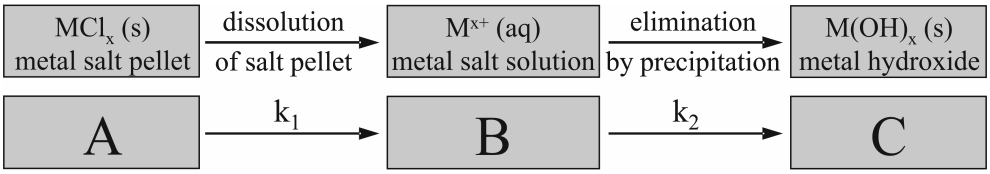

Fig. 80: Kinetic model for the generation and consumption of divalent metal ions in the interior solutions of open-tube silica gardens.

Consequently, the temporal progression of the metal ion concentration b(t) in the inner solution should comply with the following kinetic equation:[106]

$$b(t) = a_0 \cdot \frac{k_1}{k_2 - k_1} \cdot \left[e^{-k_1 \cdot (t+t_0)} - e^{-k_2 \cdot (t+t_0)} \right] \tag{41}$$

where a_0 is the total analytical concentration of the metal ions and t_0 represents the period of preparation until first sampling. In the case of $FeCl_3$, the kinetic equation had to be extended by a further term accounting for the significant deviation from zero of the final metal ion concentration b_{end} due to solidification, according to

$$b(t) = b_{end} + a_0 \cdot \frac{k_1}{k_2 - k_1} \cdot \left[e^{-k_1 \cdot (t+t_0)} - e^{-k_2 \cdot (t+t_0)} \right] \tag{42}$$

As visible from Fig. 79, fitting of the obtained experimental data with the above equations indeed shows good correlation for all investigated silica garden systems. The obtained fit parameters are compiled in Tab. 12. Calculating the rate constants of the involved reactions yields consistent results from both techniques (AES and XAS) used, with values in the range of $4.8{\cdot}10^{-4}$-$1.8{\cdot}10^{-3}$ s^{-1} and $2.3{\cdot}10^{-5}$-$4.0{\cdot}10^{-3}$ s^{-1} for k_1 and k_2, respectively. Apparently, precipitation of dissolved metal ions into the forming membrane material is the overall rate-determining step in silica gardens prepared with $CoCl_2$ and $FeCl_2$ (k_1>k_2). By contrast, precipitation of metal hydroxides and/or silicates is delimited by the rate of pellet dissolution in systems based on $FeCl_3$ (k_1<k_2). This discrepancy can be explained by the dramatically lower solubility of $Fe(OH)_3$ in aqueous solutions as compared to $Fe(OH)_2$ and $Co(OH)_2$ (cf. Tab. 8), causing extremely rapid elimination of Fe^{3+} ions from the interior solution which cannot be sustained adequately by dissolution.

Metal salt	**t_0 [min]**	**k_1 [s^{-1}]**	**k_2 [s^{-1}]**	**b_{end} [mol L^{-1}]**	**a_0 [mol L^{-1}]**	**R**
$CoCl_2$	16	$(1.28 \pm 0.17){\cdot}10^{-3}$	$(1.12 \pm 0.03){\cdot}10^{-4}$	0	1.39 ± 0.03	0.997
	13	$(1.43 \pm 1.13){\cdot}10^{-3}$	$(1.63 \pm 0.21){\cdot}10^{-4}$	0	1.22 ± 0.14	0.909
$FeCl_2$	45	$(4.91 \pm 2.71){\cdot}10^{-4}$	$(2.25 \pm 0.26){\cdot}10^{-5}$	0	0.98 ± 0.06	0.965
	15	$(1.79 \pm 0.22){\cdot}10^{-3}$	$(3.54 \pm 0.23){\cdot}10^{-5}$	0	0.68 ± 0.02	0.964
$FeCl_3$	5	$(6.04 \pm 0.80){\cdot}10^{-4}$	$(3.37 \pm 1.29){\cdot}10^{-3}$	0.29 ± 0.02	1.15 ± 0.10	0.991
	5	$(4.76 \pm 1.38){\cdot}10^{-4}$	$(3.97 \pm 37.67){\cdot}10^{-3}$	0.20 ± 0.01	6.48 ± 56.13	0.969

Tab. 12: Kinetic parameters obtained by fitting experimental data from AES (white) and XAS (highlighted) analyses in the framework of a model of an irreversible consecutive reaction.

7.2. Kinetics of Crystallization Processes

In this section, results from quantitative analyses of the data obtained from time-resolved XRD measurements on miniaturized silicate gardens (section IV.6.3) will be presented.

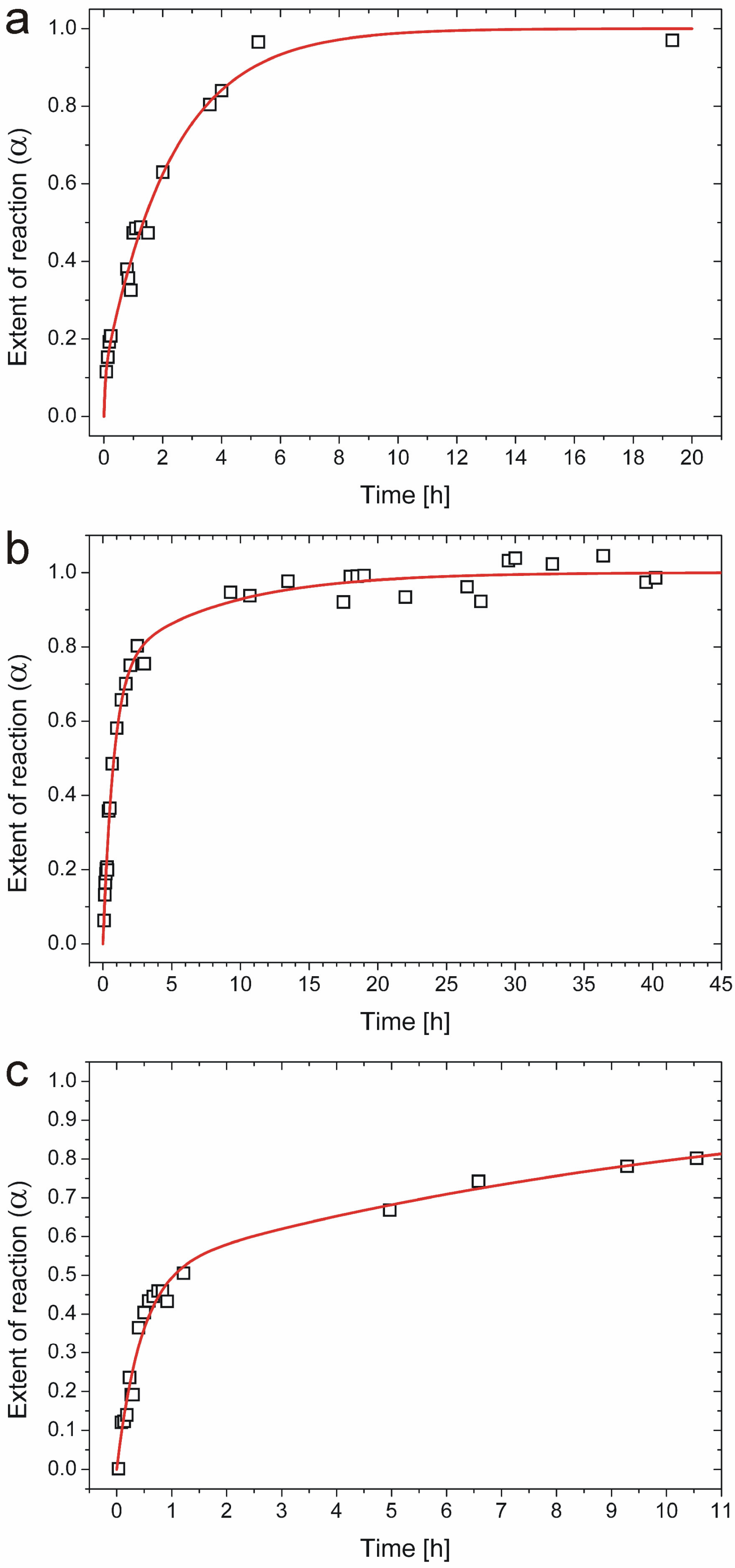

Fig. 81: Time-resolved evolution of the reaction progress (α) of (a) $Co_2(OH)_3Cl$, (b) $Fe_2(OH)_3Cl$ and (c) FeO(OH) crystallization in silica gardens prepared from (a) $CoCl_2$, (b) $FeCl_2$ and (c) $FeCl_3$ seed crystals in a capillary system.

As it is already visible from Fig. 78, crystallinity of the examined silicate gardens increases with proceeding growth. The relative amount of crystalline material can be obtained from the respective peak integrals of the diffractograms. Therefore, the values of the peak integrals directly correlate with the extent of the crystallization reaction (α). Assuming a final reaction progress of $\alpha = 1$ at infinite growth times, the kinetics of crystallization processes should be accessible from plotting α against growth time by the use of a suitable kinetic model. Following this procedure, time-resolved evolutions of the reaction progresses (α) for the crystallization of (a) $Co_2(OH)_3Cl$, (b) $Fe_2(OH)_3Cl$ and (c) $FeO(OH)$ in miniaturized silicate gardens prepared from tiny crystals of $CoCl_2$, $FeCl_2$ and $FeCl_3$ are obtained, given in Fig. 81. Red lines represent fitting curves and were calculated from experimental data by using a kinetic model which is presented in the following.

As metal oxide hydroxides (from $FeCl_3$) or metal hydroxide chlorides (from $FeCl_2$ and $CoCl_2$) may crystallize either by transformation of precipitated amorphous material (C) or directly from solution, requiring dissolved metal ions (B), the following refined reaction model can be established (Fig. 82):

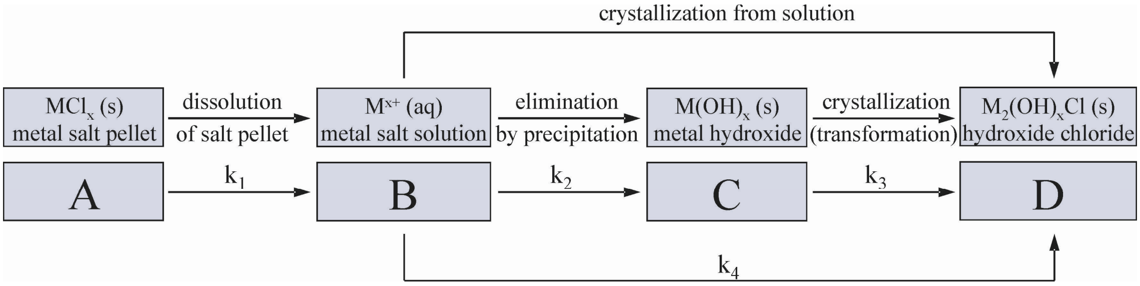

Fig. 82: Extended kinetic model for the dissolution, precipitation and crystallization reactions occurring during the evolution of silicate garden growth.

This model represents an extended and advanced version of the first approach made in the previous section (cf. Fig. 80) for the evolution of the metal ion concentrations, now including possible crystallization processes (D).

Before fitting the experimental XRD data of the miniaturized silicate gardens to the proposed model for the crystallization kinetics, the following assumptions were taken into account:

- Total dissolution of the metal salt crystal took place before first measurements were performed ($t_0 < 3$ min); the first reaction step ($A \rightarrow B$) is therefore accomplished and a concentration of b_0 at t_0 exists inside the precipitated membrane
- Compared to the amount of metal salt, a high excess in water glass is present in the capillary; consequently, the concentrations in hydroxide and silicate ions can be regarded as constant

For the evolution of the crystallization processes, the resulting kinetic equations for the temporal concentrations in B, C and D are given as:

$$b(t) = b_{t_0} \cdot e^{-(k_2+k_4)\cdot t}, \tag{43}$$

$$c(t) = b_{t_0} \cdot \frac{k_2}{k_3 - (k_2 + k_4)} \cdot \left[e^{-(k_2+k_4)\cdot t} - e^{-k_3 \cdot t} \right] \text{ and} \tag{44}$$

$$d(t) = b_{t_0} \cdot \left[1 - e^{-(k_2+k_4)\cdot t} - \frac{k_2}{k_3 - (k_2 + k_4)} \cdot \left(e^{-(k_2+k_4)\cdot t} - e^{-k_3 \cdot t} \right) \right]. \tag{45}$$

Apparently, experimental values for the crystallization progress fit well to the proposed kinetic model, giving the fitting curves (red lines) presented in Fig. 81. However, it is worth to mention that each type of silicate garden was examined only once so that, especially in the case of $CoCl_2$ (Fig. 81a) and $FeCl_3$ (Fig. 81c) based gardens, the number of collected diffractograms is limited. The herein presented results thus only represent a first feasibility study without the aim of completeness. Kinetic parameters obtained from fitting the data to the proposed kinetic model are listed in Tab. 13.

Metal salt	**k_2 [s^{-1}]**	**k_3 [s^{-1}]**	**k_4 [s^{-1}]**	**$t_{\alpha=0.5}$ [min]**
$CoCl_2$	$(4.7 \pm 7.1)\cdot 10^{-3}$	$(1.2 \pm 0.2)\cdot 10^{-4}$	$(7.2 \pm 7.5)\cdot 10^{-4}$	80
$FeCl_2$	$(8.3 \pm 2.4)\cdot 10^{-5}$	$(3.6 \pm 1.4)\cdot 10^{-5}$	$(2.7 \pm 0.2)\cdot 10^{-4}$	48
$FeCl_3$	$(2.9 \pm 1.3)\cdot 10^{-4}$	$(2.5 \pm 4.1)\cdot 10^{-5}$	$(3.2 \pm 1.8)\cdot 10^{-4}$	63

Tab. 13: Kinetic parameters obtained by fitting experimental data from XRD measurements to the established kinetic model of silicate garden growth.

Due to the realistic assumption of completed crystal dissolution prior to the performance of the first diffraction measurements, the rate constant k_1 was not determinable. From Tab. 13 it can be recognized that for the three observed silicate garden systems the reaction rate k_4 possess a higher value than the rate constant k_3. This indicates that direct crystallization from solution (B → D) is favoured to transformation of amorphous material to crystalline matter (C → D).

Apart from this congruency, especially the reaction progress curve for the crystallization of FeOOH in the $FeCl_3$-silicate system exhibits a remarkable variation to the other two examined systems; while in the latter two systems α rapidly increases to values above 0.8 within 3-4 h, the extent of FeOOH crystallization reaches only values around $\alpha \approx 0.5$ within ~90 min, followed by a significantly slower increase up to values around $\alpha \approx 0.8$ after more than 10 h. Comparison of the rate constant values for k_2 derived from the present XRD measurements and from AES and XAS measurements on the metal ion concentrations (cf. section IV.7.1) further reveals significant deviations by factors ranging from 0.1-42.

Obviously, a quantitative comparison of the kinetics of microscopic and macroscopic silicate garden growth is not possible. Reasons for the deviations in the kinetics might be found in the different sizes of the resulting silicate gardens prepared by the two independent preparation routines described in section III.2.1 and III.3.7.1.

Decelerated crystallization in the $FeCl_3$-silicate system might be explainable by the higher acidity of the Fe^{3+}, significantly lowering the pH of the interior solution. As hydroxide precipitation occurs at an elevated pH in the basic range, crystallization might thus be temporarily slowed down until sufficiently basic conditions came about in the interior of the tubular membranes.

V. Summary and Conclusions

1. Realized Experiments

In the present work, an advanced procedure for the preparation of silica gardens was developed, which relies on the use of pressed metal salt tablets instead of irregular crystals as well as slow and controlled addition of dilute water glass. Based thereupon, tubular structures having an open end to the atmosphere were grown with improved and satisfactory reproducibility using a series of different Co(II), Fe(II) and Fe(III) salts (cf. Tab. 2 in section III.1). With this open-tube setup, both the outer silica-rich reservoir and the metal salt solution enclosed by the formed membrane were easily accessible for a series of *in-situ* analysis techniques (section III.2).

By immersion of different types of pH and metal electrodes into the aqueous solutions of both compartments, the presence and evolution of long-lasting gradients in pH and electrochemical potentials across the precipitated tubular membrane were recorded within periods up to ~48 hours (sections III.3.4 and III.3.5).

The established open-tube growth of silicate gardens further allowed for continuous sampling of the solutions in the two compartments by use of pipettes or precision capillaries. By means of AES and XAS spectroscopy, concentrations of the various ionic species present during formation on both sides of the membrane were determined at different times over periods of up to days (sections III.3.2 and III.3.3).

Silicate gardens were also examined on their crystallinity. Therefore, time-resolved XRD measurements were performed at the two beamlines F3 (*DORIS III, DESY*) and XRD1 (*Elettra*) to obtain information about the kinetics of eventually occurring crystallization processes (section III.3.7).

Further, silicate gardens with open-tube growth were also isolated after growth, and extracted membrane fragments were analyzed on their chemical and structural composition by means of XRD, SEM and EDX techniques (sections III.3.1 and III.3.6).

2. Elimination of Chemical and Electrochemical Gradients by Precipitation and Diffusion Processes

By using the described *in-situ* techniques, significant gradients in pH, electrochemical potential and ion concentrations were found across the precipitated membranes in all studied silicate gardens (sections IV.3 - IV.5).

The recorded temporal concentration, potential and pH profiles show overall uniform trends for all examined systems, indicating that generally the same processes occur regardless of the chosen metal salt. Variations in the detailed progressions of the diverse parameters arise due to slight differences in the preparation procedure, limited control over the shape of a growing tube, as well as the distinct chemical behavior of the particular metal salt used.

2.1. Equilibration of pH and Ion Concentrations

Results from pH, AES and XAS measurements indicate that existing pH and ion concentration gradients are eliminated by a combination of precipitation and diffusion processes. It was further found that the sort of elimination mechanism is determined by the nature of the respective ion (sections IV.3 and IV.4):

- **Precipitation Processes**

  A combination of metal salt pellet dissolution and subsequent precipitation into the wall of the tube determines the time-dependent evolution of the interior metal ion concentrations. While the former process leads to an initial rapid increase of the measured Fe^{2+}, Co^{2+} and Fe^{3+} concentrations, the latter process causes a quasi-exponential decrease down to values below the detection limit in the case of Fe^{2+} and Co^{2+}, or to final concentrations around 0.2-0.3 M in Fe^{3+}-based systems, where complete solidification of the interior solution was observed. Elimination of multivalent metal ions by precipitation was not only traced by AES measurements but is also reflected by the temporal course of pH in the interior solution, which resembles the titration curve of a weak to medium-strong acid (metal cations) by a strong base (hydroxide ions penetrating the wall from the outside). From that, it can be deduced that metal ions are continuously incorporated to the inner surface of the membrane predominantly by precipitation of metal hydroxides (for $CoCl_2$ and $FeCl_2$ based systems) or hydroxide oxides (in the $FeCl_3$-silicate system).

- **Combination of Precipitation and Delayed Diffusion**

  In contrast to the concentration gradient in multivalent metal ions, which is exclusively eliminated by precipitation, a combination of precipitation and delayed diffusion processes is responsible for the observed equilibration of silicate and hydroxide ion concentrations in both compartments of the chemical garden systems.

  In the case of hydroxide ions, precipitation with the multivalent metal cations initially arrests transport of OH^- ions at the interior surface of the membrane. As soon as all cations are removed, unhindered diffusion is permitted and the concentration of hydroxide ions, and hence the pH, gradually become equilibrated on both sides of the membrane.

  Similar conclusions can be drawn for the diffusion of silicate ions through the wall. The concentration of dissolved silica inside the tube was found to be negligible as long as the pH of the interior solution is still acidic or near-neutral. However, once sufficiently alkaline conditions are established by in-diffusion of hydroxide ions, diffusion of silicate species sets in and their inner concentration increases to finally adopt values close to those in the outer reservoir. Regarding the dramatic changes of silica solubility with pH in the concerned regime, it is evident that diffusion of silicate ions is fundamentally possible from the very beginning on, but at first blocked by the low pH of the interior solution. As a consequence, silicate species trying to penetrate the wall will precipitate on its outer surface during the earlier stages, thus leading to the previously reported silica-rich deposits on the exterior side of the membrane.[17]

- **Unhindered Ion Diffusion**

  By tracing the concentration of sodium (introduced with the outer silica sol) and the detectable metal salt counter ion iodide (stemming from the inner metal salt pellet in the case of CoI_2) in the solutions on either side of the membrane walls, it was demonstrated that such simple ions can readily diffuse through the membrane separating the two volumes. Diffusion of Na^+ and I^- commences right from the beginning of membrane formation and proceeds over extended frames of time until their concentrations are eventually equal in both solutions and thermodynamic equilibrium is reached.

Mass balance considerations moreover suggest that iodide ions are not co-precipitated with the metal cations to a noticeable extent, supporting the notion that the interior surface of the walls mainly consists of metal hydroxide.

2.2. Elimination of Electrochemical Cell Potentials

From the recorded gradients in pH and ion concentrations across the tube wall it was concluded that also significant gradients in the electrochemical potentials of both compartments must exist, which were indeed detectable for all studied systems by using a suitable setup (section IV.5). Long-term measurements on the evolution of the detected potential difference revealed that all potential curves start at positive values between 120-550 mV and subsequently decrease down to values near to zero within periods ranging from around 8 to more than 45 h, depending on the metal salt used. When Pt electrodes were applied, potential curves exhibit distinctly stepwise progressions, while a more constant decrease of the potential differences was observed for a setup comprising Ag/AgCl electrodes.

A generalized electrochemical model for the silicate garden systems was established that could explain the characteristic evolution of the potential differences by an interplay of diffusion and membrane potentials, in combination with a pH induced potential, originating from existing pH gradients between both compartments during the first period of silicate garden growth.

2.3. General Conclusions

From all obtained data it was concluded that the precipitated tube walls should be regarded as an intermediate between a diaphragm and a membrane, which is permanently or temporarily impermeable for cobalt/iron, hydroxide and silicate ions, while water, sodium and chloride ions can readily diffuse through the tube walls. Temporal or permanent impermeability towards these three ion species, however, does not originate from classical size exclusion mechanisms but is rather directed by chemical conditions prevailing in the interior and exterior solutions of the silicate garden system. As soon as convenient environments in the tube interior are achieved by diffusion and/or precipitation processes, tube walls become permeable for exterior hydroxide and silicate ions, so that all silicate gardens finally end up in thermodynamic equilibrium with identical ion concentrations of all participating species in both compartments. At that point, remaining potential differences are essentially terminated.

Results from potential measurements allow a quantitative interpretation of the potential progressions, and it was demonstrated that potential measurements in silicate garden systems are a reliable tool for the detection of significant gradients in pH and ion concentrations over extended time frames.

It was further found that the evolution of the potential curves strikingly mirror the occurring precipitation and diffusion processes leading to the elimination of the prevailing ion concentration gradients. Therefore, progressions of the cell potentials combine results from AES and pH measurements. Hence, potential measurements offer the opportunity to easily estimate the duration of precipitation and diffusion processes before the systems ends up in thermodynamic equilibrium.

3. Crystallization Processes during Silicate Garden Growth

In-situ XRD measurements performed on silicate garden systems prepared from a series of different cobalt and iron metal salts revealed the existence of crystalline fractions in the precipitating tubular membranes (section IV.6.1). Crystalline material could be identified as metal hydroxides ($Fe(OH)_2$, $Co(OH)_2$), metal hydroxide chlorides ($Fe_2(OH)_3Cl$, $Co_2(OH)_3Cl$), metal hydroxide nitrate ($[Co_4(OH)_8 \cdot CoO_{0.48}(OH)_{0.52}NO_3]$) or metal hydroxide oxide (FeOOH).

The resulting crystalline material strongly depends on the counter ion of the metal salt. Especially when chloride salts were used, an incorporation of the counter ion into the forming crystalline material is observed, while in contrast sulphate and nitrate ions are not or only slightly participating in crystallization processes.

The tendency to crystallization processes was found to be mainly determined by the type of metal ion. For the examined systems, a higher tendency towards crystallization was observed for silicate gardens prepared from Fe(II) and Co(II) salts, while use of

Fe(III) salts brings about small if any fractions of crystalline material embedded in the precipitated membranes.

In contrast to the more or less similar performance of ion concentration, pH and potential evolutions found in the different silicate garden systems, no uniform behavior was found for the occurrence of crystallization processes, therefore not allowing for the drawing of a generalized statement.

However, in those cases, where crystalline fractions were detectable, crystallization commences right after silicate garden formation and proceeds within extended periods of several hours, resulting in increasing total amounts of crystalline material (sections IV.6.2 and IV.6.3).

4. Kinetics of Silicate Garden Formation

Progressions of the metal ion concentrations found in the interior compartment as well as the temporal evolution of crystallization occurring in the precipitated membrane material were used for the establishment of a kinetic model, describing relevant processes of silicate garden growth (section IV.7).

In summa, silicate garden growth can be regarded as a type of irreversible consecutive reaction, with the dissolution of the solid metal salt in a first step, followed by precipitation and crystallization reactions in the membrane material which may either occur in parallel or subsequently.

Experimental data obtained from AES concentration measurements as well as results from the XRD measurements on the progress of crystallization processes were found to fit well to the established kinetic model, independent of the examined system.

5. Constitution of the Resulting Tubular Precipitates

Similar to the crystallization behavior, no generalized statement can be drawn from the results of SEM and EDX measurements on different silicate garden systems (section IV.2). Except for their coincident macroscopic dimensions and wall thicknesses, examined precipitates taken from open-tube grown and isolated silicate gardens reveal significant differences not only in their structural behavior but also in their chemical composition.

Formation of distinct layers in the course of the precipitation of the tube walls was only observed for $FeCl_3$ and $CoCl_2$ based silicate gardens by EDX and SEM analysis, revealing the existence of a smooth, compact and less porous silica-enriched outer skin and a distinctly structured interior tube surface, rich in cobalt/iron and oxygen.

In contrast to that, no significant differences were found for the elemental composition of the interior and exterior surface of tubules precipitated with $FeCl_2$. No noteworthy amounts of silica were detectable on the outer surface by EDX, therefore challenging the proposed formation of an initial silica gel layer at the beginning of silicate garden growth. However, visual observations clearly confirm the presence of a silica gel film, as at first, a colourless jelly membrane forms which subsequently turns more and more green due to precipitation of "green rust". Consequently, the primary silica skin becomes either re-dissolved during the evolution of growth due to the high pH of the surrounding water glass or is only loosely attached to the second layer composed of "green rust" and is peeled off during the isolation process.

Another difference between the various silicate garden systems is the presence of isolated crystallites on the interior surface. While $FeCl_3$-silicate tubes lack in the existence of isolated crystals, numerous crystallites with angular shapes were found in precipitates prepared from $FeCl_2$ and $CoCl_2$.

Besides the mentioned discrepancies, EDX and SEM analyses also uncovered some similarities in the examined systems.

For example, low to zero Si contents were found in the tube interior, indicating that no silica skin is deposited on the interior surface after penetration of silicate ions through the membrane commenced at later growth times.

Further, elemental composition of the tube interior, determined by quantitative EDX analysis, correlates well to the chemical formula of crystalline material obtained by in-situ XRD analysis methods. This hence confirms the supposition that crystallites are mainly deposited on the interior surface of the membrane tubes.

6. Development of a Schematic Growth Model

In due consideration of all gathered data, silica garden growth can overall roughly be subdivided into six general stages, which are schematically explained in the following for a system based on $CoCl_2$ (Fig. 83):

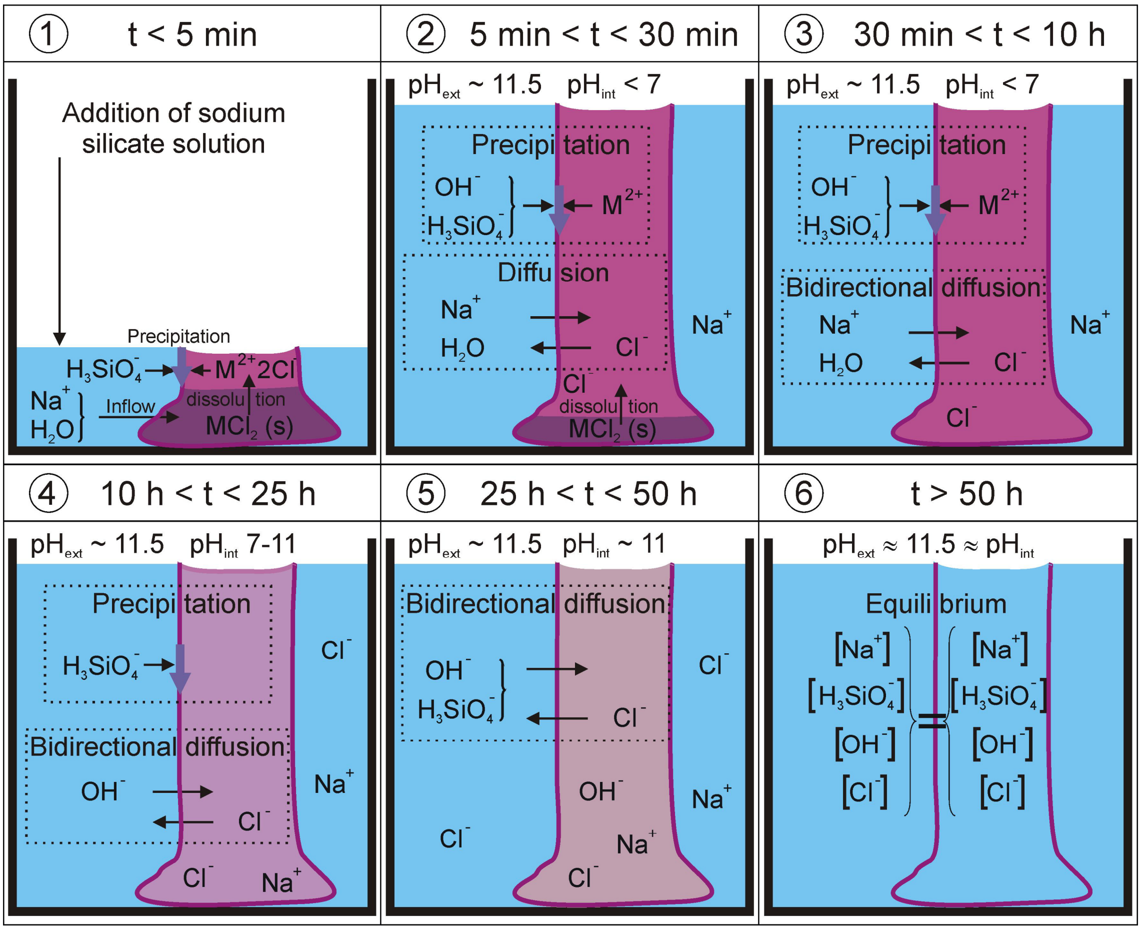

Fig. 83: Basic stages of silica garden formation, exemplarily depicted for a system based on Co(II) chloride exhibiting open-tube growth. For the sake of simplicity, “$H_3SiO_4^-$“ represents all soluble silicate species existing in the system.

1. Initiation Step

Starting from a solid metal salt tablet, slow addition of sodium silicate solution provokes superficial soaking of the tablet with liquid and concurrently an initial inflow of water together with sodium and hydroxide ions. Instantly, a membrane is formed surrounding the wetted salt pellet, which absorbs further water and incurs dissolution.

2. Incipient Garden Growth

Upon continued dosing of dilute water glass, an open tube emerges due to precipitation of cobalt silicate and hydroxide, while dissolution of the solid cobalt salt is promoted mainly by osmosis-driven diffusion of water through the membrane.

3. **Continued Garden Growth**

   These more or less simultaneously occurring processes have led to the formation of an intact macroscopic membrane tube. Once compartmentalization and dissolution of the metal salt tablet are completed, no more fresh metal ions (M^{2+}) are supplied in the interior solution and metal hydroxide precipitation on the inner surface of the wall decreases their concentration. Concurrently, silica precipitates on the external surface of the membrane due to the acidic pH in the inside. At the same time, diffusion of iodide ions from the inner solution into the surrounding water glass reservoir is initiated and accompanied by counter-diffusion of exterior sodium ions into the tube interior. These parallel processes begin to reduce the concentration and pH gradients across the membrane.

4. **Completed Precipitation**

   When all dissolved metal ions have been consumed by precipitation, the interior pH is approximately neutral and thus still low enough to prevent transport of soluble silicate species through the membrane. As a consequence of the remaining pH gradient, silica keeps on precipitating on the outer membrane surface. In turn, diffusion of hydroxide ions through the membrane into the tube interior is now possible and subsequently increases its pH to more and more alkaline values.

5. **Delayed Silicate Diffusion**

   Within a period of several hours, hydroxide ion diffusion has largely eliminated the difference in pH between the two reservoirs and established a pH of about 11 in the interior solution. Therefore, the solubility of silica inside the tube is markedly enhanced and precipitation on the outer surface gives way to unimpeded diffusion of silicate ions through the wall.

6. **Equilibrium State**

   After all diffusion processes have expired, the pH and the concentrations of all present species are equal on both sides of the membrane and thermodynamic equilibrium is achieved.

It is worthwhile mentioning that the modified procedure applied for silica garden preparation brings about some differences regarding the growth mechanism as compared to conventional experiments. For instance, replacing the commonly formed closed membrane over the salt pellet by a fairly wide tube open to the atmosphere eliminates osmotically induced excess pressures in the interior solution, which usually trigger membrane expansion and rupture. In the setup used in this work, the increasing volume of the inner solution can readily escape upwards without compulsion, thus gradually enlarging the tube and precipitating new membrane material. This enables controlled growth of a single tube whose dimensions are essentially determined by the size and shape of the employed pellet, in contrast to classical silica gardens where high osmotic pressures result in the extrusion of multiple irregular filaments from a salt crystal. Further, whereas vertical growth of microscopic tubular structures is conventionally directed by buoyancy of the lighter metal salt solution in the surrounding silica sol, it rather occurs as a consequence of slow and continuous addition of water glass in the present case.

VI. Further Considerations and Outlook

1. On the Usability of the Generated Cell Potentials

At a first glance, the spontaneous generation of two compartments with distinct ion concentrations by precipitation of a membrane and the resulting existence of a cell potential reveal several similarities to the functionality of biological cells, where differences in proton, sodium and potassium concentrations between the interior cytosol and the extracellular solution lead to the generation of a noticeable membrane potential. This potential difference is used in biology for the transformation of electrical into chemical energy by controlled transportation of the mentioned ion species through specific ion channels and ion pumps (different types of transmembrane proteins). In case of ATP-synthase, reduction of the cell potential by diffusion processes is used for the synthesis of ATP from ADP and phosphate (cf. Fig. 84).[107-108]

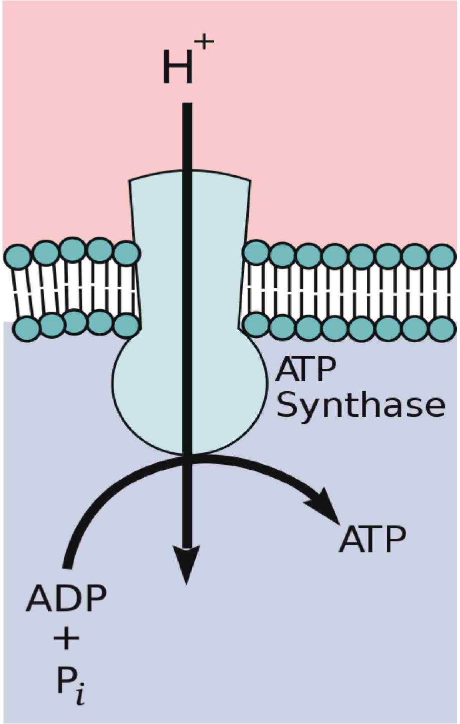

Fig. 84: Generation of ATP from ADP and phosphate by diffusion of protons from the more acidic extracellular region through the channels of the ATP synthase into the more basic cytosol along existing pH gradients across the cell membrane.[107]

Due to the general similarities found between chemical gardens and living systems, the question arises whether the generated potential difference in chemical gardens could be used in a similar way for the promotion of suitable chemical syntheses.

To contribute to the clarification of this interrogation, one must – in a first step – consider the origin of the measured cell potentials in silicate gardens. As pointed out in sections IV.5 and V.2, the overall cell potential represents a superposition of membrane, diffusion and possible redox potentials. Although all three different potentials are generated by pH and ion concentration gradients across the membrane, their possible usability as a driving force for any hypothetical chemical synthesis differs substantially:

While, as in biological cells, the diffusion and membrane potentials could be used to obtain energy from concentration equilibration by ongoing diffusion processes (where no chemical reaction takes place), the use of the possibly observed redox potential, in turn, requires the discharge of the system by occurring redox processes.

Regarding the data collected from analyses of conventional chemical garden growth presented in this work, the following considerations can be drawn on this issue:

1. Self-Discharge of the System within a Limited Period

Conventional chemical gardens were found to evolve from a highly energetic state at the beginning into thermodynamic equilibrium at the end of growth due to a combination of ion diffusion, membrane precipitation and crystallization. All these different processes contribute to the complete self-discharge of the overall system within a maximum period of ~ 50 hours. As potentials, though remarkably high at the beginning of chemical garden growth, are eliminated to a high extent during the first 5-15 hours, the period with potentials, high enough to promote any other hypothetical reaction, is strongly limited.

Furthermore, in all performed studies, no indications were found that the energy – released during the return of the system towards thermodynamic equilibrium – was used as a driving force for the occurrence of any additional reaction.

2. Non-Specific Ion Transport across the Precipitated Membrane

In contrast to biological cells, where highly complex molecular structures allow the controlled diffusion of specific ion species through tailored ion channels and pumps, therefore enabling the usability of existing concentration gradients for the promotion of energetically impeded chemical reactions (ATP synthesis), non-specific ion diffusion is observed across the precipitated membranes in chemical gardens. As a consequence to this, observed diffusion and membrane potentials could not be used for the initiation of any hypothetical chemical synthesis *in* the membrane wall.

3. Local Separation of the Silica Garden from an External Chemical System

One might, on the other hand, argue that existing chemical gradients could possibly be used to promote any energetically hindered redox reaction, whose corresponding redox pairs are spatially separated from the chemical garden system. A schematical drawing of such a theoretical setup is depicted in Fig. 85.

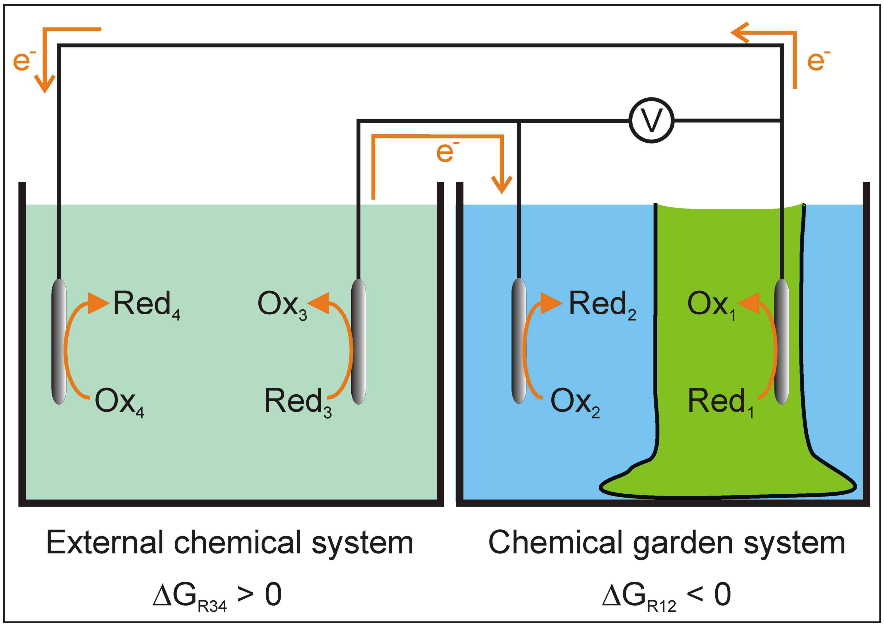

Fig. 85: Schematical drawing of a theoretical setup for the use of cell potentials in chemical gardens for the promotion of an external redox reaction, involving the application of four electrodes.

Several necessary preconditions must be fulfilled for the realization of this hypothetical process; first of all, the overall Gibbs free energy of the system must be negative. Consequently, propulsion of an energetically hindered redox reaction ($\Delta G_{34} > 0$) in the external system by the released energy of the spontaneous reaction in the chemical garden system ($\Delta G_{12} < 0$) requires that $|\Delta G_{12}| > |\Delta G_{34}|$. Second, the setup requires the existence of corresponding redox pairs in both compartments (Ox_1/Red_1 and Ox_2/Red_2), which can be realized in two different ways:

The first possibility involves the use of redox active electrodes which can participate in the redox process (e.g. Ag/AgCl electrodes), while in the second imaginable setup inert electrodes are applied in the chemical garden system. However, in the latter case a second redox active species (Ox_2) must be added to the exterior solution, as all ion species in conventional chemical gardens should have the same oxidation state in both compartments. Such a system is represented by a chemical garden prepared from iron(II) chloride, where two identical Pt electrodes are immersed into both compartments, containing dissolved Fe^{2+} in the interior solution and small amounts of riboflavin in its oxidized state (cf. Fig. 86) in the exterior sodium silicate solution.

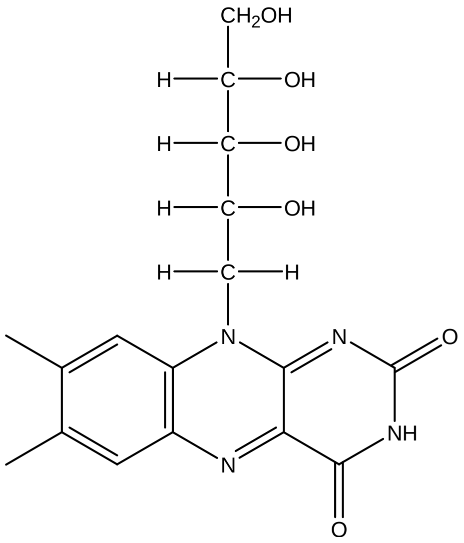

Fig. 86: Chemical structure of riboflavin in its oxidized state.

However, two different detrimental effects were found in this chemical garden system that prevent the usability of a redox active species which is added to the exterior compartment. First of all, it was observed that even large molecules like riboflavin can readily diffuse through the precipitated membrane walls (data not shown in this work). Therefore, a long-term separation of the redox active species in both compartments becomes impossible and reduction of riboflavin takes place in the interior solution by oxidation of Fe^{2+} to Fe^{3+}. Furthermore, results from *ex-situ* analyses (presented in section IV.2) revealed a more or less omnipresent incorporation of metal ions (especially iron(II)) into most segments of the membrane wall. As a consequence to this ubiquitous presence of redox active metal ions, the riboflavin can also directly react with the iron(II) precipitated in the tube walls (data not presented in this work).

Both negative effects generally eliminate the opportunity to perform locally separated redox reactions in both half cells of chemical gardens by the use of a second and dissolved redox active species in the exterior solution.

However, even if assuming the choice of an appropriate experimental system, a number of further obstacles must be considered that can also contribute to a failure of such experiments:

As already indicated above, the period in which a suitable potential, high enough to be used for the activation of a hindered chemical reaction, is strongly limited due to the rapid self-discharge of the system. In addition to this limitation, a possibly slow charge of the electrolytic double layer on all participating electrodes could further reduce the efficiency of the chemical garden systems as a driving force for external chemical syntheses. In case that the rate of the redox reactions on the surface of the electrodes is too high, the area around the electrodes may become impoverished in active redox species. As a consequence, the reaction becomes diffusion controlled, and the reaction rate significantly decreases when no homogenization of the solutions is realized by stirring (which is hardly realizable in conventional chemical garden systems). Another detrimental effect could be found in the existence of charge transfer resistances at all involved electrodes which might either partially or completely impede the electron transfer at the surfaces of the electrodes.

From all considerations and observations that can be drawn from the present results, it can be stated that the only possible way to use the generated potential in chemical gardens might be found in the application of redox-active electrodes, therefore using existing concentration gradients without the need of introducing additional redox active compounds in the exterior (or interior) compartment.

However, for all scenarios, the problem of self-discharge of the system by diffusion and precipitation processes remains, therefore generally challenging the usability of the generated cell potential for any chemical application.

2. Macroscopic Growth of Cement Gardens?

As described in section II.5.1 of this work, the mechanism of Portland cement hydration involves several processes very similar to those occurring during the formation of silicate gardens, though in a more or less reversed situation: A calcium silicate hydrate membrane is generated from grains of solid tricalcium silicate after addition of water, separating a highly concentrated interior metal silicate solution from a surrounding aqueous solution containing metal ions. In the course of cement hydration, swelling and bursting of this membrane results in the formation of calcium silicate hydrate filaments as observed for silicate gardens.

Due to the importance of the field of cement chemistry for the progressiveness of all industrial nations, these processes were already analyzed in detail by numerous groups. However, also most of these studies were performed on a microscopic scale, therefore not allowing the analysis of the interior solutions entrapped in the precipitated calcium silicate hydrate membrane.

In the present work it was demonstrated that macroscopic growth of tubules with an open membrane can be realized by using pressed pellets of ground metal salts. Therefore the mentioned limitations in the analysis of cement hydration might be eliminated by also applying the presented preparation technique on the field of cement hydration. This technique might pave the way to a detailed analysis of the temporal evolution of dissolution and precipitation processes that occur in the inside of the C-S-H membrane.

VII. Appendix

Table of Figures

Index of Tables

List of Publications

(1) **Glaab, F.**; Kellermeier, M.; Kunz, W. “Chiral Polymer Helices with Shape Identical to Previously Reported Helical Calcium Carbonate Morphologies“. *Macromolecular Rapid Communications* 2007, *28*, 1024-1028.

(2) **Glaab, F.**; Kellermeier, M.; Melero-García, E.; García-Ruiz, J. M.; Kunz, W. “EXAFS Studies on Zr-containing Sol-Gel Solutions Prepared with Monomeric and Polymeric Zirconia Compounds”. *DESY Annual Report* 2008.

(3) **Glaab, F.**; Kellermeier, M.; Kunz, W.; García-Ruiz, J. M. “On the Formation and Evolution of Chemical Gradients and Potential Differences Across Self-Assembling Inorganic Membranes”. Accepted in *Angewandte Chemie International Edition.*

(4) **Glaab, F.**; Kellermeier, M.; Klein, R.; Melero-García, E.; Choquesillo-Lazarte, D.; Kunz, W.; García-Ruiz, J. M. “On the Kinetics of Crystallization and Precipitation Processes during the Evolution of Chemical Gardens”. To be submitted to *Journal of Crystal Growth* (in preparation).

(5) Kellermeier, M.; **Glaab, F.**; Melero-García, E.; Klein, R.; García-Ruiz, J. M.; Kunz, W. “Co-Precipitation of Calcium Carbonate and Silica”. *DESY Annual Report* 2008.

(6) Kellermeier, M.; **Glaab, F**.; Carnerup, A. M.; Drechsler, M.; Gossler, B.; Hyde, S. T.; Kunz, W. “Additive-Induced Morphological Tuning of Self-Assembled Silica-Barium Carbonate Crystal Aggregates”. *Journal of Crystal Growth* 2009, *311*, 2530-2541.

(7) Kellermeier, M.; **Glaab, F.**; Melero-García, E.; García-Ruiz, J. M.; Kunz, W. “Crystallization of Calcium Carbonate in Alkaline, Silica-rich Brines at Elevated Temperatures”. *DESY Annual Report* 2009.

(8) Kellermeier, M.; **Glaab, F**.; Melero-García, E.; Klein, R.; Kunz, W.; García-Ruiz, J. M. “The Effect of Silica on Calcium Carbonate Polymorphic

Precipitation: An In-Situ Synchrotron X-Ray Diffraction Study”. To be submitted to *Angewandte Chemie International Edition*.

(9) Kellermeier, M.; Melero-García, E.; **Glaab, F.**; Klein, R.; Kunz, W.; García-Ruiz, J. M. “EXAFS Study of Counter-ion Coordination and Complexation of Barium Ions in Solution”. *DESY Annual Report* 2007.

(10) Kellermeier, M.; Melero-García, E.; **Glaab, F.**; Klein, R.; Drechsler, M.; Rachel, R.; García-Ruiz, J. M. “Stabilization of Amorphous Calcium Carbonate in Inorganic Silica-Rich Environments”. *Journal of the American Chemical Society* 2010, *131*, 17859-17866.

(11) Kellermeier, M.; Melero-García, E.; **Glaab, F**.; Eiblmeier, J.; Kienle, L.; Kunz, W.; García-Ruiz, J. M. “Growth Behavior and Kinetics of Self-Assembled Silica-Carbonate Biomorphs”. Accepted in *Chemistry – A European Journal*.

Literature

[1] S. Leduc, *The Mechanism of Life*, Rebman, London, **1911**.

[2] J. R. Glauber, *A Description of New Philosphical Furnaces*, Coats, London, **1651**.

[3] M. Copisarow; *Colloid and Polymer Science*, **1929**, 47, 60-65.

[4] T. H. Hazelhurst; *Journal of Chemical Education*, **1941**, 18, 286-289.

[5] C. W. J. Ross; *Journal of the Royal Society of New South Wales*, **1910**, 44, 583-592.

[6] R. D. Coatman, N. L. Thomas, D. D. Double; *Journal of Materials Science*, **1980**, 15, 2017-2026.

[7] J. H. E. Cartwright, J. M. García-Ruiz, M. L. Novella, F. Otálora; *Journal of Colloid and Interface Science*, **2002**, 256, 351-359.

[8] S. Thouvenel-Romans, O. Steinbock; *Journal of the American Chemical Society*, **2003**, 125, 4338-4341.

[9] S. Thouvenel-Romans, W. v. Saarloos, O. Steinbock; *Europhysics Letters*, **2004**, 67, 42-48.

[10] S. Thouvenel-Romans, J. J. Pagano, O. Steinbock; *Physical Chemistry Chemical Physics*, **2005**, 7, 2610-2615.

[11] J. J. Pagano, T. Bánsági, O. Steinbock; *The Journal of Physical Chemistry C*, **2007**, 111, 9324-9329.

[12] I. Uechi, A. Katsuki, L. Dunin-Barkovskiy, Y. Tanimoto; *The Journal of Physical Chemistry B*, **2004**, 108, 2527-2530.

[13] W. Duan, S. Kitamura, I. Uechi, A. Katsuki, Y. Tanimoto; *The Journal of Physical Chemistry B*, **2005**, 109, 13445-13450.

[14] H. Yokoi, N. Kuroda, Y. Kakudate; *Journal of Applied Physics*, **2005**, 97, 10R513-3.

[15] D. E. H. Jones, U. Walter; *Journal of Colloid and Interface Science*, **1998**, 203, 286-293.

[16] D. Balköse, F. Özkan, U. Köktürk, S. Ulutan, S. Ülkü, G. Nişli; *Journal of Sol-Gel Science and Technology*, **2002**, 23, 253-263.

[17] J. J. Pagano, S. Thouvenel-Romans, O. Steinbock; *Physical Chemistry Chemical Physics*, **2007**, 9, 110-116.

[18] K. Parmar, H. T. Chaturvedi, M. W. Akhtar, S. Chakravarty, S. K. Das, A. Pramanik, M. Ghosh, A. K. Panda, N. Bandyopadhya, S. Bhattacharjee; *Materials Characterization*, **2009**, 60, 863-868.

[19] C. Collins, W. Zhou, A. L. Mackay, J. Klinowski; *Chemical Physics Letters*, **1998**, 286, 88-92.

[20] C. Collins, G. Mann, E. Hoppe, T. Duggal, T. L. Barr, J. Klinowski; *Physical Chemistry Chemical Physics*, **1999**, 1, 3685-3687.

[21] C. Collins, R. Mokaya, J. Klinowski; *Physical Chemistry Chemical Physics*, **1999**, 1, 4669-4672.

[22] Jason J. Pagano, T. Bánsági, O. Steinbock; *Angewandte Chemie International Edition*, **2008**, 47, 9900-9903.

[23] E. Bormashenko, Y. Bormashenko, O. Stanevsky, R. Pogreb, G. Whyman, T. Stein, Z. Barkay; *Colloids and Surfaces A: Physicochemical and Engineering Aspects*, **2006**, 289, 245-249.

[24] C. Collins, W. Zhou, J. Klinowski; *Chemical Physics Letters*, **1999**, 306, 145-148.

[25] T. S. Sørensen; *Journal of Colloid and Interface Science*, **1981**, 79, 192-208.

[26] J. H. E. Cartwright, B. Escribano, S. Khokhlov, C. I. Sainz-Diaz; *Physical Chemistry Chemical Physics*, **2011**, 13, 1030-1036.

[27] J. H. E. Cartwright, B. Escribano, C. I. Sainz-Díaz; *Langmuir*, **2011**, 27, 3286-3293.

[28] J. Pantaleone, A. Toth, D. Horvath, L. RoseFigura, W. Morgan, J. Maselko; *Physical Review E (Statistical, Nonlinear, and Soft Matter Physics)*, **2009**, 79, 056221-8.

[29] J. J. Pagano, *Growth Dynamics and Composition of Tubular Structures in a Reaction-Precipitation System*, Florida State University, Tallahassee, Florida, United States, **2008**.

[30] P. M. Dove, J. D. Rimstidt; *Reviews in Mineralogy and Geochemistry* **1994**, 29, 259-308.

[31] J. Pantaleone, A. Toth, D. Horvath, J. Rother McMahan, R. Smith, D. Butki, J. Braden, E. Mathews, H. Geri, J. Maselko; *Physical Review E*, **2008**, 77, 046207.

[32] R. K. Iler, *The Chemistry of Silica : Solubility, Polymerization, Colloid and Surface Properties, and Biochemistry*, Wiley, New York, **1979**.

[33] S. P. Mukherjee; *Journal of Non-Crystalline Solids*, **1980**, 42, 477-488.

[34] R. K. Iler; *Soil Science*, **1955**, 80, 86.

[35] J. M. Fletcher, C. J. Hardy; *Chemical Industry*, **1968**, 2, 48-51.

[36] E. Smy; *Journal of Sol-Gel Science and Technology*, **1998**, 13, 233-236.

[37] P. B. Sarawade, J. K. Kim, J. K. Park, H. K. Kim; *Aerosol and Air Quality Research*, **2006**, 6, 93-105.

[38] M. A. Tenan, D. M. Soares, C. A. Bertran; *Langmuir*, **2000**, 16, 9970-9976.

[39] F. Gaboriaud, A. Nonat, D. Chaumont, A. Craievich; *Journal of Non-Crystalline Solids*, **2005**, 351, 351-354.

[40] K. Sinkó, A. Neményi; *Progress in Colloid and Polymer Science*, **2004**, 125, 103-110.

[41] S. P. Mukherjee, J. Zarzycki, J. P. Traverse; *Journal of Materials Science*, **1976**, 11, 341-355.

[42] W. L. Konijnenijk, M. v. Duuren, H. Croenendijk; *Verres Réfract*, **1973**, 27, 11.

[43] K. Kazmierski, J. Chojnowski, J. McVie; *European Polymer Journal*, **1994**, 30, 515-527.

[44] C. J. Brinker, *Sol-Gel Science : The Physics and Chemistry of Sol-Gel Processing*, Academic Press, Boston, **1990**.

[45] A. M. Buckley, M. Greenblatt; *Journal of Chemical Education*, **1994**, 71, 599-602.

[46] W. G. Klemperer, S. D. Ramamurthi; *Journal of Non-Crystalline Solids*, **1990**, 121, 16-20.

[47] D. L. Wood, E. M. Rabinovich; *Journal of Non-Crystalline Solids*, **1989**, 107, 199-211.

[48] S. E. Johnson, J. A. Deiters, R. O. Day, R. R. Holmes; *Journal of the American Chemical Society*, **1989**, 111, 3250-3258.

[49] B. Himmel, T. Gerber, H. Bürger; *Journal of Non-Crystalline Solids*, **1990**, 119, 1-13.

[50] D. W. Schaefer; *Science* **1989**, 243, 1023-1027.

[51] D. W. Schaefer, K. D. Keefer; *Physical Review Letters*, **1986**, 56, 2199-2202.

[52] W. M. Jones, D. B. Fischbach; *Journal of Non-Crystalline Solids*, **1988**, 101, 123-126.

[53] S. Chiou, H. T. Hahn; *Journal of the American Ceramic Society*, **1994**, 77, 155-160.

[54] M. Ramirez del Solar, L. Esquivias; *Journal of Sol-Gel Science and Technology*, **1994**, 3, 41-46.

[55] K. Parmar, A. K. Pramanik, N. R. Bandyopadhya, S. Bhattacharjee; *Materials Research Bulletin*, **2010**, 45, 1283-1287.

[56] R. E. Liesegang; *Kolloid-Zeitschrift*, **1911**, 9, 298-300.

[57] E. Bormashenko, Y. Bormashenko, O. Stanevsky, R. Pogreb; *Chemical Physics Letters*, **2006**, 417, 341-344.

[58] H. Yokoi, et al.; *Journal of Physics: Conference Series*, **2006**, 51, 454-457.

[59] C. Ritchie, G. J. T. Cooper, Y.-F. Song, C. Streb, H. Yin, A. D. C. Parenty, D. A. MacLaren, L. Cronin; *Nature Chemistry*, **2009**, 1, 47-52.

[60] D. E. H. Jones; *American Scientist*, **2002**, 90, 454-461.

[61] J. H. E. Cartwright, B. Escribano, C. I. Sainz-Díaz, L. S. Stodieck; *Langmuir*, **2011**, 27, 3294-3300.

[62] J. Maselko, P. Strizhak; *The Journal of Physical Chemistry B*, **2004**, 108, 4937-4939.

[63] O. L. Riggs, J. D. Sudbury, M. Hutchison; *Corrosion*, **1960**, 16, 260-264.

[64] J. D. Sudbury, O. L. Riggs, F. J. Radd; *Corrosion*, **1962**, 18, 8-25.

[65] D. D. Double, A. Hellawell; *Nature*, **1976**, 261, 486-488.

[66] D. D. Double, A. Hellawell; *Scientific American*, **1977**, 237, 82-92.

[67] D. D. Double, A. Hellawell, S. J. Perry; *Proceedings of the Royal Society of London, A*, **1978**, 359, 435-51.

[68] J. D. Birchall, A. J. Howard, J. E. Bailey; *Proceedings of the Royal Society of London, A*, **1978**, 360, 445-453.

[69] D. D. Double, P. C. Hewlett, K. S. W. Sing, J. F. Raffle; *Philosophical Transactions of the Royal Society of London. Series A, Mathematical and Physical Sciences*, **1983**, 310, 53-66.

[70] D. A. Stone, R. E. Goldstein; *Proceedings of the National Academy of Sciences of the United States of America*, **2004**, 101, 11537-11541.

[71] M. J. Russell, R. M. Daniel, A. J. Hall, J. A. Sherringham; *Journal of Molecular Evolution*, **1994**, 39, 231-43.

[72] R. C. L. Larter, A. J. Boyce, M. J. Russell; *Mineralium Deposita*, **1981**, 16, 309-317.

[73] A. J. Boyce, M. L. Coleman, M. J. Russell; *Nature*, **1983**, 306, 545-550.

[74] A. Ackermann; *Kolloid-Zeitschrift*, **1921**, 28, 270-80.

[75] A. Ackermann; *Kolloid-Zeitschrift*, **1932**, 59, 49-55.

[76] M. G. Fontana, *Corrosion Engineering*, McGraw-Hill, New York, **1986**.

[77] G. Butler, H. C. K. Ison; *Nature*, **1958**, 182, 1229-1230.

[78] J. B. Corliss, J. Dymond, L. I. Gordon, J. M. Edmond, R. P. von Herzen, R. D. Ballard, K. Green, D. Williams, A. Bainbridge, K. Crane, T. H. van Andel; *Science*, **1979**, 203, 1073-1083.

[79] K. L. Von Damm, M. D. Lilley, W. C. Shanks Iii, M. Brockington, A. M. Bray, K. M. O'Grady, E. Olson, A. Graham, G. Proskurowski; *Earth and Planetary Science Letters*, **2003**, 206, 365-378.

[80] D. K. Blackman, J. A. Karson, D. S. Kelley, J. R. Cann, G. L. Früh-Green, J. S. Gee, S. D. Hurst, B. E. John, J. Morgan, S. L. Nooner, D. K. Ross, T. J. Schroeder, E. A. Williams; *Marine Geophysical Researches*, **2002**, 23, 443-469.

[81] D. S. Kelley; *Oceanography*, **2005**, 18, 32-45.

[82] D. S. Kelley, J. A. Karson, D. K. Blackman, G. L. Fruh-Green, D. A. Butterfield, M. D. Lilley, E. J. Olson, M. O. Schrenk, K. K. Roe, G. T. Lebon, P. Rivizzigno; *Nature*, **2001**, 412, 145-149.

[83] D. S. Kelley, J. A. Karson, G. L. Früh-Green, D. R. Yoerger, T. M. Shank, D. A. Butterfield, J. M. Hayes, M. O. Schrenk, E. J. Olson, G. Proskurowski, M. Jakuba, A. Bradley, B. Larson, K. Ludwig, D. Glickson, K. Buckman, A. S. Bradley, W. J. Brazelton, K. Roe, M. J. Elend, A. Delacour, S. M. Bernasconi, M. D. Lilley, J. A. Baross, R. E. Summons, S. P. Sylva; *Science*, **2005**, 307, 1428-1434.

[84] G. Proskurowski, M. D. Lilley, D. S. Kelley, E. J. Olson; *Chemical Geology*, **2006**, 229, 331-343.

[85] G. Proskurowski, M. D. Lilley, J. S. Seewald, G. L. Früh-Green, E. J. Olson, J. E. Lupton, S. P. Sylva, D. S. Kelley; *Science*, **2008**, 319, 604-607.

[86] D. I. Foustoukos, W. E. Seyfried; *Science*, **2004**, 304, 1002-1005.

[87] N. H. Sleep, A. Meibom, T. Fridriksson, R. G. Coleman, D. K. Bird; *Proceedings of the National Academy of Sciences of the United States of America*, **2004**, 101, 12818-12823.

[88] J. L. Palandri, M. H. Reed; *Geochimica et Cosmochimica Acta*, **2004**, 68, 1115-1133.

[89] N. G. Holm, J. L. Charlou; *Earth and Planetary Science Letters*, **2001**, 191, 1-8.

[90] J. Corliss; *Origins of Life and Evolution of Biospheres*, **1989**, 19, 534-535.

[91] S. Miller, J. Bada, N. Friedmann; *Origins of Life and Evolution of Biospheres*, **1989**, 19, 536-537.

[92] http://www.elettra.trieste.it/experiments/beamlines/xrd1/index.html

[93] http://hasylab.desy.de/e70/e207/e674/e35190/e6238/F3-m_eng.gif

[94] Y. Tao, B. Zhu, Z. Chen; *Journal of Crystal Growth*, **2006**, 293, 382-386.

[95] http://farm4.static.flickr.com/3247/3353346629_be364aa4ae.jpg

[96] C. F. Baes, R. E. Mesmer, *The Hydrolysis of Cations*, John Wiley & Sons, New York, **1976**.

[97] *CRC Handbook of Chemistry and Physics*, Taylor & Francis, USA, **2006**.

[98] P. W. Atkins, *Physical Chemistry*, VCH Wiley, New York, **1996**.

[99] Y. Kishi, S. Shigemi, S. Doihara, M. G. Mostafa, K. Wase; *Hydrometallurgy.*, **1998**, 47, 325-338.

[100] C. H. Hamann, W. Vielstich, *Elektrochemie*, Wiley-VCH, **2005**.

[101] V. M. Schmidt, *Elektrochemische Verfahrenstechnik: Grundlagen, Reaktionstechnik, Prozessoptimierung*, Wiley-VCH, **2003**.

[102] S. A. Greenberg; *Journal of the American Chemical Society*, **1958**, 80, 6508-6511.

[103] B. Hille, *Ionic Channels of Excitable Membranes*, 2nd, Sinauer Associates, **1992**.

[104] C. A. Lewis; *The Journal of Physiology*, **1979**, 286, 417-445.

[105] Y. Marcus, *Ion Solvation*, Wiley, **1985**.

[106] K. A. Connors, *Chemical Kinetics: The Study of Reaction Rates in Solution*, VCH, **1990**.

[107] http://de.wikipedia.org/wiki/ATP-Synthase

[108] L. Stryer, *Biochemie*, 4th edition, Spektrum Akademischer Verlag, Berlin, **1999**.

Declaration

I hereby declare that I have independently composed the present thesis exclusively by the use of the cited references and resources. Literally or correspondingly adopted material is marked accordingly.

Hiermit erkläre ich, dass ich die vorliegende Doktorarbeit selbständig angefertigt habe. Es wurden nur die in der Arbeit ausdrücklich benannten Quellen und Hilfsmittel benutzt. Wörtlich oder sinngemäß übernommenes Gedankengut habe ich als solches kenntlich gemacht.

Ort, Datum

Unterschrift